1. REPORT DATE (DD-MM-YYYY)	2. REPORT TYPE	3. DATES COVERED (From - To)
26-07-2016	Final Report	1-May-2012 - 30-Apr-2016

4. TITLE AND SUBTITLE	5a. CONTRACT NUMBER
Final Report: Combustion of High Molecular Weight Hydrocarbon Fuels and JP-8 at Moderate Pressures (Research Area 1: Mechanical Sciences)	W911NF-12-1-0152
	5b. GRANT NUMBER
	5c. PROGRAM ELEMENT NUMBER
	611102

6. AUTHORS	5d. PROJECT NUMBER
Kalyanasundaram Seshadri	5e. TASK NUMBER
	5f. WORK UNIT NUMBER

7. PERFORMING ORGANIZATION NAMES AND ADDRESSES	8. PERFORMING ORGANIZATION REPORT NUMBER
University of California - San Diego Office of Contract & Grant Adm 9500 Gilman drive, MC 0934 La Jolla, CA 92093 -0934	

9. SPONSORING/MONITORING AGENCY NAME(S) AND ADDRESS (ES)	10. SPONSOR/MONITOR'S ACRONYM(S)
U.S. Army Research Office P.O. Box 12211 Research Triangle Park, NC 27709-2211	ARO
	11. SPONSOR/MONITOR'S REPORT NUMBER(S)
	61657-EG.16

12. DISTRIBUTION AVAILIBILITY STATEMENT
Approved for Public Release; Distribution Unlimited

13. SUPPLEMENTARY NOTES
The views, opinions and/or findings contained in this report are those of the author(s) and should not contrued as an official Department of the Army position, policy or decision, unless so designated by other documentation.

14. ABSTRACT

The objective of this research is to characterize combustion of high molecular weight hydrocarbon fuels and jet-fuels (in particular JP-8) and surrogates of jet-fuels in laminar non-uniform flows at elevated pressures upto 2.5 MPa. Experimental and kinetic modeling studies were carried out. Measurements include critical conditions of extinction and autoignition, and flame structure. The scientific questions that were addressed and answered are (1) How does pressure influence the critical conditions of extinction and autoignition? (2) What surrogate best reproduces selected combustion characteristics of JP-8 at atmospheric and moderate pressure? (3) What are

15. SUBJECT TERMS
Combustion, Jet Fuels, JP-8, Elevated Pressure, Autoignition, Kinetic Modeling

16. SECURITY CLASSIFICATION OF:			17. LIMITATION OF ABSTRACT	15. NUMBER OF PAGES	19a. NAME OF RESPONSIBLE PERSON
a. REPORT	b. ABSTRACT	c. THIS PAGE	UU		Kalyanasundaram Seshadri
UU	UU	UU			19b. TELEPHONE NUMBER
					858-534-4876

Report Title

Final Report: Combustion of High Molecular Weight Hydrocarbon Fuels and JP-8 at Moderate Pressures (Research Area 1: Mechanical Sciences)

ABSTRACT

The objective of this research is to characterize combustion of high molecular weight hydrocarbon fuels and jet-fuels (in particular JP-8) and surrogates of jet-fuels in laminar non-uniform flows at elevated pressures upto 2.5 MPa. Experimental and kinetic modeling studies were carried out. Measurements include critical conditions of extinction and autoignition, and flame structure. The scientific questions that were addressed and answered are (1) How does pressure influence the critical conditions of extinction and autoignition? (2) What surrogate best reproduces selected combustion characteristics of JP-8 at atmospheric and moderate pressure? (3) What are possible chemical kinetic mechanisms for these surrogates? (4) What is the influence of pressure on kinetic models. The concise answer to these questions are (1) With increasing pressure strain rates at extinction in general decrease. Autoignition temperature decrease with increasing pressure. A key observation that was not known prior to this work was that the influence of low-temperature chemistry increase with increasing pressure. (2) Surrogates of JP-8 were identified, (3) Chemical kinetic mechanisms were developed and tested. (4) Revisions were made to chemical kinetic mechanisms.

Enter List of papers submitted or published that acknowledge ARO support from the start of the project to the date of this printing. List the papers, including journal references, in the following categories:

(a) Papers published in peer-reviewed journals (N/A for none)

Received		Paper
08/30/2015	4.00	Ryan K. Gehmlich, Austin Kuo, Kalyanasundaram Seshadri. Experimental investigations of the influence of pressure on critical extinction conditions of laminar nonpremixed flames burning condensed hydrocarbon fuels, jet fuels, and surrogates, Proceedings of the Combustion Institute, (01 2015): 937. doi: 10.1016/j.proci.2014.05.111
08/30/2015	5.00	Kalyanasundaram Seshadri, Xue-Song Bai. Rate-Ratio Asymptotic Analysis of the Influence of Addition of Hydrogen on the Structure and Mechanisms of Extinction of Nonpremixed Methane Flames, Combustion Science and Technology, (12 2014): 3. doi: 10.1080/00102202.2014.971948
08/30/2015	6.00	Ulrich Niemann, Kalyanasundaram Seshadri, Forman A. Williams. Accuracies of laminar counterflow flame experiments, Combustion and Flame, (04 2015): 1540. doi: 10.1016/j.combustflame.2014.11.021
08/30/2015	7.00	S. Mani Sarathy, Ulrich Niemann, Coleman Yeung, Ryan Gehmlich, Charles K. Westbrook, Max Plomer, Zhaoyu Luo, Marco Mehl, William J. Pitz, Kalyanasundaram Seshadri, Murray J. Thomson, Tianfeng Lu. A counterflow diffusion flame study of branched octane isomers, Proceedings of the Combustion Institute, (01 2013): 1015. doi: 10.1016/j.proci.2012.05.106
08/30/2015	8.00	U.Niemann, K. Seshadri, F.A. Williams. Effect of pressure on structure and extinction of near-limit hydrogen counterflow diffusion flames, Proceedings of the Combustion Institute, (01 2013): 881. doi: 10.1016/j.proci.2012.06.145
08/30/2015	10.00	Ulrich Niemann, Kalyanasundaram Seshadri, Forman A. Williams. Methane, ethane, and ethylene laminar counterflow diffusion flames at elevated pressures: Experimental and computational investigations up to 2.0MPa, Combustion and Flame, (01 2014): 138. doi: 10.1016/j.combustflame.2013.07.019

TOTAL: **6**

Number of Papers published in peer-reviewed journals:

(b) Papers published in non-peer-reviewed journals (N/A for none)

<u>Received</u>   <u>Paper</u>

TOTAL:

Number of Papers published in non peer-reviewed journals:

(c) Presentations

Number of Presentations: 0.00

Non Peer-Reviewed Conference Proceeding publications (other than abstracts):

<u>Received</u>   <u>Paper</u>

07/26/2016 12.00 . Autoignition of Condensed Hydrocarbon Fuels in Nonpremixed Flows at Elevated Pressures,
2015 Spring Meeting of the Western States Section Combustion Institute. 21-MAR-16, University of
Washington, Seattle, Washington. : ,

08/27/2013 1.00 Vaishali Amin, Joshua Lee, Reinhard Seiser, and Kalyanasundaram Seshadri. The Structure, Extinction,
and Autoignition of Nonpremixed Toluene Flames,
2012 Spring Technical Meeting, Western States Section, The Combustion Institute. 19-MAR-12, . : ,

08/27/2013 2.00 Ryan Gehmlich, Kalyanasundaram Seshadri. Experimental Investigations of the Influence of Pressure on
CriticalConditions of Extinction of Laminar Nonpremixed Flames BurningCondensed Hydrocarbon Fuels,
8th US National Combustion Meeting, The Combustion Institute. 19-MAY-13, . : ,

08/30/2015 9.00 Gerald Mairinger, Ryan Gehmlich, Ernst Pucher, Kalyanasundaram Seshadri. Autoignition of n-Heptane
at Moderate Pressures,
9th US National Combustion Meeting. 18-MAY-15, . : ,

TOTAL: **4**

Number of Non Peer-Reviewed Conference Proceeding publications (other than abstracts):

<div style="text-align:center">

Peer-Reviewed Conference Proceeding publications (other than abstracts):

</div>

<u>Received</u>   <u>Paper</u>

TOTAL:

Number of Peer-Reviewed Conference Proceeding publications (other than abstracts):

<div style="text-align:center">

(d) Manuscripts

</div>

<u>Received</u>   <u>Paper</u>

07/21/2016 3.00 Ulrich Niemann, Kalyanasundaram Seshadri, Forman Williams. Methane, ethane, and ethylene laminar counterflow diffusion flames at elevated pressures: Experimental and computational investigations up to 2.0 MPa,
Combustion and Flame (05 2013)

TOTAL: **1**

Number of Manuscripts:

<div style="text-align:center">

Books

</div>

<u>Received</u>   <u>Book</u>

TOTAL:

<u>Received</u>　　　<u>Book Chapter</u>

TOTAL:

Patents Submitted

Patents Awarded

Awards

Graduate Students

NAME	PERCENT_SUPPORTED	Discipline
Gehmlich, Ryan	0.06	
Hogle, Robert	0.02	
Niemann, Ulrich	0.03	
Mairinger, Gerald	0.06	
FTE Equivalent:	**0.17**	
Total Number:	**4**	

Names of Post Doctorates

NAME	PERCENT_SUPPORTED
FTE Equivalent:	
Total Number:	

Names of Faculty Supported

NAME	PERCENT_SUPPORTED	National Academy Member
Kalyanasundaram Seshadri	0.13	
FTE Equivalent:	**0.13**	
Total Number:	**1**	

Names of Under Graduate students supported

NAME	PERCENT_SUPPORTED

FTE Equivalent:
Total Number:

Student Metrics
This section only applies to graduating undergraduates supported by this agreement in this reporting period

The number of undergraduates funded by this agreement who graduated during this period: 1.00

The number of undergraduates funded by this agreement who graduated during this period with a degree in science, mathematics, engineering, or technology fields:····· 1.00

The number of undergraduates funded by your agreement who graduated during this period and will continue to pursue a graduate or Ph.D. degree in science, mathematics, engineering, or technology fields:····· 1.00

Number of graduating undergraduates who achieved a 3.5 GPA to 4.0 (4.0 max scale):······ 1.00

Number of graduating undergraduates funded by a DoD funded Center of Excellence grant for Education, Research and Engineering:······ 0.00

The number of undergraduates funded by your agreement who graduated during this period and intend to work for the Department of Defense 1.00

The number of undergraduates funded by your agreement who graduated during this period and will receive scholarships or fellowships for further studies in science, mathematics, engineering or technology fields: 1.00

Names of Personnel receiving masters degrees

NAME

Total Number:

Names of personnel receiving PHDs

NAME
Ulrich Niemann
Ryan Gehmlich
Vaishali Amin

Total Number: 3

Names of other research staff

NAME	PERCENT_SUPPORTED

FTE Equivalent:
Total Number:

Sub Contractors (DD882)

Inventions (DD882)

Scientific Progress

See Attachment

Technology Transfer

Combustion of High Molecular Weight Hydrocarbon Fuels and JP-8 at Moderate Pressures

1   Statement of the Problem Studied

The objective of this research is to characterize combustion of high molecular weight hydrocarbon fuels and jet fuels (in particular JP-8) in laminar nonuniform flows at elevated pressures up to 2.5 MPa. Experimental and kinetic modelling studies were carried out. JP-8 is a mixture of numerous aliphatic and aromatic compounds. The major components of this fuel are straight chain paraffins, branched chain paraffins, cycloparaffins, aromatics, and alkenes. The concentration of paraffins is on the average 60 % by volume, that of cycloparaffins 20 %, that of aromatics 18 %, and that of alkenes 2 %. It has been established that an useful approach to elucidating aspects of combustion of jet fuels, is to first develop surrogates that reproduce selected aspects of combustion of JP-8. Surrogates are mixtures of hydrocarbon compounds. The hydrocarbon compounds used to construct the surrogate will depend on those aspects of combustion of JP-8 that the surrogate is expected to reproduce.

The experiments were conducted in the High Pressure Combustion Experimental Facility (HPCEF) that has been constructed at the University of California at San Diego (UCSD), using support from the U.S Army Research Office. The research was carried out in collaboration with Professor E. Ranzi and Professor A. Frassoldatiat Politecnico di Milano, Italy.

The following section is a summary of the most important results.

2   Summary of the Most Important Results

The research is described in the following six archival publications.

1. U. Niemann, K. Seshadri, and F. A. Williams, "Methane, Ethane, and Ethylene Laminar Counterflow Diffusion Flames at Elevated Pressures: Experimental and Computational Investigations up to 2.0 MPa ," *Combustion and Flame,*, **161**, 2014, pp 138—146.

2. R. Gehmlich, A. Kuo, K. Seshadri, "Experimental Investigations of the Influence of Pressure on Critical Extinction Conditions of Laminar Nonpremixed Flames Burning Condensed Hydrocarbon Fuels, Jet Fuels, and Surrogates," *Proceedings of the Combustion Institute,* **35**, 2015, pp 937-943.

3. K. Seshadri, and X. S. Bai, "Rate-Ratio Asymptotic Analysis of the Influence of Addition of Hydrogen on the Structure and Mechanisms of Extinction of Nonpremixed Methane Flames," *Combustion Science and Technology,* **187**, 2015, pp 3-26.

4. U. Niemann, K. Seshadri, and F. A. Williams, "Accuracies of Laminar Counterflow Flame Experiments," *Combustion and Flame,* **162**, 2015, pp 1540-1549.

5. G. Mairinger, R. Gehmlich, E. Pucher, K. Seshadri, "Autoignition of n-Heptane at Moderate Pressures," Paper # 114LF-0394, 9th US National Combustion Meeting, Central States Section of the Combustion Institute, May 17-20, 2015, Cincinnati, Ohio

6. G. Mairinger, A. Frassoldati, R. Gehmlich, U. Niemann, A. Stagni, E. Ranzi, K. Seshadri, "Autoignition of Condensed Hydrocarbon Fuels in Nonpremixed Flows at Elevated Pressures," *Combustion Theory and Modelling,* **in press**, 2016.

2.1 Methane, ethane, and ethylene laminar counterflow diffusion flames at elevated pressures: Experimental and computational investigations up to 2.0 MPa

The ability of chemicalkinetic mechanisms and transport descriptions to predict combustion processes is tested most easily and accurately by well-controlled laboratory experiments performed at normal atmospheric pressures, where measurements of strain rates at extinction, in particular, provide relevant tests of chemicalkinetic descriptions. In many practical applications, however, the combustion occurs at elevated pressures. Since the combustion chemistry varies with pressure, often non-monotonically in certain respects, it is desirable to pursue correspondingly well-controlled laboratory combustion experiments at pressures above atmospheric, as further tests of predictions. But such experiments, unfortunately, are difficult and expensive to design and perform. With ARO support recently a High Pressure Combustion Experimental Facility (HPCEF) was constructed in which experiments on laminar counterflow diffusion flames, premixed flames, and partially premixed flame can be carried out. Results of these experiments with hydrogen as the fuel have recently been published and reported in the previous final report to the Army Research Office. During the present reporting period, corresponding results for methane, ethane, and ethylene, were obtained as well the effects of different reaction rates on comparisons between predictions and measurements for all of the fuels tested.

The HPCEF was used to study the structures and extinction conditions of counterflow diffusion flames in air for nitrogen-diluted methane, ethane, and ethylene, from 0.1 MPa to 2.0 MPa. Besides employing thermocouples to measure temperature profiles, strain rates at extinction were measured and compared with predictions of two different chemicalkinetic mechanisms (San Diego and USC). In addition, the nitrogen in the fuel and oxidizer streams was replaced by helium for one of the methane tests of extinction strain rate as a function of pressure. In all cases, the strain rate at extinction was found to increase with pressure up to about 0.30.5 MPa and to decrease with pressure thereafter, on up to 2.0 MPa, although with helium there was a clear leveling tendency beyond 1.0 MPa. While these behaviors were in qualitative agreement with most predictions of the chemical kinetic mechanisms, in a number of cases the quantitative discrepancies were well beyond the experimental uncertainty. The experimental study showed that pressure has a substantial effect on critical extinction conditions for gaseous hydrocarbon diffusion flames. Chemical kinetic mechanisms were found to perform with varying success, which is not surprising since this is the first study addressing the extinction of highly diluted counterflow diffusion flames for low-molecular weight hydrocarbon fuels at elevated pressures. Minor revisions to San Diego mechanism for hydrocarbon reactions substantially improved agreement for methane flames, but further investigations of rate parameters for steps involving carbon-containing species definitely are warranted, aimed at improving the performance of the mechanism at high pressure.

More details are available in U. Niemann, K. Seshadri, and F. A. Williams, "Methane, Ethane, and Ethylene Laminar Counterflow Diffusion Flames at Elevated Pressures: Experimental and Computational Investigations up to 2.0 MPa ," *Combustion and Flame,*, **161**, 2014, pp 138—146.

2.2 Experimental Investigations of the Influence of Pressure on Critical Extinction Conditions of Laminar Nonpremixed Flames Burning Condensed Hydrocarbon Fuels, Jet Fuels, and Surrogates

Numerous experimental, computational and analytical studies have addressed combustion of various hydrocarbon fuels at elevated pressures. These studies include combustion in shock tubes and flowreactors and counterflow nonpremixed and have illuminated the influence of pressure on combustion. In the previous sub-section we reported on critical conditions of extinction of methane, ethane, and ethylene flames at elevated pressures. There are, however, very few studies of extinction of high molecular weight hydrocarbon fuels in nonuniform flows

at high pressure. In this section critical conditions of extinction are reported for nonpremixed combustion of various condensed hydrocarbon fuels, jet fuels, and surrogates at moderate pressure.

Critical conditions of extinction were measured for high molecular weight hydrocarbon fuels, jet fuels and surrogates at pressures up to 0.4 MPa. The hydrocarbon fuels tested were n-heptane, cyclohexane, n-octane, iso-octane, and n-decane. Jet fuels tested include JP-8 and Jet-A. The surrogates tested are the Aachen surrogate, consisting of 80,% n-decane and 20 % 1,3,5-trimethylbenzene by mass, and the 2nd generation POSF 4658 Princeton surrogate consisting of 49.6 % n-dodecane, 24.3 % iso-octane, 19.8 % n-propylbenzene, and 6.3 % 1,3,5-trimethylbenzene by mass. The counterflow, condensed-fuel configuration is employed. Air diluted with nitrogen at 298 K is injected onto the surface of a pool of heptane. The mass fraction of oxygen in the oxidizer stream is represented by $Y_{O_2,2}$. A flame is stabilized in the stagnation point boundary layer that is established above the liquidgas interface. At a selected value of pressure p, and at a selected value of $Y_{O_2,2}$, the flow velocity of the oxidizer stream is increased until extinction takes place. The strain rate at extinction was calculated. The experiment is repeated for a range of pressures. The general ordering of extinction strain rates of hydrocarbon fuels was observed and found to be in general agreement with the predictions of kinetic models and experiments conducted at atmospheric pressure in earlier experiments and computations. An initial linear increase of extinction strain rate with pressure is observed at pressures up to 0.175 MPa, followed by a general flattening of the curves up to 0.35 MPa. At pressures above 0.35 MPa, extinction strain rates of some fuels begin to decrease with increased pressures. These general trends are consistent with results previously measured for n-heptane, n-hexane, and n-decane flames in a similar configuration.

With the same experimental setup, the viability of select surrogates was investigated by comparing their extinction curves to that of JP-8 and Jet-A, the target fuels to be emulated. The critical conditions of extinction of the 2nd generation POSF 4658 Princeton surrogate closely resembled that of JP-8 at moderate pressures. The observation may be attributed to its 4-component composition, which provided a greater diversity in molecular structure and allowed for the formation of a variety of intermediate species that more closely mimicked those produced by the combustion of actual jet fuel.

More details are available in R. Gehmlich, A. Kuo, K. Seshadri, "Experimental Investigations of the Influence of Pressure on Critical Extinction Conditions of Laminar Nonpremixed

Flames Burning Condensed Hydrocarbon Fuels, Jet Fuels, and Surrogates," *Proceedings of the Combustion Institute,* **35**, 2015, pp 937-943.

2.3 Rate-Ratio Asymptotic Analysis of the Influence of Addition of Hydrogen on the Structure and Mechanisms of Extinction of Nonpremixed Methane Flames

As mentioned before JP-8 is a mixture of numerous aliphatic and aromatic compounds. Therefore improved understanding of combustion of fuel mixtures, in particular the influences of individual components of the fuel mixture on the overall combustion of the multicomponent fuel is necessary. In this section we report on the influence of hydrogen on combustion of mixtures of methane and hydrogen. It is well established that rate-ratio asymptotic techniques are powerful tools for analyzing combustion of fuel mixtures.

Rate-ratio asymptotic analysis was carried out to elucidate the influence of hydrogen on the structure and critical conditions for extinction of nonpremixed methane flames. Steady, axisymmetric, laminar flow of two counterflowing streams toward a stagnation plane was considered. One stream, called the fuel stream was made up of a mixture of methane (CH_4) and nitrogen (N_2). The other stream, called the oxidizer stream, was a mixture of oxygen (O_2), and N_2 . Hydrogen (H_2) was added either to the oxidizer stream or to the fuel stream. A reduced mechanism of four global steps was employed in the analysis. Chemical reactions are presumed to take place in a thin reaction zone that is established in the vicinity of the stagnation plane. On either side of this thin reaction zone, the flow field is inert. These inert regions represent the outer structure of the flame. The reactants, CH_4, O_2 , and H_2 are completely consumed at the reaction zone. The outer structure was constructed employing a Burke-Schumann (flame-sheet) formulation. It provides matching conditions required for predicting the structure of the reaction zone. In the reaction zone, chemical reactions are presumed to take place in two layers: the inner layer and the oxidation layer. In the inner layer fuel (methane) is consumed and the intermediate species hydrogen and carbon monoxide are formed. These intermediate species and added hydrogen are oxidized in the oxidation layer to water vapor and carbon dioxide. Critical conditions of extinction were predicted from results of the asymptotic analysis and found to agree well with previous measurements. Addition of hydrogen to methane flames promotes combustion by delaying extinction. An important finding of the asymptotic analysis is that the mechanisms by which hydrogen promotes combustion when it is added to the oxidizer stream is different from that when it is added to the

fuel stream.

A key outcome of this work is that considerable simplifications can be introduced to model combustion of multicomponent fuels made of many hydrocarbon compounds. Each component of the fuel reacts with radicals to form carbon monoxide and hydrogen. Carbon monoxide and hydrogen are subsequently converted to carbon dioxide and water vapor.

More details are available in K. Seshadri, and X. S. Bai, "Rate-Ratio Asymptotic Analysis of the Influence of Addition of Hydrogen on the Structure and Mechanisms of Extinction of Nonpremixed Methane Flames," *Combustion Science and Technology,* **187**, 2015, pp 3-26.

2.4   Accuracies of Laminar Counterflow Flame Experiments

Steady counterflows and their variants, such as stagnation flow normal to an inert, impermeable, flat plate or normal to the surface of a solid or liquid-pool fuel, are increasingly becoming the configuration of choice in this quest for greater accuracy. This configuration is used in the work reported here. Counterflow configurations are useful for investigating the structures of premixed, non-premixed, and partially premixed flames. Ignition and extinction conditions also are readily measured in this configuration. A key advantage is that counterflows enable steady combustion processes to be established away from complicating influences of walls; there is no need to address stabilization-region effects of rim-stabilized or rod-stabilized flames. Another is the inherent stability of the counterflow. Use of counterflow combustion experiments to test underlying predictions of these chemically reacting flows requires the availability of numerical methods for solving the sets of partial differential equations that describe the flow. A number of computer codes of this type are now available for solving counterflow combustion problems, such as Chemkin, OpenSMOKE, Cosilab, FlameMaster, Cantera, and LOGEsoft. This strongly motivates designing counterflow experiments that obey the conditions required for accurate descriptions in terms of ordinary differential equations. The work reported here addressed the accuracy with which this objective can be obtained.

There is a wide range of different possible designs of apparatus that can be used experiments employing the counterflow configuration. The choices vary from opposing nozzle flows without any flow-smoothing screens to opposing flows through porous plates. It is desirable to select designs that correspond best to the conditions treated in available codes for calculating reacting flows because this facilitates comparisons of experimental and computational results.

The most convenient codes to use are for steady laminar flows with one-dimensional scalar fields, and they often impose rotational plug-flow conditions at the boundaries. Accuracies of axisymmetric counterflow flame measurements in experiments intended to conform to these conditions are estimated here for designs of large aspect ratios with straight-duct feed streams that have multiple-screen flow-smoothing exits. Causes of departures from assumptions underlying computational programs are addressed by methods that involve theoretical analysis, experimental measurement, and axisymmetric computation.

It concluded from the work that both screened ducts and contoured nozzles offer useful tools for investigating combustion processes, to test knowledge of associated transport-property and chemical-kinetic parameters by comparing experimental results with predictions of computer programs based on assumptions of one-dimensional temperature and concentration fields. In such comparisons, it is best to account for the radial gradient of the radial component of the velocity when contoured nozzles are employed, but plug-flow boundary conditions apply with good accuracy for screened ducts. The departures from plug-flow conditions in screened-duct devices generally are too small to be determined accurately enough to justify use of any other boundary condition at the screen exits. Accuracies are such that errors are less than 5 % in well-designed screened-duct experiments.

More details are available in U. Niemann, K. Seshadri, and F. A. Williams, "Accuracies of Laminar Counterflow Flame Experiments," *Combustion and Flame,* **162**, 2015, pp 1540-1549.

2.5   Autoignition of n-Heptane at Moderate Pressures

An apparatus was constructed for measuring critical conditions of autoignition of condensed fuel, at moderate pressure. The counterflow configuration was employed. In this configuration a laminar flow of air is directed over the vaporizing surface of the condensed fuel. The burner is made up of a cup into which condensed fuel is introduced at a rate that is equal to the rate of vaporization, so that the position of the liquid-gas interface is maintained at a constant level. Heated air is injected from a duct that is placed directly above the surface of the liquid pool. A mixing layer is established in the vicinity of the liquid gas interface. Autoignition takes place in this layer. It has been shown that the characteristic residence time is given by the reciprocal of the strain rate $a_2 = 2V_2/L$, where V_2 is the speed at which air is injected from the duct, and L is the distance between the liquid-gas interface and the exit of the duct. The counterflow burner is placed inside the HPCEF for carrying out experiments at elevated

pressures. The chamber in the HPCEF has optical access via four view-ports with fused silica windows. The pressure in the chamber is maintained constant during experiments using a TESCOM PID-control pressure regulation system. Air is heated in two stages. First it flows through three process heaters with a power of 750 watts each and a maximum exit temperature of 800 K. Next, air is heated using spiral silicon carbide heating element with power rating of 4800 watts. The surface temperature of the heating element can attain a maximum value of 1900 K. To prevent heat loss the duct is surrounded by a 2260 watts cylindrical ceramic heating furnace that can reach a surface temperature of 1200 K. A fused quartz tube separates the oxidizer stream from the nitrogen curtain. Another quartz tube separates the nitrogen curtain from the surrounding. The whole assembly consists of machined aluminum and stainless steel parts. Where necessary the parts are cooled with deionized water. Experimental measurements will include the temperature of air at autoignition. The next section describes experimental data for autoignition obtained using this apparatus.

More details are available in G. Mairinger, R. Gehmlich, E. Pucher, K. Seshadri, "Autoignition of n-Heptane at Moderate Pressures," Paper # 114LF-0394, 9th US National Combustion Meeting, Central States Section of the Combustion Institute, May 17-20, 2015, Cincinnati, Ohio.

2.6 Autoignition of Condensed Hydrocarbon Fuels in Nonpremixed Flows at Elevated Pressures

Fundamental knowledge of mechanisms of autoignition of condensed hydrocarbon fuels at elevated pressures in nonuniform flows is essential for accurate prediction of chemical processes taking place in propulsion systems. In contrast to numerous studies of autoignition of high molecular weight hydrocarbon fuels at elevated pressures in homogeneous systems, there are very limited studies on autoignition of these fuels in nonuniform flows. A noteworthy finding in a previous study supported by the Army Research Office, was that autoignition of condensed hydrocarbon fuels in nonuniform flows at atmospheric pressure was promoted by low temperature chemistry. The study described here addressed autoignition at elevated pressures.

Experimental and computational investigation was carried out to elucidate the fundamental mechanism of autoignition of n-heptane, n-decane, and n-dodecane in nonpremixed flows at elevated pressures up to 6 bar. The counterflow configuration was employed. In this configuration a axisymmetric flow of a gaseous oxidizer stream is directed over the surface of an

evaporating pool of a liquid fuel. The oxidizer stream was a mixture of oxygen and nitrogen. The experiments are conducted at a fixed value of mass fraction of oxygen and at a fixed low value of the strain rate. The temperature of the oxidizer stream at autoignition, T_{ig} , was measured as a function of pressure, p. Computations were carried out using skeletal mechanisms constructed from a detailed mechanism and critical conditions of autoignition were predicted. The experimental data and predictions show that for all fuels tested T_{ig} decreases with increasing p. At a fixed value of p, T_{ig} for n-dodecane was the lowest followed by n-decane and n-heptane. This indicates that n-dodecane is most easy to ignite followed by n-decane and n-heptane. This is in agreement with previous experimental and computational studies at 1 atm where a similar order of reactivities for these fuels were observed at low strain rates. Flame structures at conditions before and at conditions immediately after autoignition were calculated. A noteworthy finding is that low temperature chemistry was found to play a dominant role in promoting autoignition. The influence of low temperature chemistry was found to increase with increasing pressure.

More details are available in G. Mairinger, A. Frassoldati, R. Gehmlich, U. Niemann, A. Stagni, E. Ranzi, K. Seshadri, "Autoignition of Condensed Hydrocarbon Fuels in Nonpremixed Flows at Elevated Pressures," *Combustion Theory and Modelling,* **in press**, 2016

Methane, ethane, and ethylene laminar counterflow diffusion flames at elevated pressures: Experimental and computational investigations up to 2.0 MPa

CrossMark

Ulrich Niemann *, Kalyanasundaram Seshadri, Forman A. Williams

University of California, San Diego, Department of Mechanical and Aerospace Engineering, 9500 Gilman Drive, La Jolla, CA 92093-0411, United States

ABSTRACT

A newly designed high-pressure combustion facility was used to study the structures and extinction conditions of counterflow diffusion flames in air for nitrogen-diluted methane, ethane, and ethylene, from 0.1 MPa to 2.0 MPa. Besides employing thermocouples to measure temperature profiles, strain rates at extinction were measured and compared with predictions of two different chemical–kinetic mechanisms (San Diego and USC). In addition, the nitrogen in the fuel and oxidizer streams was replaced by helium for one of the methane tests of extinction strain rate as a function of pressure. In all cases, the strain rate at extinction was found to increase with pressure up to about 0.3–0.5 MPa and to decrease with pressure thereafter, on up to 2.0 MPa, although with helium there was a clear leveling tendency beyond 1.0 MPa. While these behaviors were in qualitative agreement with most predictions of the chemical–kinetic mechanisms, in a number of cases the quantitative discrepancies were well beyond the experimental uncertainty. This underscores the desirability of improving chemical–kinetic descriptions for applications at elevated pressures. Such improvements for the San Diego mechanism are introduced here for two of the steps involving hydroperoxyl that become increasingly important with increasing pressure.

© 2013 The Combustion Institute. Published by Elsevier Inc. All rights reserved.

1. Introduction

The ability of chemical–kinetic mechanisms and transport descriptions to predict combustion processes is tested most easily and accurately by well-controlled laboratory experiments performed at normal atmospheric pressures, where measurements of strain rates at extinction, in particular, provide relevant tests of chemical–kinetic descriptions. In many practical applications, however, the combustion occurs at elevated pressures. Since the combustion chemistry varies with pressure, often non-monotonically in certain respects, it is desirable to pursue correspondingly well-controlled laboratory combustion experiments at pressures above atmospheric, as further tests of predictions. But such experiments, unfortunately, are difficult and expensive to design and perform. We have recently constructed a high-pressure combustion facility in which experiments on laminar counterflow diffusion flames were carried out. Results of these experiments with hydrogen as the fuel have recently been published [1]. In the present paper we report and discuss corresponding results for methane, ethane, and ethylene, as well as showing the effects of

different reaction rates on comparisons between predictions and measurements for all of the fuels tested.

There have been a number of previous high-pressure counterflow experimental studies. Niemann et al. [1] recently carried out experiments on hydrogen flames at pressures up to 1.5 MPa, measuring temperature profiles and providing experimental confirmation for the non-monotonic pressure dependence of extinction strain rates predicted computationally by Sohn and Chung [2]. In addition, Figura and Gomez [3] successfully stabilized non-premixed methane flames at elevated pressures up to 3.0 MPa. Their experiments were conducted with the fuel and oxidizer streams diluted with either nitrogen or helium. Temperature profiles were measured and compared with predictions [3], but extinction strain rates were not addressed. On the other hand, Maruta et al. [4] earlier had measured critical conditions for extinction of non-premixed methane flames with the fuel and oxidizer streams diluted with carbon dioxide (CO_2) and with nitrogen at pressure up to 0.8 MPa. They found that for flames diluted with CO_2, critical conditions for extinction were influenced by radiation re-absorption, but they did not specifically discuss variations of the extinction strain rates with pressure. Böhm and Lacas [5] also measured critical conditions for extinction of non-premixed methane flames up to pressures of 0.6 MPa. Their emphasis was on soot formation and destruction,

but they did demonstrate experimentally that with increasing pressure, the measured strain rate at extinction first increased and then decreased. Their computations with detailed chemistry also showed an increase in the value of the strain rate at extinction with increasing pressure followed by a decrease, but the decrease was less pronounced than that measured [5].

Much earlier than these investigations, Sato [6] had measured critical conditions for extinction of non-premixed methane and ethane flames at pressures up to 10 MPa. These measurements were made on flames stabilized over the surface of a porous cylinder (a Tsuji burner), and they showed that with increasing pressure, the strain rates at extinction for methane and ethane remained constant for pressures up to 2.0 MPa and 1.0 MPa, respectively, but with further increase in pressure, up to 10 MPa, the strain rate at extinction decreased [6]. This qualitatively different behavior at the lower pressures may be associated with the fact that the fuels in these experiments were not diluted, resulting in strain rates at extinction that were quite appreciably higher. There also have been experiments on liquid-fuel flame extinction in stagnation-point flows of alkanes, performed at about the same time, at pressures up to 2.0 MPa [7,8] that show regions of increasing extinction strain rates, leading up to a plateauing peak region, followed by a downward-sloping region as pressure is increased, qualitatively similar to the results with diluted methane. In the present work critical conditions for extinction and flame-temperature profiles are determined for an appreciably wider range of gaseous-fuel parameters than is available in this literature.

2. Experimental facility and procedures

Figure 1 is a schematic illustration of the experimental facility. It shows the pressure chamber, the gas-supply system, and the data-acquisition and control system. The counterflow burner is placed inside the chamber. The inner diameter of the fuel and oxidizer ducts of the counterflow burner is 20 mm, and the separation distance between the ducts is 10 mm. Gaseous fuel mixed with inert gas is injected from the bottom duct and diluted oxidizer from the top duct. Fine wire screens are placed at the exits of the both ducts. This makes the tangential component of the flow velocity negligibly small at the exit of the ducts, establishing plug flow. The reactant ducts are surrounded by annular shrouds that provide an inert curtain flow to minimize the influence of ambient gas on the reaction zone. The products of combustion are removed into an exhaust-treatment system where they are cooled before they are purged into the in-house exhaust system. This prevents hot gases and water vapor from accumulating inside the pressure chamber. As a consequence, the temperature in the chamber does not increase, and condensation of water vapor on the chamber walls and windows is avoided.

Gases to the pressure chamber are supplied from standard compressed gas cylinders. All gaseous streams are controlled by computer-regulated mass-flow controllers. The selection of the type of mass-flow controller for a given reactant depends on the required experimental range of flow rates. The mass-flow controllers employed here have maximum flow rates in the range of 30–500 standard liters per minute and operating pressures up to
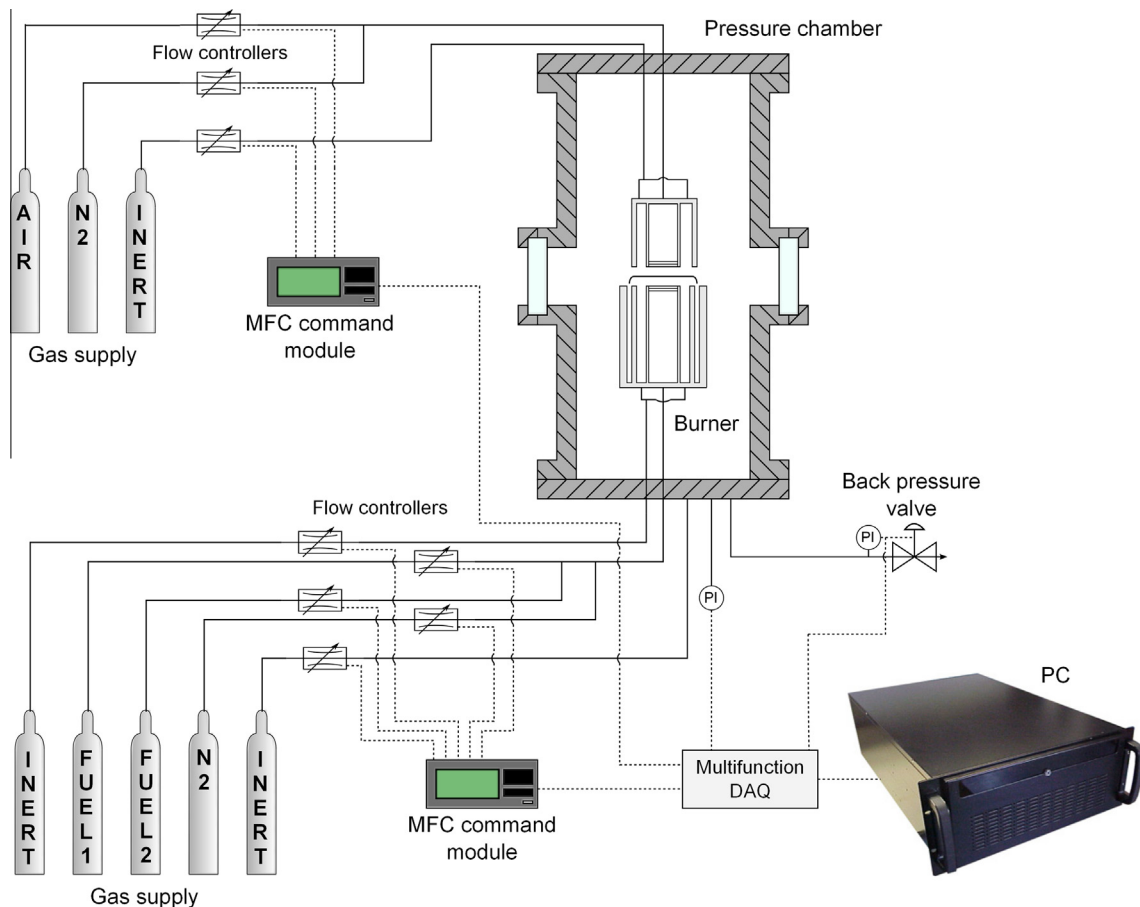

Fig. 1. Schematic illustration of the experimental arrangement. The burner is housed inside a pressure chamber, with optical access. The gas-supply system includes the mass-flow controllers and mass-flow-controller (MFC) command modules, as well as the data-acquisition and control systems.

3.5 MPa. The mass-flow controllers are calibrated using a pulse-generating wet-test meter. Pressure-dependent inaccuracies of the mass-flow controllers were found to be minuscule. The accuracy of the measured values of the volumetric flow rates is expected to be within 1% of the set flow rate. The velocities of the reactants at the exit of the ducts are presumed to be equal to the quotient of the measured volumetric flow rates of the reactants and the cross-sectional area of the ducts, corresponding to plug flow pressure.

Figure 2 shows a photograph of a diluted ethane-air counter-flow diffusion flame stabilized in this new high-pressure experimental facility. During operation inert gas is introduced into the chamber to establish and maintain the pressure at the desired level, while balancing the inflow of reactants with the outflow of exhaust gases and excess inert gas from the chamber. An electronic PID back-pressure regulator is employed to maintain the pressure in the chamber to a high degree of accuracy. The chamber pressure is independently monitored and recorded with digital pressure transducers having an accuracy within 0.1%. An ignition system was developed to establish a stable flame in the reaction zone of the counterflow burner. Since it is crucial that the flow field is not obstructed during the experiment, a surface igniter is mounted on a pivot arm that is moved by a miniature stepper motor. To ignite a flame the igniter is pivoted into the reaction zone. After the flame is established the igniter is retracted back into its initial position outside the flow field. An industrial computer equipped with a National Instruments PXI system is used as a central control and data-acquisition unit. Several virtual instruments running on a Labview platform were programmed to allow integration of multiple processes into customized controls.

Experimental conditions are established, controlled, and recorded remotely through virtual instrumentation. At the beginning of the experiments, the chamber is filled with nitrogen to the desired operating pressure. When pressure conditions are reached, the flow field is established by introducing the reactants into the counterflow burner at the desired flow rates. After establishing a steady flame the strain rate is increased, while keeping the momenta of the two streams balanced, until flame extinction takes place. Increments to increase the strain rate are selected to be sufficiently small and separated by enough time so that a steady state is achieved after each step. Tests were performed to ensure that stepping-inflicted flow perturbation is not the cause for flame extinction. The flow rates and hence the strain rate at extinction are recorded as functions of pressure and composition of the reactants.

Temperature profiles are measured using two Pt–Pt 13%Rh thermocouples. One of the thermocouples employed had a wire diameter of 75 μm and a torch-welded spherical bead with a size of 180 μm, and a second one had a 25μ spot-welded cylindrical junction. The results reported here were obtained with the smaller one, the larger one being used in estimating corrections. The thermocouple was mounted on an XY-stage that is controlled by stepper motors inside the pressure chamber. The probe is programmed to move vertically at a radial distance of 3 mm from the axis of symmetry to minimize flow-field perturbations. The flame is approached from the bottom (fuel duct), covering a total traverse distance of 7 mm. The probe then approaches the flame from the top in a similar manner. This method was used to rule out previously reported effects of flame shift caused by the presence of the thermocouple. Measured temperatures are corrected taking into consideration the radiative heat losses from the thermocouple [9] with a resulting correction less than 20 K at the highest temperature. The estimated error in the temperature measurements will be discussed in more detail in the following sections.

The experimental accuracies of the flow velocities, the reactant mass fractions and the pressure are ±1%, ±3% and ±1% of the recorded value, respectively. Experimental repeatability of the strain rate at extinction is within ±2% of the recorded value. For the burner used in this study, the deviation of the established flowfield from pure plug flow, resulting in a lower strain rate, can be estimated to be within 10% based on theoretical estimates and particle-streak photographs of the flow.

3. Experimental conditions

Figure 3 is a schematic illustration of the counterflow configuration. Fuel (CH_4, C_2H_4, C_2H_6) mixed with an inert gas (N_2, He) is injected from the fuel duct and an oxygen-inert mixture is injected from the oxidizer duct. The reactant streams flow toward a stagnation plane. The momenta of the two streams are balanced to maintain the stagnation plane at the center of the two boundaries. The mass fraction of the fuel, the temperature, and the component of the flow velocity normal to the stagnation plane at the fuel boundary are denoted by $Y_{F,1}$, T_1 and V_1, respectively, this same notation with the subscript 2 being employed for quantities at the oxidizer boundary. The distance between the fuel boundary and the oxidizer boundary, denoted by L, is $L = 10$ mm in these experiments.

The strain rates reported here are

$$a_2 = \frac{2|V_2|}{L}\left(1 + \frac{|V_1|\sqrt{\rho_1}}{|V_2|\sqrt{\rho_2}}\right). \tag{1}$$

Here ρ_1 and ρ_2 represent the density of the mixture at the fuel boundary and at the oxidizer boundary, respectively. All quantities appearing here are readily evaluated from the experiment, and in comparisons with computations these same values are employed
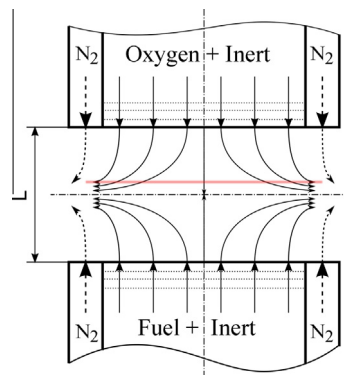

Fig. 2. Photograph of an non-premixed ethane-air flame with a fuel mass fraction $Y_{F,1}$ = 0.14 at 0.8%MPa.

Fig. 3. Schematic illustration of the counterflow flow field.

in the plug flow code. An asymptotic analysis for large injection Reynolds numbers of the laminar plug flow with boundary-layer displacement effects at the flame neglected has shown that this corresponds to the local strain rate on the air side of stagnation plane in that limit [10] as explicitly indicated later [11]. The momentum balance imposed experimentally gives $\rho_1 V_1^2 = \rho_2 V_2^2$, which when substituted in Eq. (1) results in $a_2 = 4V_2/L$.

Critical conditions for extinction in these experiments depend on the six quantities $Y_{F,1}, T_1, Y_{O_2,2}, T_2, a_2$, and pressure p. The strain rate, a_2, is determined by V_2 given the momentum balance. The main experiments were conducted with air as the oxidizer, $Y_{O_2,2} = 0.233$, and inlets at room temperature $T_1 = T_2 = 298$ K. Therefore, at any given value of $Y_{F,1}, a_2$ will depend only on p. The fuel mass fractions selected in these experiments were $Y_{F,1} = 0.16$ for methane, $Y_{F,1} = 0.12$ for ethane, and $Y_{F,1} = 0.09$ for ethylene. These conditions result in stoichiometric mixture fractions of $Z_{st} = 0.267$ for methane, $Z_{st} = 0.342$ for ethane and $Z_{st} = 0.428$ for ethylene, given by

$$Z_{st} = \left[1 + \frac{\nu Y_{F,1}}{Y_{O_2,2}}\right]^{-1} \qquad (2)$$

where ν is the stoichiometric oxygen-to-fuel mass ratio. The resulting values of the stoichiometric mixture fraction indicate that the flame will be located on the oxidizer side of the stagnation plane. In addition to measuring the extinction value $a_{2,E}$ as a function of p for fixed $Y_{F,1}$, for methane at two different pressures, $a_{2,E}$ was measured as a function of $Y_{F,1}$. The reported temperature profiles were measured at a fixed value of the strain rate $a_2 = 120$ s^{-1} and for various values of pressures. For flames of all fuels at the conditions investigated here, no visible soot formation was observed.

4. Computational approach

In investigating ranges of variations of predictions of different chemical–kinetic and transport descriptions for these experiments, the commercial computer code ChemkinPro [12] was exercised with the aforementioned plug-flow boundary conditions for two different schemes, the San Diego mechanism [13] and the USC II mechanism [14], hereafter identified simply as USC. The differences in these two sets of predictions are comparable with differences encountered in computations with other descriptions, as was verified by a few additional calculations. The USC mechanism was selected for further study along with the San Diego mechanism because of its excellent initial agreement with the present high-pressure methane extinction data. Differences in the description were maximized in that the USC mechanism was employed along with its relatively newly developed transport description, while the San Diego mechanism was used with the much older Chemkin mixture-averaged transport. Transport descriptions were observed to be relevant in that, for example, computations with the San Diego mechanism using the Chemkin multicomponent diffusion description introduced differences, always lowering the predicted extinction strain rates, comparable with differences of the predictions of the two chemical–kinetic mechanisms. For example, for the present methane-air experiments, the extinction strain rates predicted with multicomponent transport are lower by 15 s^{-1} at 0.1 MPa and by 30 s^{-1} at 0.5 MPa and above. All of the reported results included both Soret diffusion and radiant loss, the latter always found to be of lesser importance, but the former being non-negligible, although not to the extent of the differences between mixture-averaged and multicomponent transport. Interpretations of results and conclusions concerning effects of different values for chemical–kinetic rate parameters must thus be tempered by these underlying uncertainties in the transport description.

Some of the initial computations were made with the code OpenSMOKE [15,16], but later only ChemkinPro was used because of its multicomponent-diffusion option. Results obtained with the two different codes were in agreement, supporting code-independence. Computational tests always were made to assure sufficient spatial resolution that predictions were independent of grid size. This is especially important at increased pressures because of the associated reduced thickness of the flame. To account for the resulting strong gradients within the computational domain, adaptive meshing techniques were used. The resulting non-uniformly spaced grids of up to 300 points were found to resolve the reaction zone sufficiently.

5. Temperature profiles

Temperature profiles are shown in Fig. 4 for methane flames and in Fig. 5 for ethane flames at values of pressures of 0.2, 0.4 and 0.8 MPa and fixed $a_2 = 120$ s^{-1}. Standard radiation corrections [9] were employed, and catalytic effects were estimated to be negligible. Unlike extinction strain rates, the computational results in these papers are only weakly dependent upon the chemical–kinetic and transport descriptions, except very near the peak temperature. The profiles show that the gradients of temperature with respect to the spatial coordinate are zero at the oxidizer and fuel boundaries. The flames are therefore considered to be without heat loss to the nozzles. While exhibiting generally good agreement between measurements and predictions, measured temperature profiles are noticeably wider. For CH_4 the width is in average 12% higher and for C_2H_6 15% higher than the computed profiles, percentages that tend to increase with pressure. The finite size of the thermocouple causes the profiles to be smoothed in regions of high curvature, such as at the peak and near the flame boundaries. This effect, however, is expected to cancel for points in regions of linear temperature gradients. Hence it does not provide a reasonable explanation for the widened profiles.

The possible effects of absorption of flame radiation by the thermocouple wires are not included in the standard radiation corrections and have not been discussed in the literature for
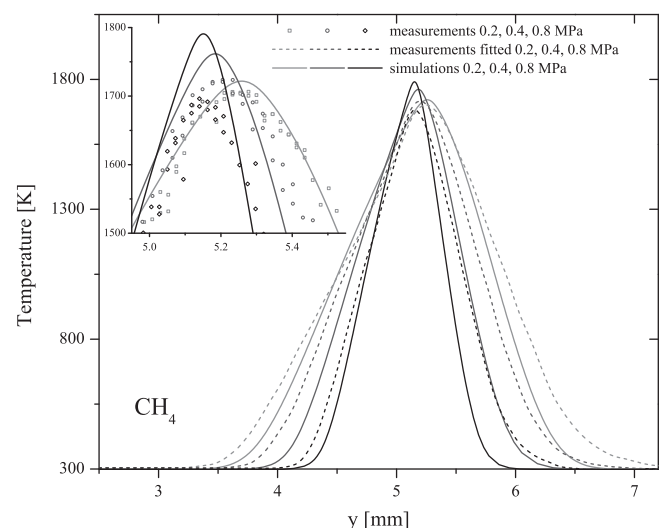

Fig. 4. Profiles of temperature as a function of distance from the fuel boundary for methane diffusion flames at fixed $Y_{F,1} = 0.16$ at 0.2, 0.4, and 0.8 MPa. The strain rate is $a_2 = 120$ s^{-1}, and the stoichiometric mixture fraction is $Z_{St} = 0.267$. Solid [——] curves are obtained computationally using San Diego mechanism with mixture-averaged diffusion. In the main plot, experimental data are represented by dashed [- - -] curves as a best fit, and the actual data points around the temperature peak are shown in the subplot.
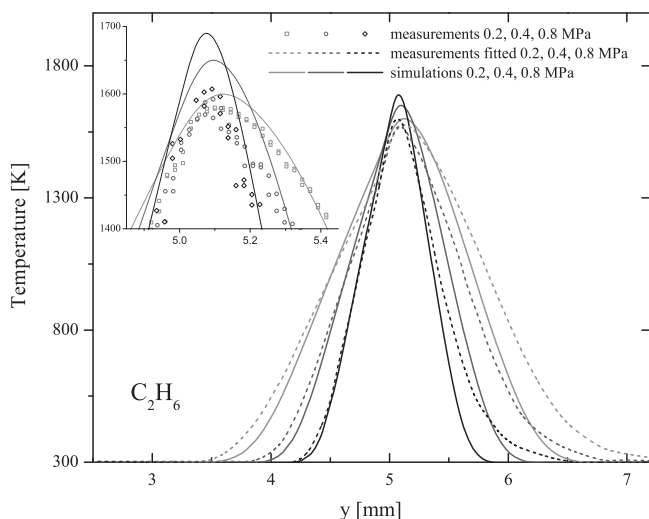
Fig. 5. Profiles of temperature as a function of distance from the fuel boundary for ethane diffusion flames at fixed $Y_{F,1} = 0.14$ at 0.2, 0.4 and 0.8 MPa. The strain rate is $a_2 = 120\,s^{-1}$, and the stoichiometric mixture fraction is $Z_{St} = 0.302$. Solid [——] curves are obtained computationally using San Diego mechanism with multi-component diffusion. In the main plot, experimental data are represented by dashed [- - -] curves as a best fit, and the actual data points around the temperature peak are shown in the subplot.

measurements of the present kind in the counterflow configuration. Flame radiation absorbed by the wires can heat them above the local gas temperature, causing the thermocouple temperature reading to be too high. Equating the radiant heat input rate to the wire to the product of the temperature difference between the wire and the gas, the wire surface area and the convective/conductive heat-transfer coefficient of the surrounding gas provides an estimate of the temperature increase of the thermocouple measurement associated with this effect. The first step in making such estimates is to calculate the radiant heat flux from the flame.

These counterflow-flame hot zones are quite accurately optically thin, and they radiate predominantly in CO_2 and H_2O bands. Planck-mean absorption coefficients for these bands, obtained from the ploynomial fits of RADCAL [17,18], were employed along with the calculated profiles of partial pressures of CO_2 and H_2O and of temperature from the San Diego mechanism to obtain the radiant fluxes from three of our counterflow flames. The results are
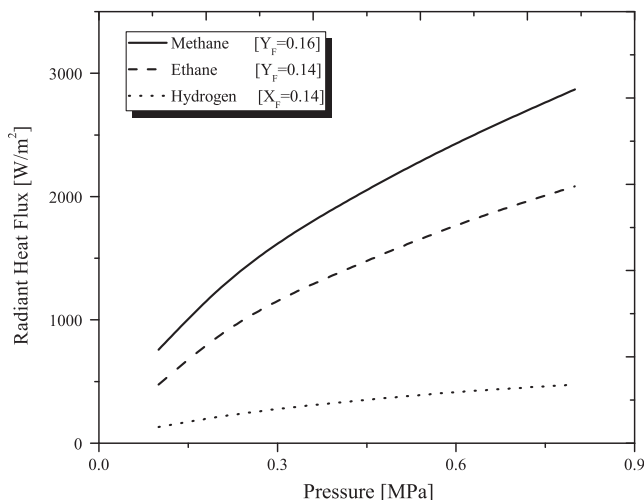

Fig. 6. Calculated values of radiative heat flux from the flame as a function of pressure for three fuels in the counterflow experiments.

shown in Fig. 6, where ethane lies below methane partially because of the greater degree of dilution of the fuel, and hydrogen lies well below the other two partially because of the absence of the CO_2 bands, consistent with measurements [1] not exhibiting significant widening for this fuel. These results are only estimates, but the values are of an order of magnitude that is consistent with the radiant-loss corrections available in Chemkin and OpenSmoke, which are somewhat lower, sometimes as much as a factor of two, but not more than that. The curves in Fig. 6 increase with pressure approximately in proportion to $p^{\frac{2}{3}}$, which may be compared with the estimated [19] $p^{\frac{1}{2}}$ increase of the heat-release rates in counterflow flames, the difference likely associated with relative increases in temperature and CO_2 and H_2O mole fractions.

Heat-transfer coefficients are dominated largely by the thermal conductivity of the gas, which increases with temperature. If the results in Fig. 6 are employed in the energy balance, with an emissivity (equal to absorptivity) of the platinum wire of 0.2 [20] then the heat-transfer coefficient in the flame is found to be high enough that the absorption of the flame radiation would increase the measured temperature by a few K at the most when the thermocouple is in the hot zone. When the thermocouple is outside the radiating region of the flame, its view factor is 0.5, and so it absorbs only about 10% of the radiant flux, but the lower thermal conductivity of the gas at such locations results in an estimated thermocouple temperature increase by a substantial amount, which increases rapidly with increasing distance from the flame, approaching as much as 300 K in the cold flows at the inlet boundaries. In an order-of-magnitude sense, this is consistent with the measured widening of the profiles in Figs. 4 and 5, but it certainly is not consistent with the observation that the measurements approach 300 K rather than 600 K at the vertical-distance values of 3 mm and 7 mm in these figures.

Although the uncertainties in these estimates are large, an inescapable conclusion is that if all of the flame radiation were incident upon the thermocouple wires in the colder regions of the flow, then the measured thermocouple temperature would be quite appreciably higher than the local gas temperature. The flame radiation therefore must be reabsorbed by the gas before reaching the colder regions. The CO_2 and H_2O absorptivities do in fact increase substantially with decreasing temperature, so that reabsorption of the flame radiation by the gas can reduce the outward radiant flux to such an extent that its influence on the thermocouple readings becomes negligible. This reabsorption is estimated to occur mainly at temperatures below 800 K. The fuels CH_4 and C_2H_6 also have infrared absorption bands that can absorb flame radiation, and that is consistent with the observation in Figs. 4 and 5 that the experimental widening is greater on the air side than on the fuel side. The widening thus is attributed here to influences of the flame radiation and its transport.

An implication of these observations is that it may be more accurate for some purposes to exercise flame codes without radiant loss included, although, as previously indicated, that effect is very small in the computations for the present flames. Accurate analyses of the thermocouple readings would be difficult to develop because they would require detailed computation of radiation transport, which are challenging and have many uncertainties. Such radiation-transport effects, however, besides influencing measurements with addition of carbon dioxide, as indicated by Maruta et al. [4], also likely affect the thermocouple measurements of Figura and Gomez [3].

As indicated by the previously stated values of the stoichiometric mixture fractions, the peak temperatures are expected to lie on the oxidizer side of the stagnation plane, which is located at $y = 5$ mm in Figs. 4 and 5, corresponding to $Z_{st} = 0.5$. This is indeed seen to be true in these figures, and, moreover, as pressure is increased, narrowing the flame, the peaks move closer to the

stagnation plane. It is of interest to investigate whether a scaling can be identified that will collapse these temperature profiles. According to Burke-Schumann theory, counterflow diffusion-flame length scales are proportional to the square root of the ratio of a diffusivity to the strain rate [21], which is proportional to $1/\sqrt{pa}$. Hence if x denotes the distance from the observed position of peak temperature, scaled temperature profiles should collapse when plotted against $\xi = x \cdot \sqrt{\frac{p \cdot a}{p_{ref} \cdot a_{ref}}}$, where p_{ref} and a_{ref} are arbitrary reference values, and x is in mm. The selections p_{ref}=0.1 MPa and a_{ref} = 120 s^{-1} are made here, and the nondimensional temperature is defined as $\theta = \frac{T-T_{min}}{T_{max}-T_{min}}$, where T_{max}, is the observed peak temperature and T_{min} is the feed temperature.

Figure 7 shows these plots, demonstrating good scalability for the flames investigated. The variations, most evident on the oxidizer side, are associated with the fact that radiative heating of the thermocouple, discussed above, does not obey this scaling but rather becomes relatively more prominent with increasing pressure. The computational profiles also are seen to obey this scaling reasonably well in Fig. 7, while exhibiting departures from experiments for the reasons discussed above.

The insets in Figs. 4 and 5 show clearly that as pressure increases the measured maximum flame temperature increasingly falls below that calculated. This, of course, is due to the fixed thermocouple size and the thinning of the flame. Figure 8 uses the information obtained from temperature profiles measured with two differently sized thermocouples to obtain a better estimate of the actual peak flame temperature. The use of two thermocouples is necessary because even the smallest commercially available R-type thermocouple with a wire diameter of 25 µm is comparable in size to the reaction-zone width at the higher pressures. The recorded temperature was plotted against the thermocouple diameter on a linear scale and extrapolated to zero diameter. This should produce a slight overestimate of the temperature that could have been improved by a nonlinear extrapolation if measurements with thermocouples of three different sizes were available. R-type thermocouples are generally considered to be accurate within 5 K, and the maximum difference between the measured and radiation-corrected temperatures is 25 K for the smaller and 150 K for the larger thermocouple for the highest temperatures measured in this study. The repeatability of measurements of the maximum temperature
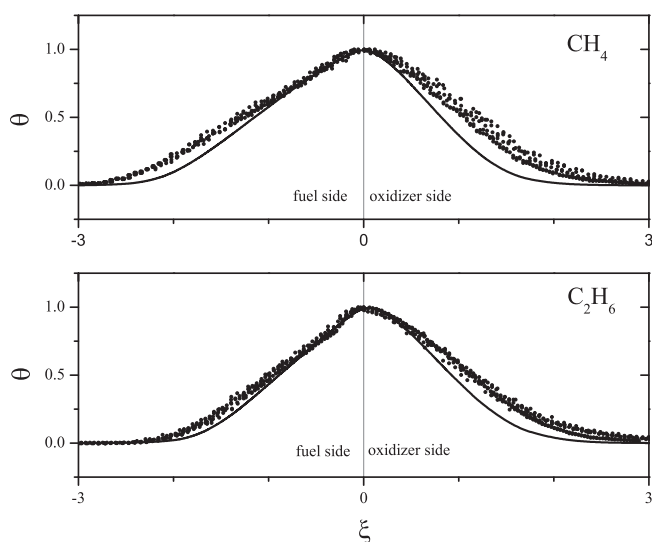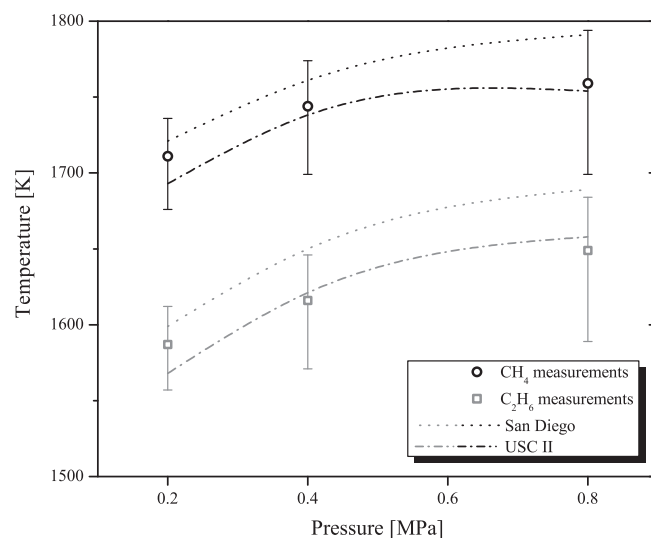

Fig. 8. The maximum temperatures plotted as a function of pressure for 0.2, 0.4 and 0.8% MPa for both methane (upper) and ethane (lower) diffusion flames at a_2= 120 s^{-1}. Open symbols denote extrapolated measurements, while computations are represented by a dotted [········] curve for San Diego mechanism with mixture-averaged diffusion and a dash-dotted [–·–·–] curve for USC-mech II.

is about ±10 K, better at greater flame thickness. Combining this information, it thus seems reasonable to estimate the accuracy of the temperature measurements conservatively to be within ±15 K for the small thermocouple and ±40 K for the large thermocouple in this high-temperature zone. Extrapolating these error margins provides error bars as shown in Fig. 8. The curves in the figures are the predictions of the San Diego mechanism with mixture-averaged diffusion and of the USC mechanism with multicomponent diffusion. With multicomponent diffusion the prediction of San Diego mechanism are quite close to the other. There thus appears to be reasonable agreement between the predictions and measurements of the peak temperature for both the absolute values and the trends with pressure.

6. Extinction conditions

Extinction conditions of diffusion flames are much more sensitive to the description of chemistry and molecular transport than are temperature profiles. Hence, obtaining reasonable good agreement between temperature profiles and numerical simulations is not a sufficiently conclusive validation for a chemical–kinetic scheme.

This becomes apparent in Fig. 9, which shows the strain rate at extinction, $a_{2,E}$, for diluted methane-air flames as a function of pressure, p, at fixed $Y_{F,1}$ = 0.16. With increasing pressure, the strain rate at extinction first increases, attains a maximum value at around 0.3 MPa and then decreases. This behavior may be associated with increasing bimolecular branching rates at the lower pressures then increasing three-body termination rates at the higher pressures. The agreement of the experimentally determined extinction strain rates with computations using the San Diego mechanism with mixture-averaged diffusion is within experimental accuracy up to about 0.7 MPa, but above this pressure the existing mechanism predicts an essentially constant extinction strain rate, contrary to experiment. Excellent agreement exists, however, between experiment and predictions of USC mechanism up to a pressure of 1.0 MPa. Experimentally, radial streaks were visible on the surface of the flame in the shaded region at pressures above 1.0 MPa. The streaks appeared to tend to align with the screen pattern, possibly resulting from the higher Reynolds numbers of the
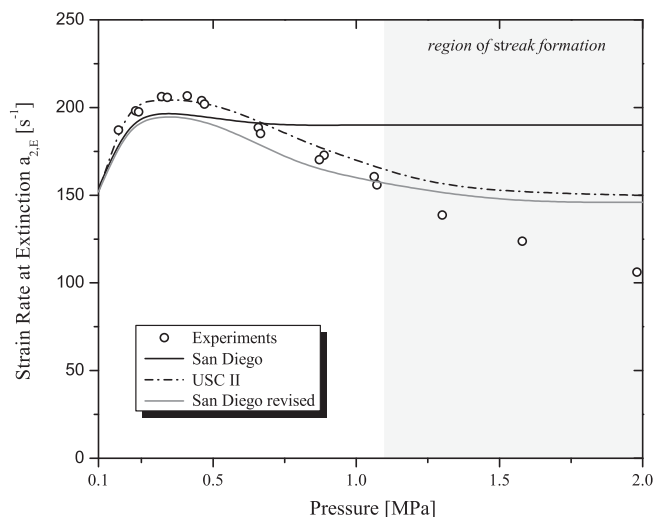

Fig. 7. Flame temperature measurements are plotted with the reduced temperature, θ, as function of a non-dimensional spatial coordinate, ξ, with the location of the peak temperature at 0; the lines are from computations.

Fig. 9. Experimentally obtained strain rates at extinction, $a_{2,E}$ for methane diluted with nitrogen as a function of pressure, p, at fixed $Y_{F,1} = 0.16$. The oxidizer is air. Open symbols represent experimental data, while computations are represented by a solid black [——] curve for San Diego mechanism with mixture-averaged diffusion and dash-dotted [-·-·-] curve for USC-mech II, and a solid gray [——] curve for the revised San Diego mechanism.

4.79×10^{13} cm³/mol s for the step $H_2O_2 + H \Leftrightarrow HO_2 + H_2$, employed in San Diego mechanism prior to 2011, but 2.1 times the current value in the mechanism, was re-introduced, there being uncertainty in this rate, with the current value the lowest in the literature. It is seen in Fig. 9 that, with these three revisions, the predictions of San Diego mechanism are quite close to those of the USC mechanism at the higher pressures and agree with the experimental results within experimental uncertainty. In previously published extinction strain rates for hydrogen [1], predictions of the San Diego mechanism with mixture-averaged transport were found to reflect the experimental pressure dependences well but to give strain rates greater than those found experimentally; possibly because of the transport descriptions. Computations show that these revisions to the mechanism have very little influence on these predictions, because the flame temperatures were lower in the hydrogen experiments, and the changes have little effect at lower temperatures.

The aforementioned streaks seen in the flames at the higher pressures remain steady and appear to have their origin at the axis of symmetry, extending in the radial direction. Their appearance becomes increasingly pronounced with increasing pressure. The repeatability of the experimental data on critical conditions for extinction is not influenced by the formation of these streaks, but they may further decrease the measured extinction strain rates for $p > 1.0$ MPa through locally higher strain caused by the streaks, which could explain the disagreement between experiments and computations. In order to test for this, nitrogen was replaced by helium as the diluent for both fuel and oxygen at similar conditions to lower the Reynolds number and thereby decrease possible tendencies towards instability. Experimentally, these streaks were not seen with helium, and the corresponding extinction results are shown in Fig. 10 for $X_{F,1} = 0.25$ and $X_{O_2,2} = 0.28$. Despite substantial differences in absolute values of extinction strain rates, there is good relative agreement between experiments and predictions of the USC and revised San Diego mechanisms in Fig. 10, even to the extent of a leveling tendency at high pressure. This experimental leveling in Fig. 10, not seen in Fig. 9, provides further evidence that the streaks may cause premature extinction. The disagreement for the absolute values of extinction strain rates can be possibly attributed to chaperone efficiencies. The USC mechanism has
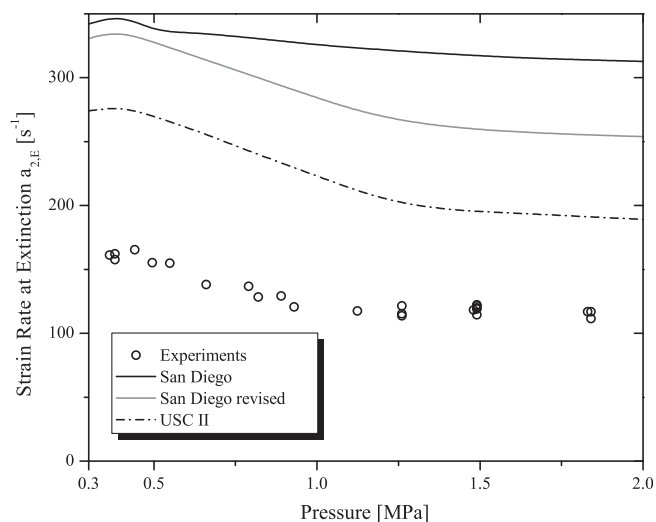
screens at the higher pressures, and then may be responsible for early flame extinction. For these reasons, it is unclear whether the experimental or computational results are more reliable at these higher pressures.

Because of the evident poor performance of the San Diego mechanism at the higher pressures, attention was focused on possible deficiencies in the chemical kinetics of that mechanism. Sensitivity studies and computations with revised rate parameters pointed to the importance of reactions involving HO_2 at elevated pressures. Study of more recent literature indicated deficiencies in rate parameters of two steps involving HO_2 in the current San Diego mechanism. One concerns the direct recombination step $O + OH + M \Leftrightarrow HO_2 + M$ for which the original rate, based on older literature, had to be lowered [22] to avoid large discrepancies with syngas data, but the lowered value still remained higher than a recent upper limit indicated by Burke et al. [23], who chose to eliminate this step entirely, on the grounds that whatever the rate is (its value currently being unknown) it cannot be rapid enough to influence results of any combustion predictions. Following Burke et al. [23], we therefore now eliminate this step entirely from San Diego mechanism.

The other reaction for which important new information is available is the step $HO_2 + OH \Leftrightarrow H_2O + O_2$, which also removes radicals and thereby contributes to lowering the extinction strain rate at higher pressures. The rate for this step in the USC mechanism is much larger than the rate in the current San Diego mechanism and is largely responsible for the good agreement of USC mechanism in Fig. 9. The rate in that mechanism was obtained by adding the contribution from a number of channels predicted by ab initio computations [24,25], but recent experiments [26] clearly show that rate is too high. The experiments, however, do demonstrate the existence of an important high-temperature channel not contained in the current San Diego description but present (with too high a rate) in the USC mechanism. That channel therefore was added to San Diego mechanism, producing the specific reaction-rate constant.

$$k = 2.89 \times 10^{13} \exp(250/T) + 4.5 \times 10^{14} \exp(-5500/T), \quad (3)$$

the last term of which is the reported [26] high-temperature term.

Finally, although producing only a minor improvement in the agreement between predictions and experiments the prefactor

Fig. 10. The strain rate at extinction, $a_{2,E}$ as a function of pressure, for a methane flame diluted with helium at fixed $X_{F,1} = 0.25$ and $X_{O_2,2} = 0.28$. Open symbols represent experimental data, while computations are represented by a solid [——] curve for San Diego mechanism with mixture-averaged diffusion and a dash-dotted [-·-·-] curve for USC-mech II, and a solid gray [——] curve for the revised San Diego mechanism.

generally larger helium efficiencies for third-body reactions than the San Diego mechanism, and the San Diego predictions can be forced to agree with experiments by increasing the efficiencies for helium in the step $H + O_2 + M \Leftrightarrow HO_2 + M$ of that mechanism from 0.7 to 4.5, although such a large value would certainly be questionable, and it might be better to attribute the difference to the transport description.

Figure 11 shows critical extinction conditions for diluted ethane flames at fixed $Y_{F,1} = 0.12$. Similar to methane, experimental data show that, with increasing pressure, the strain rate at extinction first increases, attains a maximum value between 0.5 MPa and 0.6 MPa, and then decreases. Both the San Diego and USC mechanisms are in agreement with the data in Fig. 11, within experimental error, for pressures up to 0.5 MPa. The predictions for the pressure at which the extinction strain rate pressures peak are, however, substantially higher than found experimentally, suggesting possible inaccuracies in all mechanisms or transport descriptions at the higher pressures. The differences in the predictions of different mechanisms are not very great in Fig. 11.

Figure 12 shows critical conditions of extinction for diluted ethylene flames at fixed $Y_{F,1} = 0.09$. The qualitative behavior is similar to that of ethane, with a maximum extinction strain rate attained at 0.5 MPa experimentally but at higher pressures computationally. Substantial disagreement is found for higher pressures, for all mechanisms. Unlike the situation with ethane, there are substantial differences between the predictions of the San Diego and USC mechanism for ethylene, and revisions to the San Diego mechanism have comparatively minor influences on the predictions for ethane and ethylene, which have lower flame temperatures and are influenced more strongly by C_2 chemistry. It is unclear to what extent the substantial overprediction of the extinction strain rates by the San Diego mechanism for ethylene are due to the use of mixture-averaged transport. It is interesting that for both ethane and ethylene the value of the pressure at which the extinction strain rate is predicted to peak is noticeably smaller and somewhat closer to the experiments for the San Diego mechanism than for the USC mechanism.

Figure 13 shows the strain rate at extinction, $a_{2,E}$, for methane flames as a function of the mass fraction of fuel, $Y_{F,1}$, at fixed values of pressure $p = 0.5$ MPa and $p = 1.0$ MPa. At $p = 0.5$ MPa, extinction
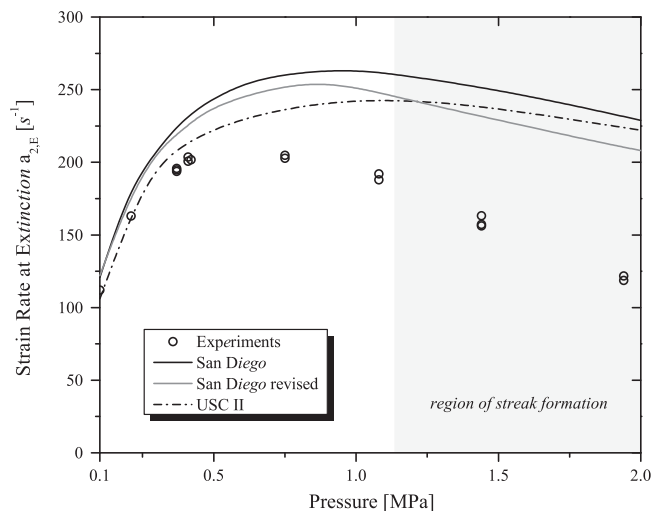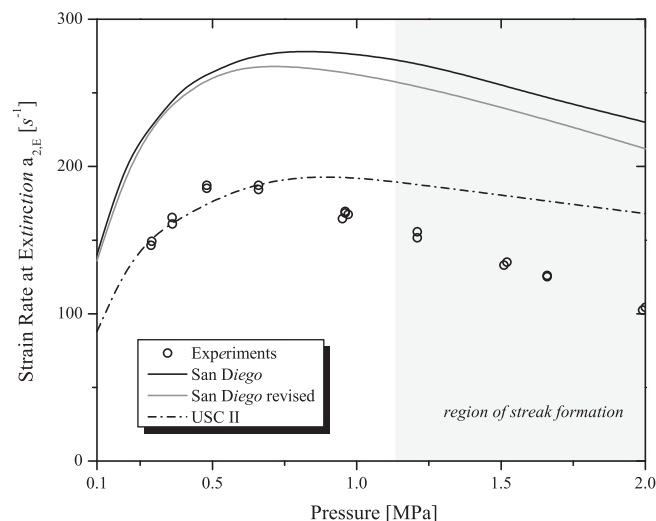

Fig. 12. Experimentally obtained strain rates at extinction, $a_{2,E}$, for ethylene diluted with nitrogen as a function of pressure, p, at fixed $Y_{F,1} = 0.09$. The oxidizer is air. Open symbols represent experimental data, while computations are represented by a solid [——] curve for San Diego mechanism with mixture-averaged diffusion and a dash-dotted [- - -] curve for USC-mech II, and a solid gray [——] curve for the revised San Diego mechanism.
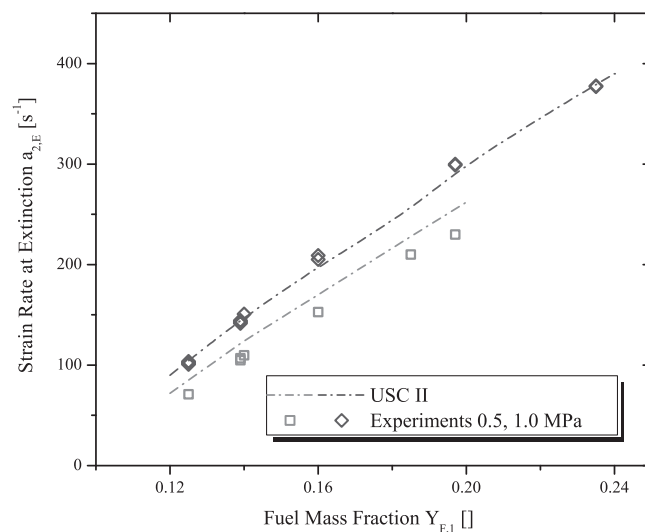

Fig. 13. The strain rate at extinction, $a_{2,E}$, for methane diluted with nitrogen as a function of the mass fraction of fuel, $Y_{F,1}$, at fixed values of pressure $p = 0.5$ MPa and $p = 1.0$ MPa. Open symbols represent experimental data, while computations are represented by dash-dotted [-·-·-·] lines for USC-mech II.

strain rates were investigated in the range $0.125 \leqslant Y_{F,1} \leqslant 0.24$, and for $p = 1.0$ MPa in the range $0.125 \leqslant Y_{F,1} \leqslant 0.2$. Experimental data exhibits the expected result that at fixed p the value of $a_{2,E}$ increases with increasing $Y_{F,1}$. The agreement between the computations of USC-mech II and experiments is excellent, consistent with the agreement in Fig. 9. All chemical–kinetic mechanisms used here correctly predict the slope of these curves of extinction strain rates as a function of fuel mass fractions.

7. Concluding remarks

The experimental study presented here showed that pressure has a substantial effect on critical extinction conditions for gaseous hydrocarbon diffusion flames. Extinction strain rates first increase in the moderately elevated pressure range until a peak value is at-

Fig. 11. Experimentally obtained strain rates at extinction, $a_{2,E}$, for ethane diluted with nitrogen as a function of pressure, p, at fixed and $Y_{F,1} = 0.12$. The oxidizer is air. Open symbols represent experimental data, while computations are represented by a solid [——] curve for San Diego mechanism with mixture-averaged diffusion and a dash-dotted [-·-·-·] curve for USC-mech II, and a solid gray [——] curve for the revised San Diego mechanism.

tained, above which a decreasing trend begins. The occurrence of streaks observed experimentally in the flames warrants further investigations concerning their possible influence on flame extinction between 1.0 MPa and 2.0 MPa. The further decrease in extinction strain rates with increasing pressure in this range when streaks are visible was not observed when nitrogen was replaced by helium in the methane flame. Experimental data obtained in the pressure range between 0.1 MPa and 1.0 MPa can be considered to be accurate since it is sufficiently far away from the onset of the formation of streaks. This accuracy is also supported by the temperature profiles measured in this range, which showed good agreement with numerical predictions and scalability when account was taken of influences of flame radiation. Chemical–kinetic mechanisms were found to perform with varying success, which is not surprising since this is the first study addressing the extinction of highly diluted counterflow diffusion flames for low-molecular weight hydrocarbon fuels at elevated pressures. Minor revisions to San Diego mechanism for hydrocarbon reactions substantially improve agreement for methane flames, but further investigations of rate parameters for steps involving carbon-containing species definitely are warranted, aimed at improving the performance of the mechanism at high pressure. Future studies need to address the problem of streak formation because there is practical interest in flames with nitrogen rather than helium as a diluent. Such studies would expand the valid pressure range for high-pressure counterflow experiments.

Acknowledgments

References

[1] U. Niemann, K. Seshadri, F. Williams, Proc. Combust. Inst. 34 (2013) 881–886.
[2] C.H. Sohn, S.H. Chung, Combust. Flame 121 (2000) 288–300.
[3] L. Figura, A. Gomez, Combust. Flame 159 (2012) 142–150.
[4] K. Maruta, K. Abe, S. Hasegawa, S. Maruyama, J. Sato, Proc. Combust. Inst. 31 (2007) 1223–1230.
[5] H. Böhm, F. Lacas, Proc. Combust. Inst. 28 (2000) 2627–2634.
[6] J. Sato, Combust. Sci. Technol. 75 (1991) 103–113.
[7] T. Niioka, S. Hasegawa, T. Tsukamoto, J. Sato, Combust. Flame 86 (1991) 171–178.
[8] T. Hiraiwa, N. Ono, T. Niioka, Symp. (Int.) Combust. 24 (1992) 239–245. Twenty-Fourth Symposium on Combustion.
[9] R.M. Fristrom, Flame Struct. Processes 118–120.
[10] K. Seshadri, F.A. Williams, Int. J. Heat Mass Transfer 21 (1978) 251–253.
[11] I.K. Puri, K. Seshadri, Combust. Sci. Technol. 53 (1987) 55–65.
[12] CHEMKIN-PRO Release 15112, Reaction Design, Inc., San Diego, CA, 2012.
[13] The San Diego Mechanism, 2011. <http://combustion.ucsd.edu>.
[14] H. Wang, X. You, A. Joshi, S. Davis, A. Laskin, F. Egolfopoulos, C. Law, 2007. <http://ignis.usc.edu/USC_Mech_II.htm>.
[15] A. Cuoci, A. Frassoldati, T. Faravelli, E. Ranzi, Proc. Combust. Inst. 32 (2008) 1335–1342.
[16] A. Cuoci, A. Frassoldati, T. Faravelli, E. Ranzi, Combust. Sci. Technol. 180 (2008) 767–784.
[17] R. Barlow, A. Karpetis, J. Frank, J.-Y. Chen, Combust. Flame 127 (2001) 2102–2118.
[18] W. Grosshandler, NIST Tech. Note 1402 (1993) 52.
[19] L. Pons, N. Darabiha, S. Candel, Combust. Flame 152 (2008) 218–229.
[20] D. Bradley, A.G. Entwistle, Brit. J. Appl. Phys. 12 (1961) 708.
[21] A. Liñán, Acta Astronaut. 1 (1974) 1007–1039.
[22] P. Saxena, F.A. Williams, Combust. Flame 145 (2006) 316–323.
[23] M.P. Burke, F.L. Dryer, Y. Ju, Proc. Combust. Inst. 33 (2011) 905–912.
[24] R. Sivaramakrishnan, A. Comandini, R. Tranter, K. Brezinsky, S. Davis, H. Wang, Proc. Combust. Inst. 31 (2007) 429–437.
[25] X. You, H. Wang, E. Goos, C.-J. Sung, S.J. Klippenstein, J. Phys. Chem. A 111 (2007) 4031–4042. PMID: 17388389.
[26] Z. Hong, K.-Y. Lam, R. Sur, S. Wang, D.F. Davidson, R.K. Hanson, Proc. Combust. Inst. 34 (2013) 565–571.

Experimental investigations of the influence of pressure on critical extinction conditions of laminar nonpremixed flames burning condensed hydrocarbon fuels, jet fuels, and surrogates

Ryan K. Gehmlich [*], Austin Kuo, Kalyanasundaram Seshadri

Department of Mechanical and Aerospace Engineering, University of California at San Diego, La Jolla, CA 92093-0411, USA

Abstract

Critical conditions of extinction are measured for high molecular weight hydrocarbon fuels, jet fuels and surrogates at pressures up to 0.4 MPa. The hydrocarbon fuels tested are n-heptane, cyclohexane, n-octane, iso-octane, and n-decane. Jet fuels tested include JP-8 and Jet-A. The surrogates tested are the Aachen surrogate, consisting of 80% n-decane and 20% 1,3,5-trimethylbenzene by mass, and the 2nd generation POSF 4658 Princeton surrogate consisting of 49.6% n-dodecane, 24.3% iso-octane, 19.8% n-propylbenzene, and 6.3% 1,3,5-trimethylbenzene by mass. The counterflow, condensed-fuel configuration is employed. Air diluted with nitrogen at 298 K is injected onto the surface of a pool of heptane. The mass fraction of oxygen in the oxidizer stream is represented by $Y_{O_2,2}$. A flame is stabilized in the stagnation point boundary layer that is established above the liquid–gas interface. At a selected value of pressure p, and at a selected value of $Y_{O_2,2}$, the flow velocity of the oxidizer stream is increased until extinction takes place. The strain rate at extinction is calculated. The experiment is repeated for a range of pressures. The general ordering of extinction strain rates of hydrocarbon fuels was observed and found to be in general agreement with the predictions of kinetic models and experiments conducted at atmospheric pressure in earlier experiments and computations. An initial linear increase of extinction strain rate with pressure is observed at pressures up to 0.175 MPa, followed by a general flattening of the curves up to 0.35 MPa. At pressures above 0.35 MPa, extinction strain rates of some fuels begin to decrease with increased pressures. These general trends are consistent with results previously measured for n-heptane, n-hexane, and n-decane flames in a similar configuration.

© 2014 The Combustion Institute. Published by Elsevier Inc. All rights reserved.

Keywords: Condensed fuel; Liquid pool; Extinction; JP-8; Surrogate

1. Introduction

Numerous experimental, computational and analytical studies have addressed combustion of

* Corresponding author.
  E-mail address: rgehmlic@ucsd.edu (R.K. Gehmlich).

various hydrocarbon fuels, hydrogen, and carbon monoxide at elevated pressures [1–11]. These studies include combustion in shock tubes and flow reactors [5–7,12,13] and counterflow nonpremixed flames [1,2,7,10,11], and have illuminated the influence of pressure on combustion. Some studies have provided critical conditions of extinction of methane and ethane flames [8–11]. There are, however, very few studies of extinction of high molecular weight hydrocarbon fuels in nonuniform flows at high pressure, with the exception of the early pioneering studies described in [1,2]. In the present work critical conditions of extinction are measured for nonpremixed combustion of various condensed hydrocarbon fuels, jet fuels, and surrogates at moderate pressure. The counterflow configuration is employed.

Two types of counterflow configurations—the vaporized fuel configuration and the condensed fuel configuration have been employed in previous studies on hydrocarbon fuels that are liquids at room temperature and pressure [14–17]. In the vaporized fuel configuration, liquid fuel is first vaporized and then introduced into the counterflow burner. In the condensed fuel configuration a gaseous oxidizing stream flows over the vaporizing surface of a liquid fuel. This configuration was employed in many previous studies at 1 atm [18–22], and at moderate pressures [1,2]. This configuration is employed in the present work. The condensed fuel configuration is particularly useful for experimental studies on those fuels that have high boiling temperatures where vaporization with negligible thermal breakdown is difficult to achieve. For *n*-decane, for example, the normal boiling point is greater than 500 K at a pressure of 5 bar. As a consequence, there is an increased risk of thermal breakdown of *n*-decane if the pressure exceeds 5 bar. Therefore the condensed fuel configuration is desirable for studies on high molecular hydrocarbon fuels at elevated pressures. Studies in the condensed fuel configuration closely resemble combustion of single fuel droplets. This is another reason for the selection of this configuration for the present study.

Niioka et al. [1] and Hiraiwa [2] measured critical conditions of extinction for *n*-heptane employing the condensed fuel configuration. In their experiments the liquid fuel was introduced into a cup. The surface of the fuel was maintained at the top of a porous plate placed on the cup to prevent liquid fuel from overflowing. Fuels tested include *n*-hexane, *n*-heptane, and *n*-decane. Air with different levels of dilution with nitrogen were considered. The strain rate at extinction was measured as a function of the pressure up to 3 MPa. A key finding of their studies is that at values of pressure close to atmospheric pressure, there is at first a linear increase in extinction strain rate with increasing pressure. At higher pressures and at high levels of dilution of air with nitrogen,

the strain rate at extinction changes very little with increasing pressure [1,2]. If the air is not diluted, the strain rate at extinction first increases and then decreases [2]. A noteworthy feature of the work of Niioka et al. [1] is that by use of rigorous activation energy asymptotic analysis, a clear relation is made between the extinction strain rate measured in the condensed fuel configuration and extinction diameter of burning droplets, thus establishing the practical relevance of their studies. In the present study, critical conditions of extinction are measured for *n*-heptane, *n*-octane, iso-octane, *n*-decane, and cyclohexane.

The present study will also include measurements of critical conditions of extinction for jet fuels and surrogates of jet fuels. The motivation for this arises from a need to model combustion of practical fuels at high pressures. Commercial fuels, including jet fuels, kerosene, gasoline, and diesel, are composed of hundreds of aliphatic and aromatic hydrocarbon compounds. The major components of real jet fuels are straight-chain alkanes, branched-chain alkanes, cycloalkanes, aromatics, and alkenes [3,23–26]. On average, the composition by volume is approximately 60% alkanes, 20% cycloalkanes, 18% aromatics, and 2% alkenes [26]. Efforts to develop chemical-kinetic models that accurately describe the combustion of these practical fuels are critical to the development and the advancement of next-generation engines and power plants. However, due to the hundreds of chemical species found in practical fuels and the significant variation in the chemical composition between batches of fuel, the task of quantitatively studying and modeling them is both numerically and experimentally challenging. For this reason, studies on the combustion of jet fuels are often carried out using surrogates. Surrogate mixtures have only a handful of components, but are designed to simulate the most essential characteristics of real fuels. The fuels tested in the present work have been identified as possible components of surrogates [3,27,23,28].

The surrogates to be tested in the present work are the Aachen surrogate made up of *n*-decane (80 %) and trimethylbenzene (20 %) by weight, and the 2nd generation POSF 4658 surrogate developed by Dooley, et al. [29]. In a previous study [17], several batches of JP-8 and Jet-A, and fifteen possible surrogates of jet fuels were tested in nonpremixed systems at pressure of 1 atm. In this study [17] and other studies at 1 atm [14,15,30] the Aachen surrogate and a surrogate made up of *n*-dodecane (57 %), methylcyclohexane (21 %), and *o*-xylene (22 %), by weight, called Surrogate C were found to reproduce key aspects of nonpremixed [14,15,17] and premixed [30] combustion of JP-8. The Aachen Surrogate was found to be the best in reproducing critical conditions of autoignition of jet fuels, but not necessarily extinction, where a slightly

modified version of the Utah surrogate developed by Violi et al. [17,24] was a better match for JP-8. In these previous studies the 2nd generation POSF 4658 surrogate developed by Dooley et al. [29] was not yet available and therefore it was not tested.

2. Experimental approach and procedure

2.1. Setup

The experiments involved the use of the condensed fuel counterflow configuration in the UC San Diego High Pressure Combustion Experimental Facility (HPCEF). In this configuration, a steady axisymmetric, laminar, stagnation-point flow of an oxidizer is directed onto the vaporizing surface of a liquid fuel. This configuration allows for the experimental testing of fuels with high boiling points for which it is difficult to avoid pyrolysis reactions during fuel vaporization [22]. Figure 1 shows a schematic illustration of the basic configuration used. The reactive flow field is characterized by the value of pressure, p, the distance between the oxidizer duct exit plane and the liquid pool surface, L, the mass fraction of oxygen in the oxidizer stream, $Y_{O_2,2}$, the temperature of the oxidizer stream, T_2, and the velocity of the oxidizer stream at the exit plane, V_2. The oxidizer stream consists of a mixture of oxygen and nitrogen, which in this experiment was held fixed such that $Y_{O_2,2} = 0.175$. The radial component of the flow velocity at the oxidizer boundary is presumed to be equal to zero.

Figure 2 shows a schematic of the overall experimental setup. The counterflow burner is placed inside a stainless steel chamber designed for carrying out experiments at pressures up to 2.5 MPa. The chamber has optical access via four view-ports with fused silica windows. The pressure in the chamber is maintained constant during

experiments using a TESCOM PID-control pressure regulation system. This system is independently monitored and recorded with digital pressure transducers with an accuracy of ± 0.0007 MPa.

A semi-automatic ignition system was developed to consistently establish a stable flame in the reaction zone of the condensed fuel counterflow burner. The ignition system employed here includes two surface ignitors mounted on a mechanical arm which can be rotated into the reaction zone using a stepper motor. Gaseous flows of oxidizer and inert gases are supplied via gas bottles and controlled using mass flow controllers carefully selected and calibrated for the range of flows experienced in a given experiment. Fine screens are placed at the exit of the oxidizer duct to achieve plug flow conditions to a high degree of accuracy. A "curtain" of nitrogen flows annularly to the oxidizer duct at a flow velocity close to the duct exit velocity. A similar curtain of nitrogen flows annularly to the fuel duct at velocities close to the vaporized fuel velocity at the liquid/gas interface. These curtains serve to help shape and contain the flame as well as stabilize it. Product gases are cooled using fine water sprays within the burner body, then separated from the cooling water in a separation chamber, and finally expelled from the chamber to the building exhaust.

Fuel is supplied to the fuel cup by a syringe pump with a flow accuracy of ± 0.01 mL/min. The fuel enters the cup through a pipe which has a small hole at the top for a thermocouple probe through which a small amount of fuel can pass as well, and 4 small openings around the top of the pipe which direct fuel outward within the cup. A stainless steel screen is placed just above the thermocouple and outlet of the pipe to facilitate mixing in the pool and quell any radial temperature gradients or velocity gradients in the liquid. The lower part of the fuel cup is cooled by a water, such that fuel always enters the cup at a consistent temperature, close to 300 K. The pool temperature is measured by a thermocouple located at the point where the fuel enters the fuel cup. The cooling system maintains a consistent, steady state temperature gradient within the cup and prevents violent surface boiling for a wide range of condensed fuels, ensuring a smooth, consistent, and steady flame throughout the range of pressures used in the study.

A real time high definition camera system monitors the pool and provides visual feedback of the liquid–gas interface level, which can be compared to the desired level, as designated by a reference needle of fixed height in the cup. Use of a reference needle in the cup allows for precise monitoring and control of the level through visual means. The needle tip induces a small dimple in the surface of the pool when the height is correct.
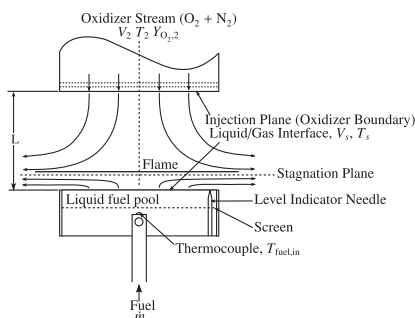

Fig. 1. Schematic illustration of the counterflow configuration. V_2 and V_s are the velocities at the oxidizer-boundary and on the gas side of the liquid–gas interface, respectively. T_2 and T_s are the temperatures at the oxidizer-boundary and the liquid–gas interface, respectively.
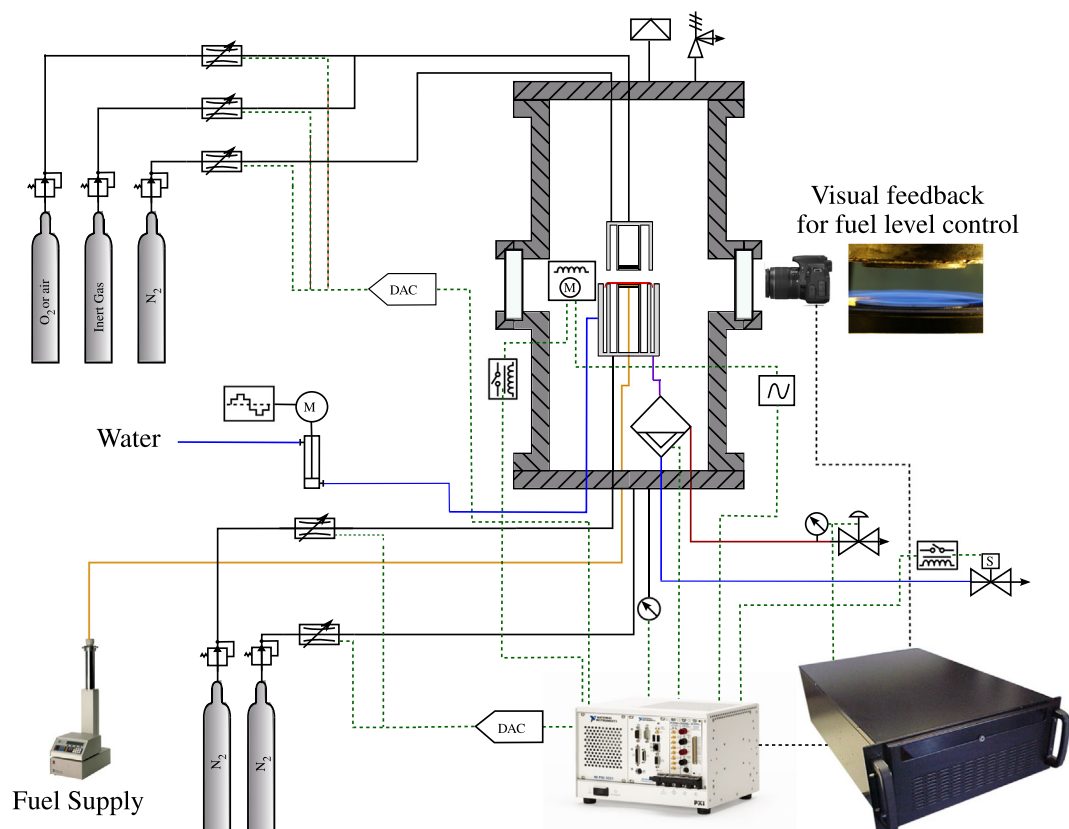
Fig. 2. Schematic illustration of the experimental arrangement. The figure shows the counterflow burner placed inside the pressure chamber. The figure also shows the gas supply system, the mass flow controllers, the mass flow controller (MFC) command modules, and the data acquisition and control system (DAC).

If the dimple disappears, the level is too high; if the dimple becomes larger or the needle tip becomes visible, the level is too low. Adjustments to the fuel feed rate can be made via a remote control station to maintain a constant level. Estimated errors in the separation distance, L, are less than ± 0.2 mm. This method also allows for measurements of fuel mass burning rates by recording the required fuel feed rate to maintain the fuel cup level under steady state burning conditions.

Any fuel spillage or overflow drains down into a channel where it can periodically be purged from the pressure chamber during the experiment.

2.2. Procedures

The value of the strain rate, defined as the normal gradient of the normal component of the flow velocity, changes from the fuel boundary to the oxidizer boundary [31]. The characteristic strain rate on the oxidizer side of the stagnation plane, a_2, is defined by Eq. (1):

$$a_2 = \frac{2V_2}{L} \tag{1}$$

Equation (1) has been obtained from an asymptotic theory where the Reynolds numbers of the laminar flow at the duct exit is presumed to be large [21,31], but irrespective of that, it serves to parameterize the experimental conditions for future comparisons with numerical computations. The separation distance, L, in this experiment was 10 mm.

Critical extinction conditions are measured by selecting a fixed pressure and establishing a flow of oxidizer at a fixed oxygen mass fraction onto the liquid pool surface. This flow is initialized at an oxidizer strain rate well below the critical extinction value. A pair of silicon nitride heating elements is then brought into the flow field using a remotely controlled stepper motor system and is energized to ignite a stable flame. The heating elements are then retracted from the flow field. The flow of oxidizer is incrementally increased while simultaneously increasing the feed rate of

Table 1
Tested surrogate mixtures for jet fuels (mass %).

	Surrogate compounds	A [15]	B [29]
Normal alkanes	n-Decane	80	
	n-Dodecane		49.6
Branched alkanes	iso-Octane		24.3
Aromatics	n-Propylbenzene		19.8
	1,3,5-Trimethylbenzene	20	6.3

fuel to the cup in order to maintain a constant and desired fluid level in the cup. This process is done slowly to ensure that steady state conditions are reached at each incremental increase of strain rate. The procedure is continued until the flame extinguishes.

2.3. Fuels tested

A wide range of liquid fuels were tested, namely cyclohexane (C_6H_{12}), n-heptane (n-C_7H_{16}), n-octane (n-C_8H_{18}), iso-octane (C_8H_{18}), n-decane (n-$C_{10}H_{22}$), JP-8, Jet-A, and two JP-8 surrogate mixtures, namely a 2 component mixture (referred to as A) and a 4 component mixture (referred to as B). The details of the surrogate compositions used in this experiment are listed in Table 1. The JP-8 tested was a military-grade jet fuel, POSF-6169 supplied by Edwards Air Force Base. The Jet-A tested was POSF-4658 commercial aviation fuel from Montgomery Field Airport in San Diego, California.

3. Results and discussion

3.1. Extinction

Figure 3 shows the extinction strain rate as a function of pressure for a fixed oxygen mass
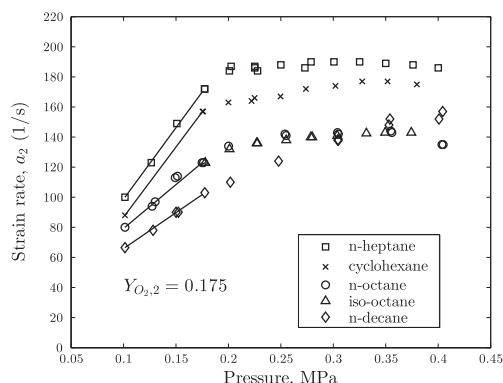

Fig. 3. The characteristic strain rate at extinction, a_2, as a function of pressure for a number of component reference fuels at a fixed oxidizer mass fraction of $Y_{O_2,2}$.

fraction of $Y_{O_2,2} = 0.175$ for 5 different reference fuels. In the condensed fuel configuration, dilution of the oxidizer stream is necessary to reduce soot formation and improve the accuracy of the measurements. The particular value of $Y_{O_2,2} = 0.175$ is selected because it permits experimental data for a wide range of strain rates and pressures for which the flame is stable and measurable for the fuels tested in the experiment. The ordering of extinction strain rates at elevated pressures is consistent with earlier results of Grana et al. [22] for extinction strain rates measured and computed at atmospheric pressures. The highest extinction strain rates were observed for n-heptane, followed by cyclohexane, n-octane and iso-octane, with n-decane having the lowest extinction strain rates. The tendency for all reference fuels is to have a steep linear increase in the extinction strain rates up until approximately 0.175 MPa, followed by a leveling off for the pressure ranges from 0.175 to 0.4 MPa, and then a dropping off of extinction strain rate as pressure is increased from that point. A similar phenomenon was measured and reported for n-heptane flame extinction by Hiraiwa [2]. Previous work by Niemann et al. with gaseous methane counter flow diffusion flames in a similar configuration [8] describe this non-monotonicity as the possible result of increasing bimolecular branching rates at the lower pressures followed by increased third-body termination rates at higher pressures. These results were also predicted for gaseous methane flames in numerical computations using both the USC mechanism [32] and a revised San Diego mechanism [8].

Alkanes with extremely low vapor pressures and high boiling temperatures (such as n-dodecane) proved to have inconclusive results. This was due to higher liquid surface temperatures and the onset of violent surface boiling while burning, despite water cooling the fuel in the cup to help prevent boiling. Aromatic reference fuels tested including trimethylbenzene, proved to have inconclusive extinction results due to the tendency toward producing large amounts of soot for all ranges of oxidizer mass fractions and pressures for which a flame could be established.

Figure 4 shows the measured extinction strain rates as a function of pressure for two jet fuels, POSF 4658 Jet-A and POSF 6169 JP8, along with the Aachen surrogate (surrogate A) and the 2nd generation POSF 4658 Princeton surrogate (B). Once again the oxygen mass fraction is fixed at $Y_{O_2,2} = 0.175$. This figure shows a significant disagreement for the Aachen surrogate at elevated pressures, but relatively close agreement between the Princeton surrogate and the two jet fuels, with small deviations appearing at pressures above 0.3 MPa. For the Aachen surrogate, rather than closely following the extinction curve of the jet fuels as was observed at atmospheric pressure [22], it followed with little deviation the curve
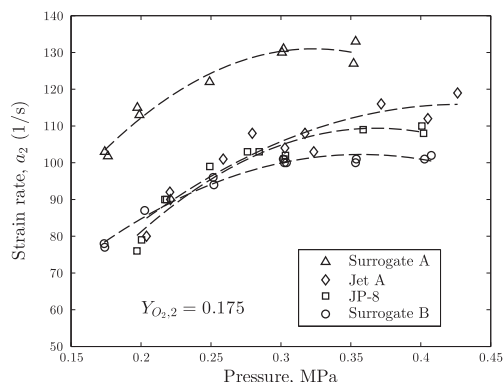
Fig. 4. The characteristic strain rate at extinction, a_2, as a function of pressure for jet fuels and two surrogate mixtures at a fixed oxidizer mass fraction of $Y_{O_2,2} = 0.175$.
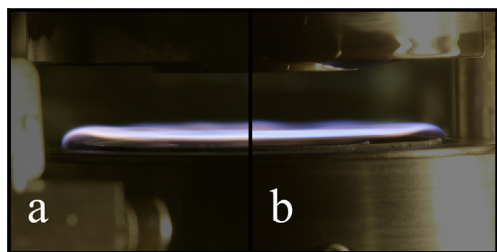

Fig. 6. The mass burning rate, $\dot{m}''$, as a function of strain rate for n-heptane, iso-octane, and cyclohexane at a fixed oxidizer mass fraction of $Y_{O_2,2} = 0.175$. The dashed lines represent extinction limits.

Fig. 5. Photograph of surrogate B (2nd generation POSF 4658 Princeton surrogate) side by side with a photograph of JP-8. The flame is stabilized in the high pressure experimental facility shown in Fig. 2 for $p = 0.25$ MPa, $Y_{O_2,2} = 0.175, T_2 = 298$ K, and $a_2 = 80$ s^{-1}.

Fig. 7. The flame standoff distance for several reference fuels as a function of pressure for $a_2 = 100, Y_{O_2,2} = 0.175$, and $T_2 = 298$ K.

measured for n-decane at elevated pressures, which had significantly higher extinction strain rates than the jet fuels.

Figure 5 shows a photograph of surrogate B (2nd generation POSF 4658 Princeton surrogate) side by side with a photograph of JP-8. The conditions for these photographs are $p = 0.25$ MPa, $Y_{O_2,2} = 0.175, T_2 = 298$ K, and $a_2 = 80$ s^{-1}. The two flames are almost indistinguishable by sight.

3.2. Mass burning rate

Figure 6 shows the mass burning rate as a function of strain rate and pressure for n-heptane, iso-octane, and cyclohexane, showing for all fuels a linear increase in the mass burning rate with an increase in oxidizer stream duct velocity. As the mass flux of oxidizer is increased, the mass flux of fuel must be increased proportionally in order to maintain stoichiometric proportions in the reaction zone.

Figure 6 also shows an increase in mass burning rate as pressure is increased. With an increase in pressure, there is an increase in the
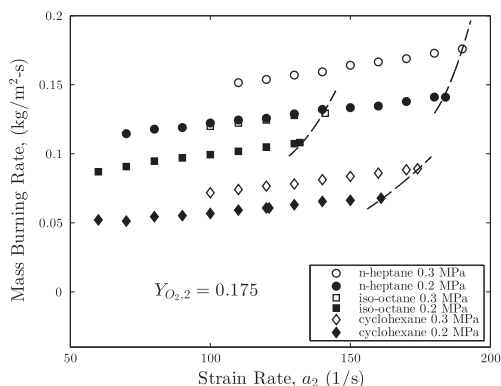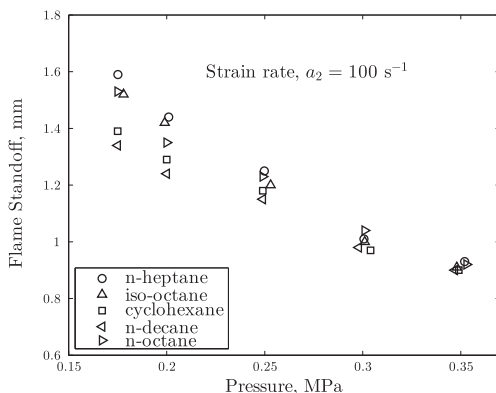
corresponding concentration of reactants in the reaction zone, driving higher reaction rates and thus higher mass burning rates. The reaction zone is also thinned, and pushed closer to the fuel surface. Similar results were obtained for other fuels and conditions.

3.3. Flame standoff distance

The flame standoff distances are measured as the distance from the liquid fuel surface to the "top" of the luminous flame. Figure 7 shows a plot of flame standoff distances vs pressure for all the component reference fuels used in the study, at a single strain rate of $a_2 = 100$ s^{-1}. In general, the standoff distances do not vary widely between fuels, but are a stronger function of strain rate and pressure. As pressure is increased, standoff distances are decreased almost linearly in the range of pressures tested.

4. Concluding remarks

The condensed fuel counterflow configuration provides insight into combustion characteristics of condensed hydrocarbon fuels at elevated pressure regimes, and offers a platform to launch future moderate pressure experiments. The ordering of component reference fuels was observed and found to be in general agreement with the predictions of kinetic models and experiments conducted at atmospheric pressure by Grana et al. Additionally, the component reference fuel's performance paralleled the trends established in similar elevated pressure experiments conducted by Niioka and Hiraiwa et al. [1,2].

With the same experimental setup, the viability of select surrogates was investigated by comparing their extinction curves to that of JP-8 and Jet-A, the target fuels to be emulated. Surrogate B's extinction curve closely resembled that of JP-8 at moderate pressures. The observation may be attributed to its 4-component composition, which provided a greater diversity in molecular structure and allowed for the formation of a variety of intermediate species that more closely mimicked those produced by the combustion of actual jet fuel.

Future investigations will compare the experimental data obtained from the elevated pressure, liquid pool setup to numerical data obtained from computer simulations employing chemical-kinetic mechanisms.

Acknowledgements

References

[1] T. Niioka, S. Hasegawa, T. Tsukamoto, *Combust. Flame* 86 (1991) 171–178.
[2] T. Hiraiwa, N. Ono, T. Niioka, *Proc. Combust. Inst.* 24 (1992) 239–245.
[3] A. Agosta, N. Cernansky, D. Miller, T. Faravelli, E. Ranzi, *Exp. Therm. Fluid Sci.* 28 (7) (2004) 701–708.
[4] L. Figura, A. Gomez, *Combust. Flame* 159 (1) (2012) 142–150.
[5] S. Jahangirian, S. Dooley, F. Haas, F. Dryer, *Combust. Flame* 159 (1) (2012) 30–43.
[6] H.J. Curran, W.J. Pitz, C.K. Westbrook, C.V. Callahan, F.L. Dryer, *Proc. Combust. Inst.* 27 (1998) 379–387.
[7] R. Sivaramakrishnan, A. Comandini, R. Tranter, et al., *Proc. Combust. Inst.* 31 (2007) 429–437.
[8] U. Niemann, K. Seshadri, F. Williams, *Combust. Flame* 161 (1) (2013) 138–146.
[9] J. Sato, *Combust. Sci. Technol.* 75 (1991) 103–113.
[10] K. Maruta, K. Abe, S. Hasegawa, et al., *Proc. Combust. Inst.* 31 (2007) 1223–1230.
[11] H. Böhm, F. Lacas, *Proc. Combust. Inst.* 28 (2000) 2627–2634.
[12] P. Dagaut, M. Reuillon, J. Boettner, M. Cathonnet, *Symp. (Int'l) Combust.* 25 (1) (1994) 919–926.
[13] U.C. Müller, N. Peters, A. Linan, *Proc. Combust. Inst.* 24 (1992) 777–784.
[14] S. Humer, A. Frassoldati, S. Granata, T. Faravelli, E. Ranzi, R. Seiser, K. Seshadri, *Proc. Combust. Inst.* 31 (1) (2007) 393–400.
[15] S. Honnet, K. Seshadri, U. Niemann, N. Peters, *Proc. Combust. Inst.* 32 (1) (2009) 485–492.
[16] R. Seiser, U. Niemann, K. Seshadri, *Proc. Combust. Inst.* 33 (2011) 1045–1052.
[17] S. Humer, R. Seiser, K. Seshadri, *J. Propul. Power* 27 (4) (2011) 847–855.
[18] A. Hamins, K. Seshadri, *Combust. Sci. Technol.* 38 (1984) 89–103.
[19] A. Hamins, K. Seshadri, *Symp. (Int'l) Combust.* 20 (1984) 1905–1913.
[20] A. Hamins, K. Seshadri, *Combust. Flame* 68 (3) (1987) 295–307.
[21] K. Seshadri, S. Humer, R. Seiser, *Combust. Theory Modell.* 12 (5) (2008) 831–855.
[22] R. Grana, K. Seshadri, A. Cuoci, U. Niemann, T. Faravelli, E. Ranzi, *Combust. Flame* 159 (1) (2012) 130–141.
[23] T. Edwards, *J. Propul. Power* 17 (2) (2001) 461–466.
[24] A. Violi, S. Yan, E.G. Eddings, A.F. Sarofim, S. Granata, T. Faravelli, E. Ranzi, *Combust. Sci. Technol.* 174 (11-12) (2002) 399–417.
[25] J. Muylaert, Technologies for Propelled Hypersonic Flight, vol. 2, Nat.l Tech. Inf. Serv., Springfield, VA, 2006.
[26] M. Colket, T. Edwards, S. Williams, et al., in: AIAA Aerospace Sciences Meeting and Exhibit, AIAA, Reno, NV, 2007, pp. 1–21.
[27] Jet fuel surrogate research: A white paper, Surrogate Fuels Workshop-Part IV, 2006.
[28] T. Edwards, "Real" kerosene aviation and rocket fuels: Compositions and surrogates, 2001 Fall Technical Meeting, Eastern States Section of the Combustion Institute.
[29] S. Dooley, S. Won, J. Heyne, et al., *Combust. Flame* 159 (4) (2012) 1444–1466.
[30] K. Seshadri, A. Frassoldati, A. Cuoci, T. Faravelli, U. Niemann, P. Weydert, E. Ranzi, *Combust. Theory Model.* 15 (2011) 569–583.
[31] K. Seshadri, *Combust. Flame* 33 (1978) 197–215. , 2007.
[32] H. Wang, X. You, A.V. Joshi, S.G. Davis, A. Laskin, F. Egolfopoulos, C.K. Law, USC Mech Version II. High-Temperature combustion reaction model of H2/CO/C1-C4 compounds, 2007. <http://ignis.usc.edu/USC_Mech_II.htm>.

Rate-Ratio Asymptotic Analysis of the Influence of Addition of Hydrogen on the Structure and Mechanisms of Extinction of Nonpremixed Methane Flames

Kalyanasundaram Seshadri[a] & Xue-Song Bai[b]

[a] Department of Mechanical and Aerospace Engineering, University of California at San Diego, La Jolla, California, USA

[b] Department of Energy Sciences, Lund University, Lund, Sweden
Published online: 10 Dec 2015.

Click for updates

PLEASE SCROLL DOWN FOR ARTICLE

Taylor & Francis
Taylor & Francis Group

RATE-RATIO ASYMPTOTIC ANALYSIS OF THE INFLUENCE OF ADDITION OF HYDROGEN ON THE STRUCTURE AND MECHANISMS OF EXTINCTION OF NONPREMIXED METHANE FLAMES

Kalyanasundaram Seshadri[1] and Xue-Song Bai[2]

[1]*Department of Mechanical and Aerospace Engineering, University of California at San Diego, La Jolla, California, USA*
[2]*Department of Energy Sciences, Lund University, Lund, Sweden*

Rate-ratio asymptotic analysis is carried out to elucidate the influence of hydrogen on the structure and critical conditions for extinction of nonpremixed methane flames. Steady, axisymmetric, laminar flow of two counterflowing streams toward a stagnation plane is considered. One stream, called the fuel stream is made up of a mixture of methane (CH_4) and nitrogen (N_2). The other stream, called the oxidizer stream, is a mixture of oxygen (O_2), and N_2. Hydrogen (H_2) is added either to the oxidizer stream or to the fuel stream. A reduced mechanism of four global steps is employed in the analysis. Chemical reactions are presumed to take place in a thin reaction zone that is established in the vicinity of the stagnation plane. On either side of this thin reaction zone, the flow field is inert. These inert regions represent the outer structure of the flame. The reactants, CH_4, O_2, and H_2 are completely consumed at the reaction zone. The outer structure is constructed employing a previously developed Burke-Schumann (flame-sheet) formulation. It provides matching conditions required for predicting the structure of the reaction zone. In the reaction zone, chemical reactions are presumed to take place in two layers—the inner layer and the oxidation layer. In the inner layer fuel (methane) is consumed and the intermediate species hydrogen and carbon monoxide are formed. These intermediate species and added hydrogen are oxidized in the oxidation layer to water vapor and carbon dioxide. Critical conditions of extinction were predicted from results of the asymptotic analysis and found to agree well with previous measurements. Addition of hydrogen to methane flames promotes combustion by delaying extinction. An important finding of the asymptotic analysis is that the mechanisms by which hydrogen promotes combustion when it is added to the oxidizer stream is different from that when it is added to the fuel stream.

Keywords: Extinction; Hydrogen enrichment; Methane/air non-premixed flame; Rate-ratio asymptotic analysis; Scalar dissipation rate

INTRODUCTION

Recently, Niemann et al. (2013) carried out an experimental and computational study to elucidate the influence of hydrogen (H_2) on the structure and critical conditions of extinction of laminar nonpremixed methane (CH_4) flames. In their study, H_2 was added to either the fuel stream made up of methane and nitrogen (N_2) or to the oxidizer stream made up of oxygen (O_2) and nitrogen with both streams at normal atmospheric pressure, and at normal room temperature. Experimental conditions were adjusted to fix selected values of the stoichiometric mixture fraction and adiabatic temperature. At these selected conditions, the strain rate at extinction was measured as a function of the hydrogen concentration in the fuel stream or in the oxidizer stream (Niemann et al., 2013). The ratio of the fraction of the flux of oxygen that consumes hydrogen to the fraction that consumes fuel (methane) was calculated. This ratio is denoted by r. It was found that, within experimental uncertainty, the ratio of the extinction strain rate with H_2 addition to that without was the same at any given value of r, irrespective of whether the hydrogen was added to the fuel stream or to the oxidizer stream. This experimental result was also in close agreement with computational predictions employing detailed chemistry. The present rate-ratio asymptotic analysis is motivated by these previous findings. It seeks to obtain an improved fundamental understanding of the influence of hydrogen on nonpremixed methane flames. In particular, the present analysis seeks to elucidate the similarities and differences in flame structures and mechanisms of extinction between hydrogen addition to the fuel stream and hydrogen addition to the oxidizer stream.

A number of rate-ratio asymptotic analyses of the structure of nonpremixed methane flames are available (Bai and Seshadri, 1999; Chelliah and Williams, 1990; Chelliah et al., 1991; Seshadri, 1996; Seshadri and Ilincic, 1995b; Seshadri and Peters, 1988; Seshadri and Williams, 1994; Treviño and Williams, 1988; Yang and Seshadri, 1992). In these analyses, the combustion of methane was represented by a reduced chemical-kinetic mechanism made up of four global steps. Critical conditions of extinction were predicted and compared with experimental data and predictions using detailed chemistry. The analysis of Seshadri and Peters (1988) and Yang and Seshadri (1992) introduced the approximation that the reactants, CH_4 and O_2, are completely consumed in the reaction zone to the leading order. Subsequently it was found that this approximation failed to predict chemical inhibition of methane flames. To improve predictions of chemical inhibition, Seshadri and Ilincic (1995b) first carried out a rate-ratio asymptotic asymptotic analysis with the approximation that CH_4 is completely consumed in the reaction zone but not O_2. Thus the mass fraction of O_2 is of order unity in the reaction zone, leading to its leakage. The flame structure is similar to the structure of a nonpremixed flame in the "premixed flame regime" analyzed by Liñán (1974), employing one-step chemistry with large activation energy. In the analysis of Liñán (1974), for small values of the stoichiometric mixture fraction, there was leakage of fuel to the leading order, while in rate-ratio asymptotic analysis of Seshadri and Ilincic (1995b) there was leakage of oxygen. Seshadri and Ilincic (1995a) successfully employed the formulation of Seshadri and Ilincic (1995b) to predict chemical inhibition of methane flames

by bromotrifluoromethane (CF_3Br), although significant deficiencies remained. Subsequent analysis of Grudno and Seshadri (1998) and Seshadri (2005) removed these deficiencies and provided a thorough description of chemical inhibition of methane flames by CF_3Br. Bai and Seshadri (1999) made significant improvements to the analysis of Seshadri and Ilincic (1995b) and included the influences of a number of key elementary reactions that were previously neglected. The analysis of Bai and Seshadri (1999) introduced the approximation that there is a leakage of oxygen from the reaction zone to the leading order. This improved analysis was successfully used by Seshadri and Bai (2007) to predict the extinction of partially premixed methane flames. Recently Seshadri et al. (2014) extended the formulation of Bai and Seshadri (1999) to successfully predict inhibition of methane flames by nitrous oxide (N_2O).

Motivated by the success in the predictions of critical conditions of extinction of methane flames, and flame inhibition by CF_3Br and N_2O, Seshadri et al. (2013) extended the analysis of Bai and Seshadri (1999) to describe the influence of added hydrogen on the structure and critical conditions of extinction of methane flames. The analysis, however, did not provide a satisfactory description of the influence of hydrogen on methane flames. Addition of hydrogen to methane flames promotes combustion (Niemann et al., 2013). It also enhances the rates of consumption of oxygen. Thus the approximation that, to the leading order, there is complete consumption of oxygen at the reaction zone is expected to be more accurate. The failure of the analysis of Seshadri et al., (2013) is attributed to inaccuracies in the approximation that oxygen is of order unity in the reaction zone. The present analysis introduces the approximation that both CH_4 and O_2 are completely consumed in the reaction zone. It extends the formulation of Seshadri and Peters (1988) and Yang and Seshadri (1992) to include the influences of hydrogen addition to the reactant streams. It also includes all the improvements of Bai and Seshadri (1999).

FLAME STRUCTURE

Steady, axisymmetric, laminar flow of two counterflowing streams toward a stagnation plane is considered here. The origin is placed at the stagnation plane; the spatial coordinate normal to the stagnation plane is x, and the normal component of the flow velocity is represented by u. The stream carrying CH_4 mixed with N_2 is called the fuel stream, which is presumed to flow toward the stagnation plane from the region $x < 0$. The stream carrying O_2 and N_2 is called the oxidizer stream. It flows toward the stagnation plane from the region $x > 0$. Hydrogen is added to the reactant streams. The mass fraction of CH_4 in the fuel stream is $Y_{F,1}$, and that of O_2 in the oxidizer stream is $Y_{O_2,2}$. The mass fraction of H_2 added to the fuel stream is $Y_{H_2,1}$, and that added to the oxidizer stream is $Y_{H_2,2}$; the temperature of the fuel stream is T_1, and that of the oxidizer stream is T_2.

In view of the high diffusivity of hydrogen in comparison to the other reactants, following the previous analysis of Seshadri and Trevino (1989) and Niemann et al. (2013), it is convenient to introduce the conserved scalar quantities ξ and ξ_{H_2} defined by the equations

$$\rho u \frac{d\xi}{dx} - \frac{d}{dx}\left(\frac{\lambda}{c_p}\frac{d\xi}{dx}\right) = 0,$$

$$\rho u \frac{d\xi_{H_2}}{dx} - \frac{d}{dx}\left(\frac{\lambda}{c_p Le_{H_2}}\frac{d\xi_{H_2}}{dx}\right) = 0. \tag{1}$$

Here λ is the thermal conductivity, c_p is the heat capacity of the mixture, ρ is the density, λ is the coefficient of thermal conductivity, $Le_i = \lambda / (\rho c_p D_i)$ is the Lewis number of species i, and D_i is the coefficient of diffusion of species i. The heat capacity, c_p, is presumed to be constant. Both ξ and ξ_{H_2} are defined to be unity in the fuel stream far from the stagnation plane, and zero in the oxidizer stream far from the stagnation plane. A characteristic diffusion time χ^{-1} deduced from the spatial gradient of ξ is

$$\chi = 2\left[\lambda / (\rho c_p)\right] \ |\nabla\xi|^2. \tag{2}$$

The quantity χ represents the scalar dissipation rate and plays a central role in the analysis. The goal of the present analysis is to predict the scalar dissipation rate at extinction. For convenience, the definitions

$$X_i \equiv Y_i W_{N_2} / W_i,$$
$$\tau \equiv c_p W_{N_2} (T - T_u) / Q_F, \tag{3}$$

are introduced. Here, Q_F is the heat released per mole of CH_4 consumed in the overall step $CH_4 + 2\,O_2 \rightarrow CO_2 + 2H_2O$, W_i is the molecular weight of species i, W_{N_2} is the molecular weight of nitrogen, and $T_u = T_2 + (T_1 - T_2)\,\xi$. It follows that $X_i = C_i W_{N_2} / \rho$, where C_i is the molar concentration of species i. At 298 K, $Q_F = 803000$ J/mol.

Chemical reactions are presumed to take place in a thin reaction-zone that is located at $x = x_{st}$. The values of ξ and ξ_{H_2} at x_{st} are, respectively, their stoichiometric values ξ_{st} and $\xi_{H_2,st}$. The regions $x < x_{st}$ and $x > x_{st}$ are inert and represent the outer structure. The outer structure is analyzed first. It provides boundary conditions for the differential equations that describe the structure of the reaction zone.

THE OUTER STRUCTURE

The profile of temperature and profiles of mass fractions of the reactive species CH_4, O_2, added H_2, CO_2, and H_2O represent the outer structure of the flame. Figure 1 is a schematic illustration of the outer structure. At the reaction zone, $x = x_{st}$, $\xi = \xi_{st}$, and $\xi_{H_2} = \xi_{H_2,st}$; the mass fractions of CH_4, O_2, and H_2 are zero. In the region $x < x_{st}$, $\xi > \xi_{st}$, and $\xi_{H_2} > \xi_{H_2,st}$ there is no oxygen, and in the region $x > x_{st}$, $\xi < \xi_{st}$, and $\xi_{H_2} < \xi_{H_2,st}$ there is no fuel. In the analysis of the outer structure, the approximation Le_i as unity for all species, except H_2, is introduced. The value of the Lewis number of H_2, Le_{H_2}, is presumed to be constant. As a consequence of these approximations, X_i for all species, except that of H_2, is a linear function of ξ, while X_{H_2} is a linear function of ξ_{H_2} (Niemann et al., 2013; Seshadri & Trevino, 1989). At $\xi = \xi_{st}$, $X_{CO_2} = X_{CO_2,st}$ and $X_{H_2O} = X_{H_2O,st}$. For constant c_p, the profile of temperature T is also a linear function of ξ. The value of T at $\xi = \xi_{st}$ is the adiabatic temperature, T_{st}, and $\tau_{st} = c_p W_{N_2} (T_{st} - T_u) / Q_F$.

The gradient of of τ with respect to ξ, and those of X_i, are discontinuous at the reaction zone, $\xi = \xi_{st}$. These gradients in the region $\xi > \xi_{st}$ are represented by the subscript $+$, and in the region $\xi < \xi_{st}$ by the subscript $-$. The gradients at ξ_{st+} are
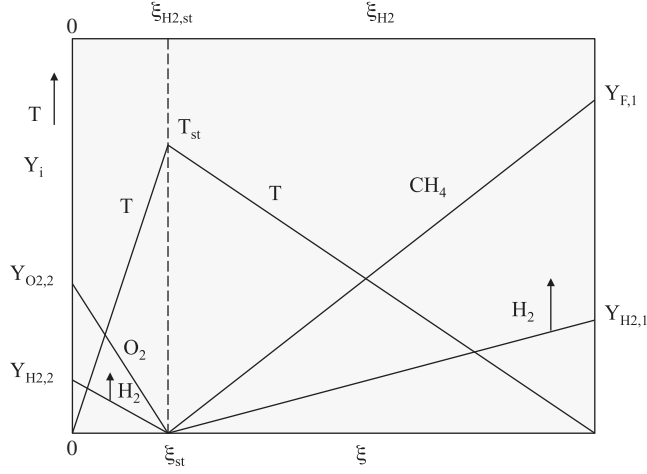
Figure 1 Schematic of the outer structure of nonpremixed methane flame with hydrogen addition to the fuel stream and to the oxidizer stream.

$$\left(dX_\mathrm{F}/d\xi\right)_+ = X_{\mathrm{F},1}\Big/(1-\xi_\mathrm{st}) = g, \quad \left(dX_{\mathrm{O}_2}/d\xi\right)_+ = 0,$$

$$\left(dX_{\mathrm{H}_2}/d\xi\right)_+ = \left[X_{\mathrm{H}_2,1}\Big/\left(1-\xi_{\mathrm{H}_2,\mathrm{st}}\right)\right]\left(d\xi/d\xi_{\mathrm{H}_2}\right)_{\xi_\mathrm{st}} = mLe_{\mathrm{H}_2},$$

$$\left(dX_{\mathrm{CO}_2}/d\xi\right)_+ = -X_{\mathrm{CO}_2,\mathrm{st}}\Big/(1-\xi_\mathrm{st}), \quad \left(dX_{\mathrm{H}_2\mathrm{O}}/d\xi\right)_+ = -X_{\mathrm{H}_2\mathrm{O},\mathrm{st}}\Big/(1-\xi_\mathrm{st}),$$

$$\left(d\tau/d\xi\right)_+ = -\tau_\mathrm{st}/(1-\xi_\mathrm{st}) = -p. \tag{4}$$

At $\xi_{\mathrm{st}-}$ the gradients are

$$\left(dX_\mathrm{F}/d\xi\right)_- = 0, \quad \left(dX_{\mathrm{O}_2}/d\xi\right)_- = -X_{\mathrm{O}_2,2}/\xi_\mathrm{st} = -2g\left(1+r\right),$$

$$\left(dX_{\mathrm{H}_2}/d\xi\right)_- = -\left(X_{\mathrm{H}_2,2}/\xi_{\mathrm{H}_2,\mathrm{st}}\right)\left(d\xi/d\xi_{\mathrm{H}_2}\right)\xi_\mathrm{st} = -nLe_{\mathrm{H}_2},$$

$$\left(dX_{\mathrm{CO}_2}/d\xi\right)_- = X_{\mathrm{CO}_2,\mathrm{st}}\Big/\xi_\mathrm{st}, \quad \left(dX_{\mathrm{H}_2\mathrm{O}}/d\xi\right)_- = X_{\mathrm{H}_2\mathrm{O},\mathrm{st}}\Big/\xi_\mathrm{st},$$

$$\left(d\tau/d\xi\right)_- = \tau_\mathrm{st}/\xi_\mathrm{st} = s. \tag{5}$$

Here the quantity r is given by the expression

$$r = X_{\mathrm{O}_2,2}(1-\xi_\mathrm{st})\Big/(2\,X_{\mathrm{F},1}\xi_\mathrm{st}) - 1. \tag{6}$$

The diffusive mass flux of any reactant, that is completely consumed at ξ_st, is proportional to the ratio of the gradient of the reactant with respect to ξ evaluated at ξ_st to its Lewis number. It can be readily verified that the quantity r represents the ratio of the fraction of the flux of oxygen that consumes hydrogen to the fraction that consumes fuel. It is identical

to the quantity r defined in the analysis of Niemann et al. (2013). Conservation for the mass flux of element carbon and the mass flux of element oxygen across the reaction zone at ξ_{st} is

$$\left(dX_F/d\xi + dX_{CO_2}/d\xi\right)_+ = \left(dX_F/d\xi + dX_{CO_2}/dx\right),$$

$$\left(2\,dX_{O_2}/d\xi + 2\,dX_{CO_2}/d\xi + dX_{H_2O}/d\xi\right)_+ = \left(2\,dX_{O_2}/d\xi + 2dX_{CO_2}/d\xi + dX_{H_2O}/d\xi\right). \tag{7}$$

The values of $X_{CO_2,st}$ and $X_{H_2O,st}$ are obtained by introducing Eqs. (4), (5), and (6) into Eq. (7),

$$X_{CO_2,st} = g\xi_{st}\left(1 - \xi_{st}\right), \quad X_{H_2O,st} = 2\,g\xi_{st}\left(1 - \xi_{st}\right)\left(1 + 2r\right). \tag{8}$$

Conservation for the mass flux of the element hydrogen across ξ_{st} is

$$\left[2\,dX_F/d\xi + \left(1/Le_{H_2}\right)dX_{H_2}/d\xi + dX_{H_2O}/d\xi\right]_+ = \left[2\,dX_F/d\xi + \left(1/Le_{H_2}\right)dX_{H_2}/d\xi + dX_{H_2O}/d\xi\right]. \tag{9}$$

It follows from Eqs. (4), (5), and (8) that

$$m + n = 4rg. \tag{10}$$

Energy conservation gives the jump condition

$$\left[d\tau/d\xi + 2q\,dX_{O_2}/d\xi + (1 - 4q)\,dX_F/d\xi\right]_+ = \left[d\tau/d\xi + 2q\,dX_{O_2}/d\xi + (1 - 4q)\,dX_F/d\xi\right]. \tag{11}$$

Here $q = Q_{H_2}/Q_F$, and Q_{H_2} is the heat release for the overall reaction $H_2 + \left(1/2\right)O_2 \rightarrow H_2O$. At 298 K, $Q_{H_2} = 242000$ J/mol. It follows from Eqs. (4), (5), and (6) that $p + s = g\left(1 + 4rq\right)$. The value of τ_{st} is

$$\tau_{st} = g\xi_{st}\left(1 - \xi_{st}\right)\left(1 + 4rq\right). \tag{12}$$

Hence, the adiabatic temperature, T_{st}, is

$$T_{st} = T_u + g\xi_{st}\left(1 - \xi_{st}\right)Q_F(1 + 4rq)/\left(c_p W_{N_2}\right). \tag{13}$$

In a classical counterflow problem (Liñán, 1974), the density and coefficient of diffusion are taken to be constant and $u = -\varsigma ax$, where a is the strain rate, and $\varsigma = 1$ for two-dimensional flow and $\varsigma = 2$ for axisymmetric flow. For fixed value of the Lewis number, λ/c_p, is constant. Employing these approximations, Seshadri and Trevino (1989) and Niemann et al. (2013) have shown that

$$2\xi_{H_2} = \text{erfc}\left[\sqrt{Le_{H_2}}\text{erfc}^{-1}\left(2\xi\right)\right]. \tag{14}$$

Here, erfc^{-1} represents the inverse of the complementary error function and not the reciprocal. Kim and Williams (1993) have shown that for small values of the stoichiometic mixture fraction, Eq. (14) holds without the approximations of constant density and coefficient of diffusion. It follows from Eq. (14) that

$$d\xi \Big/ d\xi_{H_2} = \sqrt{Le_{H_2}} \exp\left\{\left(1 - Le_{H_2}\right) \left[\text{erfc}^{-1}\left(2\xi\right)\right]^2\right\}. \tag{15}$$

It is evident from Eq. (15) that the scalar dissipation rate defined using the spatial gradient of ξ_{H_2} will differ from that shown in Eq. (2) by a factor that depends on Le_{H_2} and ξ. The analysis is carried out using the scalar dissipation rate defined in Eq. (2) because it allows comparison with predictions of critical conditions of extinction, obtained from asymptotic analysis, with experimental data.

The outer structure can be constructed using the equations derived in this section if $X_{F,1}$, $X_{O_2,2}$, $X_{H_2,1}$, $X_{H_2,2}$ and the temperatures T_1 and T_2 are known. Eq. (10) together with Eqs. (4), (5), (6), (14), and (15) can be employed to evaluate ξ_{st} and $\xi_{H_2,st}$; Eqs. (12) and (13) can be used to evaluate τ_{st} and T_{st} and Eq. (8) can be employed to evaluate $X_{CO_2,st}$ and $X_{H_2O,st}$. In the analysis described here, ξ_{st} and T_{st} are fixed. Thus, for a selected value of r, Eqs. (12), (4), and (6) are used to evaluate $X_{F,1}$ and $X_{O_2,2}$, and Eqs. (10), (4), and (5) are used to evaluate $X_{H_2,2} + \xi_{H_2, st}\left(X_{H_2,1} - X_{H_2,2}\right)$. It follows that $X_{H_2,2}$ can be evaluated for H_2 addition to the oxidizer stream only, and $X_{H_2,1}$ for H_2 addition to the fuel stream only. The structure of the reaction zone is analyzed in the following sections.

THE REDUCED MECHANISM

A four-step reduced mechanism is employed to describe the chemical reactions taking place in the thin reaction zone at $\xi = \xi_{st}$. This reduced mechanism and rate data are the same as those employed by Bai and Seshadri (1999). Therefore only a brief description is given here. This reduced mechanism was derived from the detailed mechanism shown in Table 1.1 of Peters (1993). Those elementary steps in the detailed mechanism that include compounds with two or more carbon atoms, and those that include nitrogen are neglected (Bai and Seshadri 1999). The range of temperatures considered here are not high enough for nitrogen chemistry to have a significant influence on flame structure and critical conditions of extinction. The four-step mechanism is as follows:

$$
\begin{array}{lrcl}
\text{I.} & CH_4 + 2\,H + H_2O & \rightleftharpoons & CO + 4\,H_2, \\
\text{II.} & CO + H_2O & \rightleftharpoons & CO_2 + H_2, \\
\text{III.} & H + H + M & \rightarrow & H_2 + M, \\
\text{IV.} & O_2 + 3\,H_2 & \rightleftharpoons & 2\,H + 2\,H_2O.
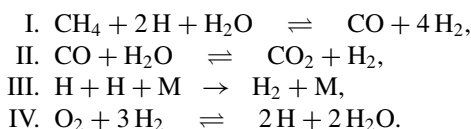\end{array}
$$

Table 1 shows the elementary reactions that are used in the analysis. The numbering here reflects the presence of the other three well-known reversible hydrogen–oxygen shuffle steps. The symbol f appearing in the first column of Table 1 refers to the forward step of a reversible elementary reaction n, and the subscript b later will refer to the reverse step. Reactions 5, 8, and 9, are presumed to be irreversible. The rate constant of elementary step n is $k_n = B_n T^{\alpha_n} \exp[-E_n \big/ (\hat{R}T)]$, where $\hat{R}$ is the universal gas constant. The equilibrium constants for the reversible reactions 1, 6, and 7, respectively, are $K_1 = 12.76 \times \exp\left(-8032/T\right)$, $K_6 = 8.88 \times 10^{-3} \times \exp\left(11169/T\right)$, and $K_7 = 26.21 \times$

Table 1 Rate data

Number	Reaction	B_n	α_n	E_n
1f	$O_2 + H \rightarrow OH + O$	2.000×10^{14}	0.00	70.30
5	$H + O_2 + M \rightarrow HO_2 + M$	2.300×10^{18}	-0.80	0.00
6f	$CO + OH \rightarrow CO_2 + H$	4.400×10^{6}	1.50	-3.10
7f	$CH_4 + H \rightarrow CH_3 + H_2$	2.200×10^{4}	3.00	36.60
8	$CH_3 + H \rightarrow CH_4 \quad k_0$	6.257×10^{23}	-1.80	0.00
	k_∞	2.108×10^{14}	0.00	0.00
9	$CH_3 + O \rightarrow CH_2O + H$	7.000×10^{13}	0.00	0.00

Units are moles, cubic centimeters, seconds, kJoules, Kelvin.

$\exp(-245/T)$. The concentration of the third body C_M is calculated using the relation $C_M = \left[p\bar{W} \big/ \left(\hat{R}T \right) \right] \sum_{i=1}^{n} \eta_i Y_i / W_i$, where p denotes the pressure, $\bar{W}$ is the average molecular weight, and the η_i is the chaperon efficiency of species i. For the elementary reaction 5, the values of η_i are 6.5 for CH_4, 1.5 for CO_2, 0.75 for CO, 0.4 for N_2, 6.5 for H_2O, 0.4 for O_2, and 1.0 for all other species. The rate constant for reaction 8 is calculated using the formula given in Peters (1993) and Bai and Seshadri (1999).

The reaction rates for the global steps, w_k, expressed in terms of the reaction rates of elementary reactions w_n, are

$$w_I = w_{7f} - w_{7b} - w_8, \quad w_{II} = w_{6f} - w_{6b},$$
$$w_{III} = w_5 + w_8, \quad w_{IV} = w_{1f} - w_{1b}. \tag{16}$$

Following the previous analysis of Bai and Seshadri (1999), partial equilibrium approximations are introduced for the elementary steps (2) $H_2 + O \rightleftharpoons OH + H$ and (3) $H_2 + OH \rightleftharpoons H_2O + H$. These approximations give

$$X_{OH} = X_{H_2O} X_H \big/ \left(K_3 X_{H_2} \right) \quad X_O = X_{H_2O} X_H^2 \big/ \left(K_2 K_3 X_{H_2}^2 \right) \tag{17}$$

where $K_2 = 2.28 \times \exp(-963/T)$ and $K_3 = 0.232 \times \exp(7536/T)$ are, respectively, the equilibrium constant of the elementary steps (2) and (3). These partial equilibrium approximations produce reasonable agreement with results of detailed chemistry computations but exhibit noticeable differences under some conditions, primarily for lower oxygen concentrations (Bai and Seshadri, 1999).

THE STRUCTURE OF THE REACTION ZONE

Chemical reactions represented by the four global steps of the reduced mechanism take place in the reaction zone. In this zone, the convective terms in the species balance equations and in the energy conservation equation are neglected because they are small when compared with the diffusive and the reactive terms. For convenience, the definitions

$$x_i \equiv X_i \big/ Le_i, \quad \omega_k \equiv W_{N_2}^2 w_k / \rho^2, \quad Q_k \equiv (-\Delta H_k) \big/ Q_F \tag{18}$$

are introduced, where $(-\Delta H_k)$ is the heat release in the overall step k of the reduced mechanism. The heats of formation at 298 K are CH_4: -74.87 kJ/mol, CO: -110.53 kJ/mol, CO_2: -393.51 kJ/mol, H_2O: -241.826 kJ/mol, and H: 218 kJ/mol.

Thus $(-\Delta H_\mathrm{I}) = -229.834\,\mathrm{kJ}$, $(-\Delta H_\mathrm{II}) = -41.154\,\mathrm{kJ}$, $(-\Delta H_\mathrm{III}) = -436\,\mathrm{kJ}$, and $(-\Delta H_\mathrm{IV}) = -47.652\,\mathrm{kJ}$. Thus $Q_\mathrm{I} = 0.287$, $Q_\mathrm{II} = 0.052$, $Q_\mathrm{III} = 0.543$, and $Q_\mathrm{IV} = 0.059$. From the definition of Q_k, it follows that $Q_\mathrm{I} + Q_\mathrm{II} + Q_\mathrm{III} + 2Q_\mathrm{IV} = 1$.

Seven reactive species appear in the four-step reduced mechanism. Since there are three chemical elements in these reactive species, four independent species balance equations can be written. The independent differential balance equations selected are those for the fuel (CH_4), H-radicals, CO, and H_2. The equations written in terms of the variables defined in Eq. (18) are

$$[\chi W_{N_2}/(2\rho)]\, d^2 x_\mathrm{F}/d\xi^2 = \omega_\mathrm{I},$$

$$[\chi W_{N_2}/(2\rho)]\, d^2 x_\mathrm{H}/d\xi^2 = 2\omega_\mathrm{I} + 2\omega_\mathrm{III} - 2\omega_\mathrm{IV},$$

$$[\chi W_{N_2}/(2\rho)]\, d^2 x_\mathrm{CO}/d\xi^2 = -\omega_\mathrm{I} + \omega_\mathrm{II},$$

$$[\chi W_{N_2}/(2\rho)]\, d^2 x_{O_2}/d\xi^2 = \omega_\mathrm{IV.}$$

$$(19)$$

The remaining species in the four-step mechanism are obtained from coupling relations satisfying conservation of chemical elements. The temperature is evaluated using energy conservation. The conservation conditions are

$$d^2(4x_\mathrm{F} + x_\mathrm{H}/2 + x_\mathrm{CO} + x_{H_2} - 2x_{O_2})/d\xi^2 = 0,$$

$$d^2(x_{CO_2} + x_\mathrm{F} + x_\mathrm{CO})/d\xi^2 = 0,$$

$$d^2(x_{H_2O} + 2x_\mathrm{F} + x_\mathrm{H}/2 + x_{H_2})/d\xi^2 = 0,$$

$$d^2(\tau + q_F x_\mathrm{F} + q_H x_\mathrm{H} + q_{CO} x_\mathrm{CO} + q_{O_2} x_{O_2})/d\xi^2 = 0,$$

$$(20)$$

where $q_F = (Q_\mathrm{I} + Q_\mathrm{II} - Q_\mathrm{III})$, $q_H = Q_\mathrm{III}/2$, $q_{CO} = Q_\mathrm{II}$, and $q_{O_2} = (Q_\mathrm{III} + Q_\mathrm{IV})$.

The global reactions of the reduced four-step mechanism take place in various layers within the reaction zone. The characteristic Damköhler numbers, D_I, D_II, D_III and D_IV, for the global steps are constructed with flow time given by the reciprocal of the scalar dissipation rate and the chemical time given by the forward rate of the elementary steps 7f, 6f, 5, and 1f, respectively. Their values are all large. Since radicals participate in all elementary steps, global step IV is active in the entire reaction zone. Previous studies, for example that by Bai and Seshadri (1999), show that the distinguished limit $D_\mathrm{I} \gg D_\mathrm{III}$, with the ratio $D_\mathrm{II}/D_\mathrm{III}$ of the order of unity, applies. This distinguished limit is employed here. Therefore the reaction zone is made up of two layers, an oxidation layer of thickness of the order of ϵ, where global steps II and III are dominant, and an inner layer of thickness of the order of δ, where global step I is dominant. The ordering $\delta \ll \varepsilon \ll 1$, consistent with the presumed ordering of the Damköhler numbers, is employed in the analysis. The accuracy of this approximation is checked after completing the analysis.

Figures 2 and 3, respectively, are schematic illustrations of the structure of the reaction zone with hydrogen added to the fuel stream and to the oxidizer stream. The profile of temperature and profiles of CH_4, O_2, H_2, CO, and H are shown. The temperature profiles shown by the dashed lines in Figures 2 and 3 are projections from the outer structure into
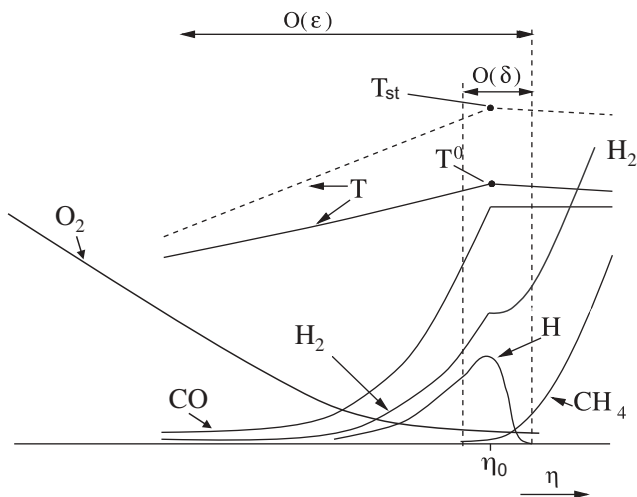
Figure 2 Schematic illustration of the structure of the reaction zone at ξ_{st} for hydrogen added to the fuel stream. The figure shows the inner layer and the oxidation layer.
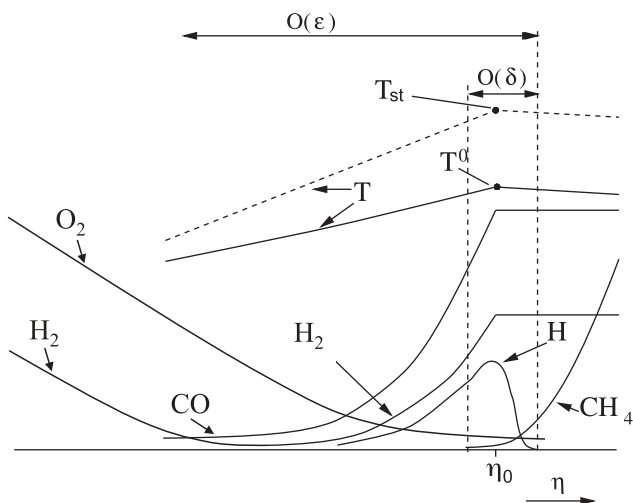

Figure 3 Schematic illustration of the structure of the reaction zone around ξ_{st} for hydrogen added to the oxidizer stream. The figure shows the inner layer and the oxidation layer.

the reaction zone. The quantity T^0 is the peak temperature in the reaction zone. Since the chemical reactions take place with finite rates, $T^0 < T_{st}$.

Figures 2 and 3 show the relative location of these layers with respect to each other in terms of the stretched coordinate η, which is used as the independent variable in the analysis of the oxidation layer. The stretched coordinate is so defined that the inner layer is located around $\eta = \eta_0$. The temperature and the scalar dissipation rate evaluated at η^0 are represented by T^0 and χ^0, respectively. In the inner layer, the global steps I and IV are

active. Fuel, CH_4, is completely consumed there, and the intermediate species H_2 and CO are formed. As a consequence, in the reaction zone, X_F is of the order of δ. Bai and Seshadri (1999) have shown that X_H is also of the order of δ. In the oxidation layer, the global steps II, III, and IV take place. Here O_2, added H_2, and CO and H_2 produced in the inner layer are oxidized to CO_2 and H_2O. Oxygen is consumed primarily in the oxidation layer. As a consequence, in the reaction zone X_{O_2}, X_{H_2}, and X_{CO} are of the order of ϵ. It is noteworthy that consumption of H_2 primarily takes place in the oxidation layer irrespective of the reactant stream to which it is added. As a consequence, the analysis of Bai and Seshadri (1999) of the inner layer of methane flames is applicable here with modest changes. The only change required is replacing the value of X_{O_2} from a quantity of the order of unity, which is obtained from analysis of the outer structure, with a quantity of the order of ϵ, which is obtained from analysis of the oxidation layer. Asymptotic analysis of the inner layer and the oxidation layer provide sufficient conditions for calculating the scalar dissipation rate, χ^0, at extinction.

The Structure of the Oxidation Layer

In the oxidation layer, the concentration of fuel is negligibly small; therefore the influence of the global step I is neglected. Steady-state approximation is introduced for H. It follows from Eq. (19) that $\omega_{III} = \omega_{IV}$. Using Eqs. (17) and (18), the result

$$X_H = K_1^{1/2} K_2^{1/2} K_3 X_{H_2}^{3/2} X_{O_2}^{1/2} (1 - k_5 C_M / k_{1f})^{1/2} / X_{H_2O,st} \tag{21}$$

is obtained. These approximations reduce the four-step mechanism to a two-step mechanism:

II. $CO + H_2O \quad \rightleftharpoons \quad CO_2 + H_2,$
III$'$. $O_2 + 2H_2 \quad \rightleftharpoons \quad 2H_2O.$
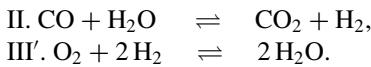
The reaction rate of the global step III$'$ is the same as that for the global step III of the four-step mechanism. There are now five reactive species in the global steps II and III$'$ and three elements. Therefore, two independent species balance equation can be written. The differential equations for O_2 and CO are selected for describing the structure of oxidation layer. Thus,

$$d^2 x_{O_2}/d\xi^2 = \left[AD_{III}G_{III}/(2^{3/2}g^2)\right] x_{O_2}^{3/2} x_{H_2}^{3/2} (1 - G_b\kappa)^{1/2},$$
$$d^2 x_{CO}/d\xi^2 = \left[AD_{III}^{3/4} SG_{II}/\left(2^{1/2}g\right)\right] x_{O_2}^{1/2} x_{H_2}^{1/2} \left(x_{CO} - \alpha G_a x_{H_2}\right) (1 - G_b\kappa)^{1/2}. \tag{22}$$

Coupling relations deduced from Eq. (20) are

$$d^2 \left(x_{CO} + x_{H_2} - 2x_{O_2}\right)/d\xi^2 = 0,$$
$$d^2 \left(x_{CO_2} + x_{CO}\right)/d\xi^2 = 0,$$
$$d^2 \left(x_{H_2O} + x_{H_2}\right)/d\xi^2 = 0, \tag{23}$$
$$d^2 \left(\tau + q_{CO}x_{CO} + q_{O_2}x_{O_2}\right)/d\xi^2 = 0.$$

The quantities D_{III}, S, A, α, and κ appearing in Eq. (22) are defined as

$$D_{\mathrm{III}} \equiv 2^{5/2} \rho^0 g^2 k_5^0 C_{\mathrm{M}}^0 \left(K_1^0 K_2^0 K_3^{0^2}\right)^{1/2} Le_{\mathrm{H_2}}^{3/2} Le_{\mathrm{O_2}}^{3/2} / \left(\chi^0 X_{\mathrm{H_2O,st}} W_{\mathrm{N_2}}\right),$$

$$S \equiv D_{\mathrm{III}}^{1/4} k_{6f}^0 Le_{\mathrm{CO}} X_{\mathrm{H_2O,st}} / \left(2 k_5^0 C_{\mathrm{M}}^0 K_3^0 g Le_{\mathrm{H_2}} Le_{\mathrm{O_2}}\right), \quad A = \chi^0/\chi, \tag{24}$$

$$\alpha \equiv K_3^0 X_{\mathrm{CO_2,st}} Le_{\mathrm{H_2}} / \left(K_6^0 X_{\mathrm{H_2O,st}} Le_{\mathrm{CO}}\right), \quad \kappa \equiv k_5^0 C_{\mathrm{M}}^0 / k_{1f}^0.$$

Here χ^0 is the scalar dissipation rate evaluated in the reaction zone, at the location η^0 indicated in Figures 2 and 3. The superscript 0 over the rate constants and equilibrium constants indicates that their values are evaluated at $T = T^0$. The quantities G_{II}, G_{III}, G_{a}, and G_{b} are defined as

$$G_{\mathrm{II}} = \rho k_{6f} K_1^{1/2} K_2^{1/2} \Big/ \left(\rho^0 k_{6f}^0 K_1^{0^{1/2}} K_2^{0^{1/2}}\right) = \exp\left[-m_{\mathrm{II}}\left(1/T - 1/T^0\right)\right],$$

$$G_{\mathrm{III}} = \rho k_5 C_{\mathrm{M}} K_1^{1/2} K_2^{1/2} K_3 \Big/ \left(\rho^0 k_5^0 C_{\mathrm{M}}^0 K_1^{0^{1/2}} K_2^{0^{1/2}} K_3^0\right) = \exp\left[-m_{\mathrm{III}}\left(1/T - 1/T^0\right)\right],$$

$$G_{\mathrm{a}} = K_3 K_6^0 \big/ \left(K_3^0 K_6\right) = \exp\left[-m_{\mathrm{a}}\left(1/T - 1/T^0\right)\right], \tag{25}$$

$$G_{\mathrm{b}} = k_{1f}^0 k_5 C_{\mathrm{M}} \big/ \left(k_{1f} k_5^0 C_{\mathrm{M}}^0\right) = \exp\left[-m_{\mathrm{b}}\left(1/T - 1/T^0\right)\right].$$

The quantities m_{II}, m_{III}, m_{a}, and m_{b} represent the effective activation temperature. They are evaluated from the rate data shown in Table 1. The contribution of the temperature exponent of the rate constant, α_n, is estimated employing the approximation $T^{\alpha_n} = T_m^{\alpha_n} \exp(\alpha_n) \exp(-\alpha_n T_m/T)$ (Seshadri and Peters, 1988; Yang and Seshadri, 1992). Here, T_m is a reference temperature. For $T_m = 1600$ K, the values $m_{\mathrm{II}} = 4925$ K, $m_{\mathrm{III}} = -7519$ K, $m_{\mathrm{a}} = 3632$ K, and $m_{\mathrm{b}} = -11335$ K are obtained. Since the effective activation temperatures represented by m_{II}, m_{III}, and m_{a} are not too large, the approximation, $G_{\mathrm{II}} = G_{\mathrm{III}} = G_{\mathrm{a}} = 1$ is made. The differences between the critical conditions of extinction calculated with and without introducing this approximation were found to be small. Furthermore, the approximation $A = 1$ is introduced because changes in values of the scalar dissipation rate in the reaction zone are expected to be small.

The expansions

$$\xi - \xi_{\mathrm{st}} = \varepsilon\left(\eta + \eta^0\right), \quad x_{\mathrm{CO}} = \varepsilon 2 g z_{\mathrm{CO}},$$

$$x_{\mathrm{O_2}} = \varepsilon g\left[z_{\mathrm{O_2}} - 2\left(1 + r\right)\left(\eta + \eta^0\right)\right],$$

$$x_{\mathrm{H_2}} = \varepsilon 2 g\left[z_{\mathrm{O_2}} - z_{\mathrm{CO}} - n\left(\eta + \eta^0\right) / (2g)\right], \tag{26}$$

$$\tau = \tau_{\mathrm{st}} - \varepsilon\left[2 g q_{CO} z_{\mathrm{CO}} + g q_{O_2} z_{\mathrm{O_2}} - s\left(\eta + \eta^0\right)\right],$$

are introduced, where ϵ is small and the variables η, $z_{\mathrm{O_2}}$, and z_{CO}, are presumed to be of the order of unity. By matching the profiles of CO and $\mathrm{O_2}$ in the oxidation layer with those in the outer structure in the region $\xi < \xi_{\mathrm{st}}$ given by Eq. (5), the following results are obtained

$$dz_{\mathrm{O_2}}/d\eta = dz_{\mathrm{CO}}/d\eta = 0 \quad \text{as} \quad \eta \to -\infty. \tag{27}$$

The expansions for x_{H_2} and τ shown in Eq. (26) are chosen so that they satisfy the coupling relations shown in Eq. (23) and match with the slopes shown in Eq. (5) as $\eta \to -\infty$.

The small expansion parameter ϵ is chosen so that it can be calculated from the equation

$$\varepsilon = D_{III}^{-1/4}. \tag{28}$$

Introducing the expansions given by Eq. (26) into Eq. (22) gives

$$d^2 z_{O_2}/d\eta^2 = (1 - G_b \kappa)^{1/2} \left[z_{O_2} - 2 (1+r) \left(\eta + \eta^0 \right) \right]^{3/2} \left[z_{O_2} - z_{CO} - n \left(\eta + \eta^0 \right) / (2g) \right]^{3/2},$$

$$d^2 z_{CO}/d\eta^2 = S (1 - G_b \kappa)^{1/2} \left[z_{O_2} - 2 (1+r) \left(\eta + \eta^0 \right) \right]^{1/2} \left[z_{O_2} - z_{CO} - n \left(\eta + \eta^0 \right) / (2g) \right]^{1/2}$$

$$\times \left\{ z_{CO} - \alpha \left[z_{O_2} - z_{CO} - n \left(\eta + \eta^0 \right) / (2g) \right] \right\} \tag{29}$$

In view of Eqs. (3) and (26), $T = T_{st} - \varepsilon \left[2g q_{CO} z_{CO} + g q_{O_2} z_{O_2} - s \left(\eta + \eta^0 \right) \right] Q_F / \left(c_p W_{N_2} \right)$. At $\eta = 0$, the values of z_{CO} and z_{O_2} are z_{CO}^0 and $z_{O_2}^0$ respectively. Hence, the temperature at $\eta = 0$, T^0, is

$$T^0 = T_{st} - \varepsilon \left(2g q_{CO} z_{CO}^0 + g q_{O_2} z_{O_2}^0 - s \eta^0 \right) Q_F / \left(c_p W_{N_2} \right). \tag{30}$$

It follows from Eq. (30) that

$$\varepsilon = c_p W_{N_2} \left(T_{st} - T^0 \right) / \left[\left(2g q_{CO} z_{CO}^0 + g q_{O_2} z_{O_2}^0 - s \eta^0 \right) Q_F \right]. \tag{31}$$

To the leading order, an expansion for $1/T$ gives

$$1/T - 1/T^0 = \varepsilon \left[2g q_{CO} \left(z_{CO} - z_{CO}^0 \right) + g q_{O_2} \left(z_{O_2} - z_{O_2}^0 \right) - s\eta \right] Q_F / \left(c_p W_{N_2} T^{0^2} \right). \tag{32}$$

Eq. (21) shows that the steady-state concentration of H is proportional to the square root of $1 - G_b \kappa$. The value of H is zero when $G_b \kappa = 1$. The temperature at which this is achieved is represented by T_c. Thus the steady-state approximation for H breaks down at $\eta = \eta_c$, where $z_{CO} = z_{CO,c}$ and $z_{O_2} = z_{O_2,c}$. Thus

$$2g q_{CO} \left(z_{CO,c} - z_{CO}^0 \right) + g q_{O_2} \left(z_{O_2,c} - z_{O_2}^0 \right) - s\eta_c = T^{0^2} \left(-\ln \kappa \right) c_p W_{N_2} / \left[\varepsilon Q_F \left(-m_b \right) \right]. \tag{33}$$

Boundary conditions at $\eta = 0$ are obtained for Eq. (29) from jump conditions across the inner layer. To obtain these conditions, the influence of the global steps II and III on the structure of the inner layer is neglected. Hence, the coupling relations deduced from Eq. (19) are $d^2 \left(x_F + x_{CO} \right) / d\xi^2 = 0$, $d^2 \left(x_F + 3x_H/2 + x_{H_2} \right) / d\xi^2 = 0$, and $d^2 \left(x_{O_2} + x_H/2 - x_F \right) / d\xi^2 = 0$. Integrating these equations once and matching the slopes with those in Eq. (4) gives the results $d \left(x_F + x_{CO} \right) / d\xi = g$, $d \left(x_F + 3x_H/2 + x_{H_2} \right) / d\xi = g + m$, and $d \left(x_{O_2} + x_H/2 - x_F \right) / d\xi^2 = -g$. Using the expansions given by Eq. (26), the boundary conditions
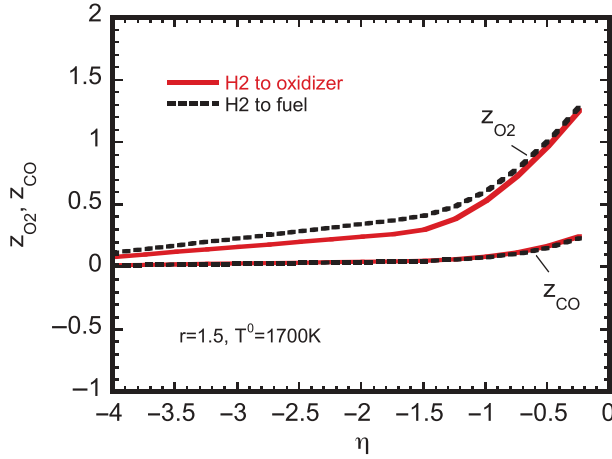
Figure 4 Profiles of z_{CO} and z_{O_2} as functions of η obtained from numerical integration of Eq. (29) for $r = 1.5$, $T^0 = 1700$ K, $\alpha = 0$. The solid line represents profiles for H_2 addition to the oxidizer stream ($m = 0$), $S = 2.73$, $n = 0.55$, and the broken lines for H_2 addition to the fuel stream ($n = 0$), $S = 2.84$, $m = 0.81$.

$$dz_{CO}/d\eta = 1/2, \quad dz_{O_2}/d\eta = 1 + 2r, \tag{34}$$

are obtained at $\eta = 0$.

The presence of the quantity r in Eq. (29) indicates that addition of H_2 either to the oxidizer stream or to the fuel stream enhances the rates of consumption of O_2 and CO in the oxidation layer. For H_2 addition to the oxidizer stream, the quantity n in Eq. (29) provides an additional increase to the rates of consumption of O_2 and CO in the oxidation layer. Thus for a given value of r, the structure of the oxidation layer for H_2 addition to the oxidizer stream is not the same as that for H_2 addition to the fuel stream.

Eq. (29) is integrated numerically by employing the boundary conditions given by Eqs. (27) and (34). Figure 4 shows representative resulting profiles of z_{CO} and z_{O_2}, as functions of η. The profiles are used to obtain the values of z_{CO}^0 and $z_{CO_2}^0$. The values of $X_{O_2}^0$ and $X_{H_2}^0$ are then obtained from

$$X_{O_2}^0 = \varepsilon g Le_{O_2} \left[z_{O_2}^0 - 2\left(1 + r\right)\eta^0 \right], \quad X_{H_2}^0 = \varepsilon 2g Le_{H_2} \left[z_{O_2}^0 - z_{CO}^0 - n\eta^0/\left(2g\right) \right]. \tag{35}$$

The Structure of the Inner Layer

Bai and Seshadri (1999) have analyzed the structure of the inner layer with O_2 of the order of unity in this layer represented by $X_{O_2,p}$. The value of $X_{O_2,p}$ was obtained from analysis of the outer structure (Bai and Seshadri, 1999). The results of this previous analysis is applicable here after replacing $X_{O_2,p}$ by $X_{O_2}^0$. This is permissible because in the present analysis, as well as in the analysis of Bai and Seshadri (1999), the mass fraction of O_2 is large in comparison to δ. The value of δ, obtained from the analysis of Bai and Seshadri (1999) after making the indicated substitution, is

$$\delta^2 = \frac{2^{3/2} g^2 k_5^0 C_M^0 k_8^0 k_2^{0\,1/2} Le_{O_2}{}^{3/2} Le_{H_2}{}^{3/2} \varepsilon^4}{k_{7f}^0 k_9^0 K_1^{0\,1/2} Le_F X_{O_2}^0 X_{H_2}^0}. \tag{36}$$

Following the analysis of Bai and Seshadri (1999), two coupled second-order differential equations, one for CH_4 and the other for H, are obtained. These equations include an eigenvalue ω defined for the analysis here with O_2 of the order of ϵ

$$\omega^2 = \frac{2^{7/2} g^4 \varepsilon^4 k_5^0 C_M^0 k_8^{03} K_2^{01/2} X_{H_2O,st}{}^2 Le_H{}^2 Le_{O_2}{}^{3/2} Le_{H_2}{}^{3/2}}{k_{7f}^0 k_9^{03} K_1^{05/2} K_3^{02} X_{O_2}^0{}^3 X_{H_2}^0{}^3 Le_F}. \tag{37}$$

The coupled differential equations for CH_4 and H are required to satisfy five boundary conditions (Bai and Seshadri 1999). The equations are integrated numerically, with the additional boundary condition being used to obtain ω.

SCALAR DISSIPATION RATE

The results of the asymptotic analysis are employed to predict the value of χ_q^0, which is the value of χ^0 at extinction. For given values of temperature and mass fractions of the reactants at the boundaries, the outer structure can be constructed using the procedure described at the end of the section entitled The Outer Structure. A value of η^0 is selected. The goal is to predict the scalar dissipation rate, χ^0, that is consistent with this selected value of η^0. An iterative procedure is employed. It begins by selecting an appropriate value of T^0. The rate constants and equilibrium constants are evaluated. A second iteration is required, and it is carried out after selecting an appropriate value of ϵ. This permits evaluation of the quantity S given by Eq. (24). Eqs. (29) are integrated and the results are used to obtain $z_{O_2}^0$ and z_{CO}^0. The quantity ϵ is calculated using Eq. (31) and compared with the selected value. The iteration is continued until the selected value of ϵ agrees with the calculated value. The quantities $X_{O_2}^0$ and $X_{H_2}^0$ are calculated using Eq. (35). The coupled differential equations for CH_4 and H describing the structure of the inner layer in Bai and Seshadri (1999) are integrated and the value of ω is obtained. This is compared with ω calculated using Eq. (37). If they are not the same, the procedure is repeated with a different value of T^0 until the value of ω, obtained from integration of the coupled differential equations for CH_4 and H, agrees with that calculated using Eq. (37). The value of χ^0, which is consistent with the selected value of η^0, is calculated by recasting Eq. (24) as

$$\chi^0 = 2^{5/2} \rho^0 g^2 k_5^0 C_M^0 \left(K_1^0 K_2^0 K_3^{0^2} \right)^{1/2} Le_{H_2}^{3/2} Le_{O_2}^{3/2} \epsilon^4 / \left(X_{H_2O,st} W_{N_2} \right). \tag{38}$$

The entire procedure is repeated with another selected value of η^0.

The classical C-shaped curve is obtained when T^0 is plotted as a function of $\left(\chi^0 \right)^{-1}$. The value of $\left(\chi^0 \right)^{-1}$, where its derivative with respect to T^0 in the C-shaped curve is zero, represents the critical condition at extinction. At this critical condition, the value of χ^0 is denoted by χ_q^0. To facilitate comparison of predictions of asymptotic analysis of critical conditions of extinction with numerical and experimental results, the scalar dissipation rate at ξ_{st}, denoted χ_{st}, is calculated using the following expression (Peters, 1984; Seshadri and Peters, 1988; Yang and Seshadri, 1992):

$$\chi_{st} = \chi^0 \exp \left[-2\epsilon \eta^0 / \xi_{st} \right]. \tag{39}$$

The value of χ_{st} at extinction is represented by $\chi_{st,q}$.

The experimental results of Niemann et al. (2013) give the strain rates at extinction, a_e. Kim and Williams (1993) have derived a relation between $\chi_{st,q}$ and extinction strain rate a_e given by

$$\chi_{st,q} = \frac{a_e}{2\pi} \frac{3\left[(T_{st}/T_u)^{1/2} + 1\right]^2}{2(T_{st}/T_u)^{1/2} + 1} \times \exp\left\{-2\left[\text{erfc}^{-1}(2\xi_{st})\right]^2\right\}. \tag{40}$$

Here, erfc^{-1} is the inverse of the complementary error function as in Equation (14).

RESULTS AND DISCUSSION

Niemann et al. (2013) measured strain rates of methane flames at extinction, a_e, with hydrogen added either to the fuel stream or to the oxidizer stream. The temperature of the reactant streams at the boundaries were maintained at 298 K, and the pressure was 1 atm. Three sets of experimental data were obtained. In each set, the mass fractions of the reactants at the boundaries were selected so that the adiabatic temperature T_{st} and the stoichiometric mixture fraction, ξ_{st}, are the same. In one set of experiments, $T_{st} = 2000$ K and $\xi_{st} = 0.055$, and extinction strain rates were measured for various amounts of H_2 added to the oxidizer stream represented by $Y_{H_2,2}$. In the second set, $T_{st} = 2000$ K and $\xi_{st} = 0.055$, and extinction strain rates were measured for various amounts of H_2 added to the fuel stream represented by $Y_{H_2,1}$. In the third set, $T_{st} = 2100$ K and $\xi_{st} = 0.055$, and extinction strain rates were measured for various values of $Y_{H_2,1}$. It follows from Eq. (40) that the scalar dissipation rate at extinction, $\chi_{st,q}$, is proportional to the strain rate at extinction, a_e, and the constant of proportionality is the same for each set of experimental data. This permits comparison of predictions of asymptotic analysis with experimental data, because asymptotic analysis gives the scalar dissipation rate at extinction and not the strain rate.

In performing the calculations described in the section entitled Scalar Dissipation Rate, for simplicity the concentration of the third body, C_M^0, the density, ρ^0, and the heat capacity, c_p, are evaluated using the relations given in Smooke and Giovangigli (1991) and Bai and Seshadri (1999). These relations are $C_M^0 = 0.02027/T^0$ mol/cm^3, $\rho^0 = 0.000351/T^0$ kg/cm^3, and $c_p = 1045 + 0.24T - 0.2T^2$ J/(kg·K). The molecular weights are $W_F = 0.016$ kg/mol, $W_{N_2} = 0.028$ kg/mol, $W_{O_2} = 0.032$ kg/mol, and $W_{H_2} = 0.002$ kg/mol, and the Lewis numbers of various species are $Le_F = 0.97$, $Le_{H_2} = 0.3$, $Le_{CO} = 1.11$, and $Le_H = 0.2$ (Smooke and Giovangigli, 1991). Furthermore, predictions of scalar dissipation rate at extinction with $\alpha \neq 0$ and with $\alpha = 0$ in Eq. (29) were found to be nearly the same. Therefore all predictions shown here are with $\alpha = 0$. This approximation is equivalent to neglecting the contribution of the reverse step of global reaction II of the reduced mechanism. The predictions of the asymptotic analysis and comparison with experimental data are shown in Figures 5–14. The predictions in all figures, except Figure 10, are at fixed $T_{st} = 2000$ K and $\xi_{st} = 0.055$. The predictions and measurements in Figure 10 are at $T_{st} = 2000$ K, $\xi_{st} = 0.055$ and at $T_{st} = 2100$ K and $\xi_{st} = 0.055$.

Figures 5 and 7 show T^0 as a function of $(\chi^0)^{-1}$, and Figures 6 and 8 show $X_{O_2}^0$ as a function of $(\chi^0)^{-1}$. Figures 5 and 6 are predictions for various amounts of hydrogen added to the oxidizer stream, and Figures 7 and 8 are corresponding predictions for hydrogen added to the fuel stream. All the curves in these figures show the classical C-shaped behavior. The upper branch of the C-shaped curve for T^0 vs $(\chi^0)^{-1}$ and the lower branch for $X_{O_2}^0$ vs $(\chi^0)^{-1}$ are stable. With decreasing values of $(\chi^0)^{-1}$, the flame temperature decreases
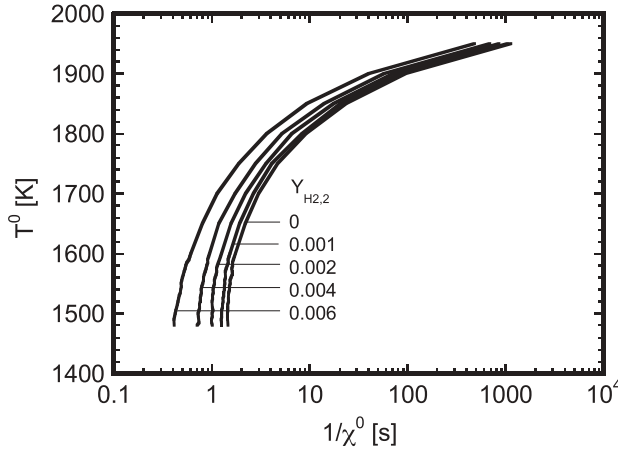
Figure 5 The flame temperature, T^0, as a function of $\left(\chi^0\right)^{-1}$, for various amounts of hydrogen added to the oxidizer stream only, at fixed $T_{st} = 2000$ and $\xi_{st} = 0.055$.
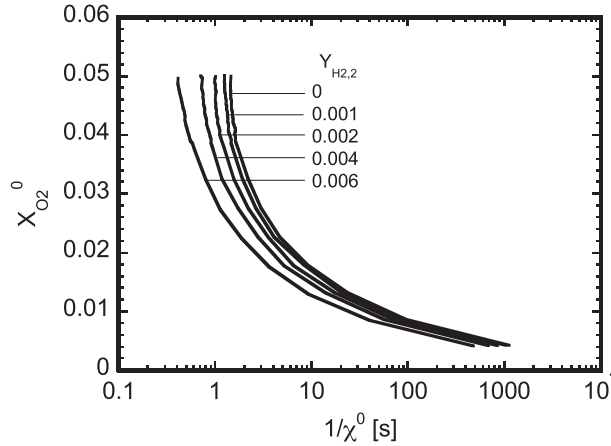

Figure 6 The normalized mass fraction of O_2, $X_{O_2}^0$, as a function of $\left(\chi^0\right)^{-1}$ for various amounts of hydrogen added to the oxidizer stream only, at fixed $T_{st} = 2000$ and $\xi_{st} = 0.055$.

and the oxidizer leakage represented by $X_{O_2}^0$ increases. All curves show that there are no solutions for values of $(\chi^0)^{-1}$ below a critical value. This critical value of $(\chi^0)^{-1}$ is the scalar dissipation rate at extinction. It is noteworthy that at extinction the value of T^0 and $X_{O_2}^0$ are nearly the same for all cases considered here.

From Eq. (40), it is deduced that at fixed T_{st} and ξ_{st}, the ratio $a_e/a_{e,0} = \chi_{st,q}/\chi_{st,q,0}$, where $a_{e,0}$ and $\chi_{st,q,0}$ are the strain rate and scalar dissipation rate at extinction for $Y_{H_2,2} = Y_{H_2,1} = 0$. Therefore, the ratio of strain rates at extinction, $a_e/a_{e,0}$, measured by Niemann et al. (2013) are presumed to be equal to the ratio $\chi_{st,q}/\chi_{st,q,0}$. Figure 9 shows the ratio $\chi_{st,q}/\chi_{st,q,0}$ as a function of hydrogen added to the oxidizer stream, $Y_{H_2,2}$, while Figure 10 shows similar data for hydrogen addition of the fuel stream, $Y_{H_2,1}$. Figure 10 also compares predictions with experimental data obtained at $T_{st} = 2100$ K and $\xi_{st} = 0.055$. The symbols in Figures 9 and 10 represent experimental data and lines are predictions. For
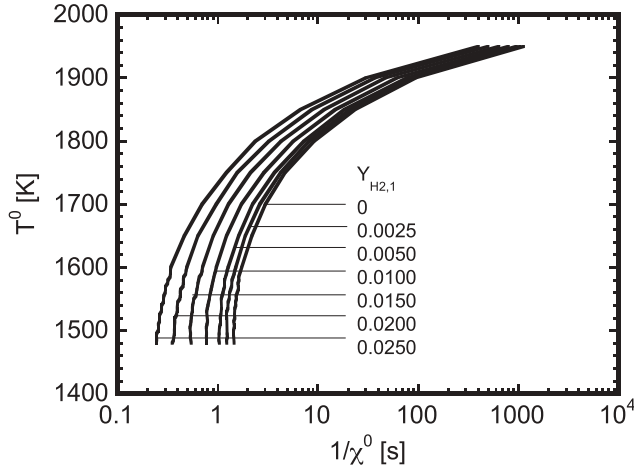
Figure 7 The flame temperature, T^0, as a function of $(\chi^0)^{-1}$, for various amounts of hydrogen added to the fuel stream only, at fixed $T_{st} = 2000$ and $\xi_{st} = 0.055$.
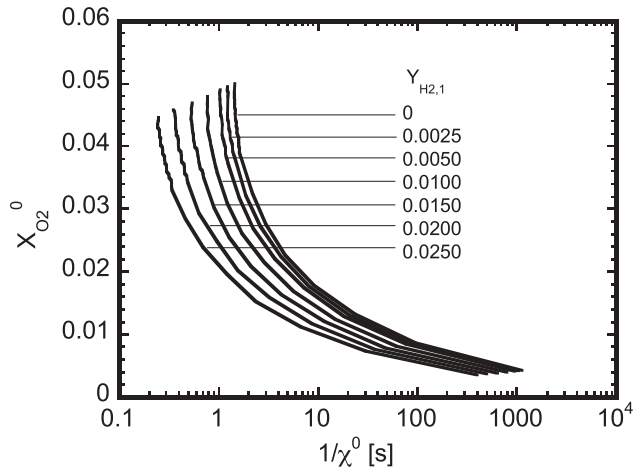

Figure 8 The normalized mass fraction of O_2, $X_{O_2}^0$, as a function of $(\chi^0)^{-1}$, for various amounts of hydrogen added to the fuel stream only, at fixed $T_{st} = 2000$ and $\xi_{st} = 0.055$.

$Y_{H_2,1} = Y_{H_2,2} = 0$, the value of $\chi_{st,q,0}$ is calculated by employing Eq. (40) using the experimentally measured value of a_e at $T_{st} = 2000$ K and $\xi_{st} = 0.055$ was 3.5 s^{-1}. This is to be compared with the predicted value of $\chi_{st,q,0} = 1.05$ s^{-1} at $T_{st} = 2000$ K and $\xi_{st} = 0.055$. The differences between the measured and predicted values of $\chi_{st,q}$ are attributed to inaccuracies in calculating $\chi_{st,q}$ by employing Eq. (40) from measured values of a_e and inaccuracies in calculating this quantity by employing Eq. (39) from predicted value of χ^0. In view of these inaccuracies, comparisons of the predicted values of the ratio $\chi_{st,q}/\chi_{st,q,0}$ with the measured values of $a_e/a_{e,0}$ will be more indicative of the accuracy with which the asymptotic analysis captures the influence of hydrogen on flame structure than with comparisons of absolute
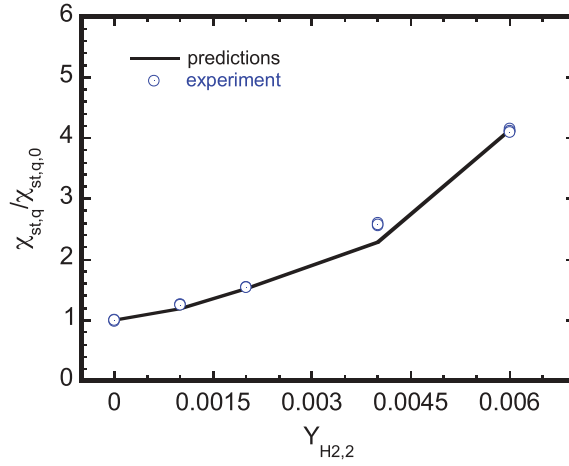
Figure 9 The ratio $\chi_{st,q}/\chi_{st,q,0}$ at extinction for various values of hydrogen added only to the oxidizer stream, $Y_{H_2,2}$, at fixed $T_{st} = 2000$ and $\xi_{st} = 0.055$. The symbols represent experimental data, and the lines are predictions of the asymptotic analysis.
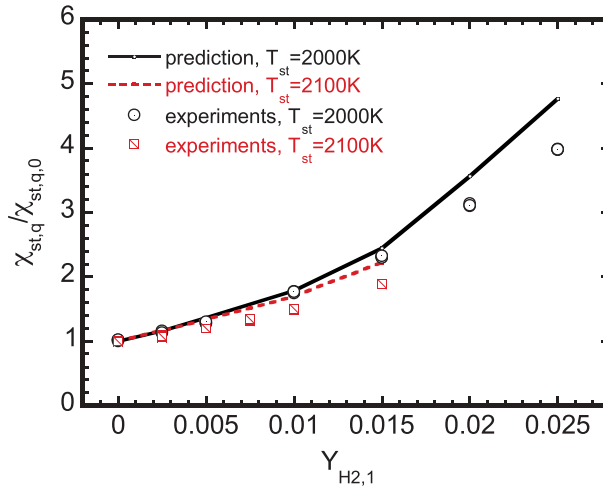

Figure 10 The ratio $\chi_{st,q}/\chi_{st,q,0}$ at extinction for various values of hydrogen added only to the fuel stream, $Y_{H_2,1}$ at fixed $T_{st} = 2000$ and $\xi_{st} = 0.055$, and at fixed $T_{st} = 2100$ and $\xi_{st} = 0.055$. The symbols represent experimental data, and the lines are predictions of the asymptotic analysis.

values. The ratios help to remove the inaccuracies that are present in predictions of critical conditions of extinction of methane flames without added hydrogen. Figure 9 shows that the predictions of the asymptotic analysis agree well with experimental data. Figure 10 shows that the predictions agree well with experimental data at low values of $Y_{H_2,1}$, while at higher values of $Y_{H_2,1}$, the predictions begin to deviate from the measurements, but not appreciably.

Figure 11 shows the the predicted value of the ratio $\chi_{st,q}/\chi_{st,q,0}$ as a function of r for hydrogen added to the oxidizer stream (broken line) and to the fuel stream (solid line). At a given value of r, the predicted value of this ratio for hydrogen added to the fuel stream
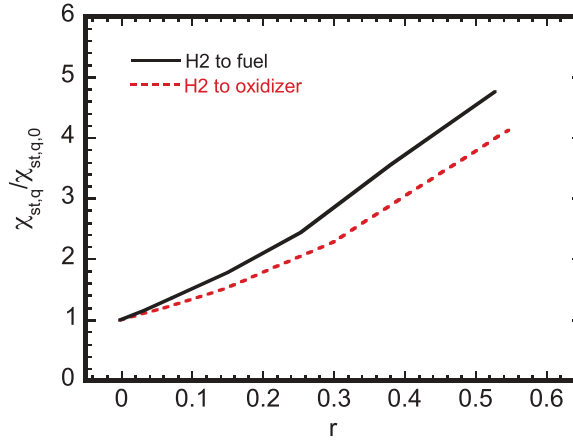
Figure 11 The predicted value of the ratio $\chi_{st,q}/\chi_{st,q,0}$ as a function of r for hydrogen added to the oxidizer stream (broken line) and to the fuel stream (solid line) at fixed $T_{st} = 2000$ and $\xi_{st} = 0.055$.

Figure 12 Predicted value of η^0 as a function of r for hydrogen added to the oxidizer stream (broken line) and to the fuel stream (solid line) at fixed $T_{st} = 2000$ and $\xi_{st} = 0.055$.
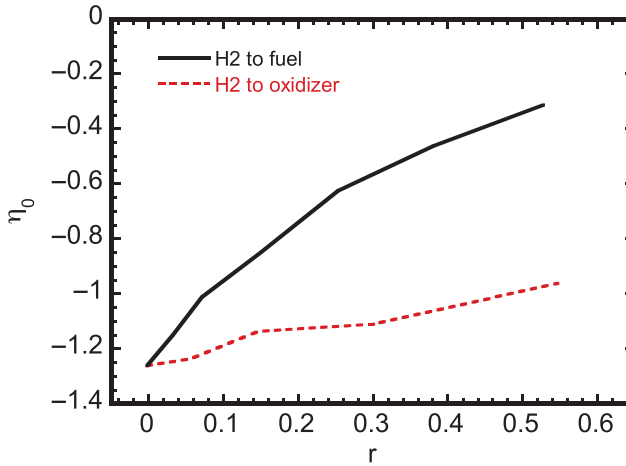
is slightly higher than that when it is added to the oxidizer stream. Figure 12 shows the location of the inner layer as a function of r. It highlights the differences between the flame structure when H_2 is added to the oxidizer stream and that when H_2 is added to the fuel stream. The inner layer is located at $\xi_{st} + \epsilon\eta^0$ as shown by Eq. (26). With increasing r, the value of η^0 increases slightly for hydrogen addition to the oxidizer stream, while there is significant increase in the value of η^0 when H_2 is added to the fuel stream.

With increasing values of r, there is an enhanced consumption of O_2 and H_2 as illustrated by the appearance of r in Eq. (29). The global step IV shows that the enhanced consumption of H_2 and O_2 results in higher levels of radical production. This is the reason for the increase in value of $\chi_{st,q}$. It is noteworthy that addition of H_2 to the oxidizer stream results in further enhancement of consumption of oxygen and hydrogen in the oxidation layer, as illustrated by the appearance of n in Eq. (29). This further increases the value of
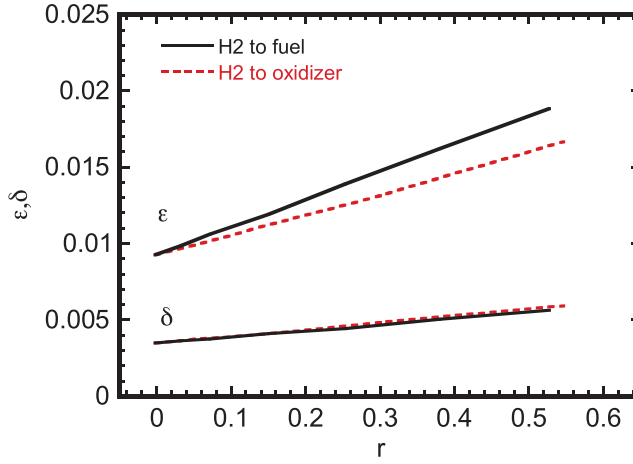
Figure 13 Predicted value of δ and ϵ as a function of r for hydrogen added to the oxidizer stream (broken line) and to the fuel stream (solid line) at fixed $T_{st} = 2000$ and $\xi_{st} = 0.055$.

Figure 14 The value of ω as a function of r for hydrogen added to the oxidizer stream (broken line) and to the fuel stream (solid line) at fixed $T_{st} = 2000$ and $\xi_{st} = 0.055$.
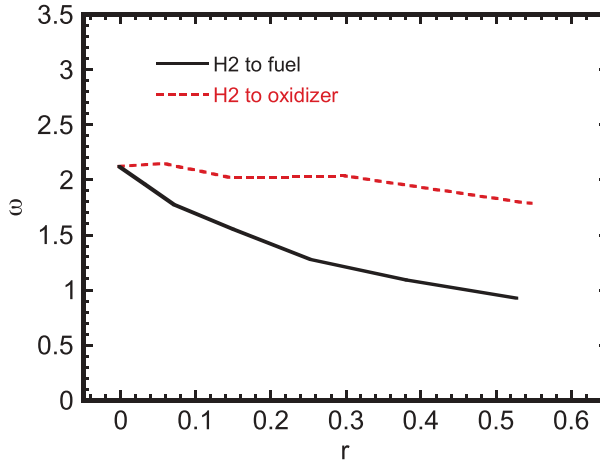
$\chi_{st,q}$. Figure 12 shows that as r increases, the flame moves further toward the fuel boundary when H_2 is added to the fuel stream in comparison to that when it is added to the oxidizer stream. Since ξ_{st} is small, the temperature gradients are steeper in the region $\xi < \xi_{st}$ in comparison with those in the region $\xi > \xi_{st}$. Grudno and Seshadri (1996) have shown that at fixed T_{st}, the scalar dissipation rate at extinction increases with increasing value of ξ_{st}. Thus when H_2 is added to the oxidizer stream, there is further increase in the value of $\chi_{st,q}$ from the enhanced consumption of O_2 and H_2, while for H_2 addition to the fuel stream there is further enhancement in the value of $\chi_{st,q}$ arising from the increase in the value of η^0.

Figure 13 shows the value of the thickness of the inner layer, δ, and the thickness of oxidation layer, ϵ, as a function of r. For all r, the value of δ is less than that of ϵ, and both

are less than unity. This confirms the ordering $\delta \ll \epsilon \ll 1$ employed in the analysis. At a given value of r, the value of δ is the same for hydrogen addition to the fuel stream and hydrogen addition to the oxidizer stream. Thus at the same value of r, the characteristic thickness of the inner layer does not depend on the stream to which H_2 is added. At a given value of r, the value of ε for hydrogen addition to the oxidizer stream is slightly lower than that for hydrogen addition to the fuel stream. Figure 14 shows the value of ω, defined by Eq. (37), decreases with r; the decrease is larger when H_2 is added to the fuel stream. Figures 12, 13, and 14 show that with increasing addition of H_2, the changes in flame structure when H_2 is added to the fuel stream are larger than those when it is added to the oxidizer stream.

CONCLUDING REMARKS

Experimental and computational studies of Niemann et al. (2013) indicate that addition of hydrogen to methane flames at fixed T_{st} and ξ_{st} makes the flame more resistant to strain. The results also appear to suggest that the influence of hydrogen does not depend on the stream to which it is added. The present study confirms some of these findings. The present study shows that there are similarities in the flame structure when H_2 is added to the fuel stream with that when it is added to the oxidizer stream, but there are also important differences. Irrespective of which stream to which H_2 is added, the two-layer structure of the reaction zone, characterized by the oxidation layer and the inner layer, is maintained. The structure of the inner layer is the same and does not depend on the stream to which H_2 is added. When H_2 is added either to the oxidizer stream or to the fuel stream, there is an enhanced consumption of H_2 and O_2. Global step IV shows that consumption of H_2 and O_2 is chain-branching and radicals are produced in this global step. This is the reason for the increase in the values of $\chi_{st,q}$ with addition of H_2. The consumption of O_2 and H_2 is greater when H_2 is added to the oxidizer stream. This enhanced consumption of O_2 is the reason for the lower value of ϵ in Figure 13 for H_2 addition to the oxidizer stream in comparison with H_2 addition to the fuel stream for the same value of r. With H_2 addition to the fuel stream, the flame moves further toward the fuel boundary in comparison to that when it is added to the oxidizer stream at the same value of r. This makes the flame stronger and more resistant to strain as illustrated by the findings of Grudno and Seshadri (1996). Thus there are some differences between the mechanisms of promotion of combustion for H_2 addition to oxidizer stream and H_2 addition to the fuel stream. The two-layer structure for the reaction zone is expected to hold for all values of g, b, m, and n if they are all of the order of unity. To the leading order, the flame structure for g of the order of ϵ, and b of the order of unity, will resemble that of a nonpremixed hydrogen flame for $n = 0$, and m of the order of unity, and that of a counterflow premixed hydrogen flame, similar to that analyzed by Seshadri (1983), for $m = 0$, and n of the order of unity. In the both cases, the influence of methane on the flame structure will be of the order of ϵ and can be included as a perturbation.

ACKNOWLEDGMENT

FUNDING

The research of K. Seshadri, was supported by the U.S. Army Research Office by award # W911NF-12-1-0152, and by the National Science Foundation, award # CBET-1404026. The research of X. S. Bai was supported by the Swedish research funding organizations (CeCOST, KC-FP and VR).

REFERENCES

Bai, X. S., and Seshadri, K. 1999. Rate-ratio asymptotic analysis of non-premixed methane flames. *Combust. Theor. Model.*, **3**, 51–75.

Chelliah, H. K., Trevino, C., and Williams, F. A. 1991. Asymptotic analysis of methane-air diffusion flames. In *Reduced Kinetic Mechanisms and Asymptotic Approximations for Methane-Air Flames*, M. D. Smooke (Ed.), Springer-Verlag, Berlin, Chapter 7, pp. 137–158.

Chelliah, H. K., and Williams, F. A. 1990. Aspects of the structure and extinction of diffusion flames in methane-oxygen-nitrogen systems. *Combust. Flame*, **80**, 17–48.

Grudno, A., and Seshadri, K. 1996. Characteristic residence times of laminar nonpremixed flames at extinction. *Combust. Sci. Technol.*, **112**, 199–210.

Grudno, A., and Seshadri, K. 1998. Rate-ratio asymptotic analysis of inhibition of nonpremixed methane-air flames by CF_3Br. *Combust. Flame*, **112**, 418–437.

Kim, J. S., and Williams, F. A. 1993. Structures of flow and mixture-fraction fields for counterflow diffusion flames with small stoichiometric mixture fractions. *SIAM J. Appl. Math.*, **53**, 1551–1566.

Liñán, A. 1974. The asymptotic structure of counterflow diffusion flames for large activation energies. *Acta Astronaut.*, **1**, 1007–1039.

Niemann, U., Seshadri, K., and Wiliams, F. A. 2013. Effect of addition of a nonequidiffusional reactant to an equidiffusional diffusion flame. *Combust. Theor. Model.*, **17**, 563–576.

Peters, N. 1984. Laminar diffusion flamelet models in non-premixed turbulent combustion. *Prog. Energy Combust. Sci.*, **10**, 319–339.

Peters, N. 1993. Flame calculations with reduced mechanisms—an outline. In *Reduced Kinetic Mechanisms for Applications in Combustion Systems*, N. Peters and B. Rogg (Eds.), Springer-Verlag, Heidelberg, Chapter 1, pp. 1–13.

Seshadri, K. 1983. The asymptotic structure of a counterflow premixed flame for large activation energies. *Int. J. Eng. Sci.*, **21**(2), 103–111.

Seshadri, K. 1996. Multistep asymptotic analyses of flame structures. *Proc. Combust. Inst.*, **26**, 831–846.

Seshadri, K. 2005. Chemical inhibition of nonpremixed methane flames by CF_3Br. *Combust. Sci. Technol.*, **117**, 871–906.

Seshadri, K., and Bai, X. S. 2007. Rate-ratio asymptotic analysis of the structure and extinction of partially premixed flames. *Proc. Combust. Inst.*, **31**, 1181–1188.

Seshadri, K., Bai, X. S., and Williams, F. A. 2013. Rate-ratio asymptotic analysis of the influence of addition of hydrogen on the structure and mechanisms of extinction of nonpremixed methane flame. Presented at the 8th U.S National Combustion Meeting Organized by the Western States Section of the Combustion Institute, The University of Utah, Utah, Paper # 070LT-0325.

Seshadri, K., Bai, X. S., and Williams, F. A. 2014. Rate-ratio asymptotic analysis of the structure and mechanisms of extinction of nonpremixed CH_4/N_2-$O_2/N_2O/N_2$ flames. *Proc. Combust. Inst*. In press. DOI: 10.1016/j.proci.2014.05.002.

Seshadri, K., and Ilincic, N. 1995a. The asymptotic structure of inhibited nonpremixed methane-air flames. *Combust. Flame*, **101**, 271–286.

Seshadri, K., and Ilincic, N. 1995b. The asymptotic structure of nonpremixed methane-air flames with oxidizer leakage of order unity. *Combust. Flame*, **101**, 69–80.

Seshadri, K., and Peters, N. 1988. Asymptotic structure and extinction of methane-air diffusion flames. *Combust. Flame*, **73**, 23–44.

Seshadri, K., and Trevino, C. 1989. The influence of the Lewis numbers of the reactants on the asymptotic structure of counterflow and stagnant diffusion flames. *Combust. Sci. Technol.*, **64**, 243–261.

Seshadri, K., and Williams, F. A. 1994. Reduced chemical systems and their application in turbulent combustion. In *Turbulent Reacting Flows*, P. A. Libby and F. A. Williams (Eds.), Academic Press, San Diego, CA, pp. 153–210.

Smooke, M. D., and Giovangigli, V. 1991. Formulation of the premixed and nonpremixed test problems. In *Reduced Kinetic Mechanisms and Asymptotic Approximations for Methane-Air Flames*, M. D. Smooke (Ed.), Springer Verlag, Berlin, chapter 1, pp. 1–28.

Treviño, A., and Williams, F. A. 1988. Asymptotic analysis of the structure and extinction of methane-air diffusion flames. In *Dynamics of Reactive Systems Part 1: Flames*, A. L. Kuhl, J. R. Bowen, J.-C. Leyer, and A. Borisov (Eds.), American Institute of Aeronautics and Astronautics, Reston, VA, chapter III, pp. 129–165.

Yang, B., and Seshadri, K. 1992. Asymptotic analysis of the structure of nonpremixed methane air flames using reduced chemistry. *Combust. Sci. Technol.*, **88**, 115–132.

Accuracies of laminar counterflow flame experiments

CrossMark

Ulrich Niemann [*], Kalyanasundaram Seshadri, Forman A. Williams

University of California, San Diego, Department of Mechanical and Aerospace Engineering, 9500 Gilman Drive, La Jolla, CA 92093-0411, United States

ABSTRACT

Counterflow configurations are useful for investigating the structures of premixed, non-premixed, and partially premixed flames. Ignition and extinction conditions also are readily measured in this configuration. There is a wide range of different possible designs of apparatus to be used in such measurements. The choices vary from opposing nozzle flows without any flow-smoothing screens to opposing flows through porous plates. It is desirable to select designs that correspond best to the conditions treated in available codes for calculating reacting flows because this facilitates comparisons of experimental and computational results. The most convenient codes to use are for steady laminar flows with one-dimensional scalar fields, and they often impose rotational plug-flow conditions at the boundaries. Accuracies of axisymmetric counterflow flame measurements in experiments intended to conform to these conditions are estimated here for designs of large aspect ratios with straight-duct feed streams that have multiple-screen flow-smoothing exits. Causes of departures from assumptions underlying computational programs are addressed by methods that involve theoretical analysis, experimental measurement, and axisymmetric computation. It is concluded that experimental results would not be expected to differ from predictions made with plug-flow boundary conditions by more than five percent for properly designed counterflow experiments of this straight-duct, multiple-screen type.

© 2014 The Combustion Institute. Published by Elsevier Inc. All rights reserved.

1. Introduction

While there are many reasons for performing combustion experiments, ranging from searching for previously unknown phenomena to improving design, performance, and safety of combustion devices, a prevalent growing motivation is to improve knowledge of underlying transport and chemical-kinetic rate processes, increasing accuracies with which associated parameters are known. Steady counterflows and their variants, such as stagnation flow normal to an inert, impermeable, flat plate or normal to the surface of a solid or liquid-pool fuel, are increasingly becoming the configuration of choice in this quest for greater accuracy. Initial careful work [1,2] – viewed by many as somewhat of a curiosity – for example, a novel way to blow a hole in the center of a flame – the developing realization of the many advantages of the counterflow configuration underlies its emergence.

One advantage is that counterflows enable steady combustion processes to be established away from complicating influences of walls; there is no need to address stabilization-region effects of rim-stabilized or rod-stabilized flames. Another is the inherent stability of the counterflow. The streamline stretching in this configuration helps to dampen disturbances and to prevent some types of combustion instabilities from occurring. It is well suited for experiments at normal atmospheric pressure but also can be adapted for measurements at elevated pressures [3–18], approaching conditions of greater interest in many propulsion and power-production applications. Although planar, two-dimensional counterflow combustors can be (and have been [19,20]) constructed and studied, for most purposes it is simpler and more convenient to select an axisymmetric flow, which makes it unnecessary to consider end effects and which generally exhibits enhanced disturbance-damping abilities.

Use of counterflow combustion experiments to test underlying predictions of these chemically reacting flows requires the availability of numerical methods for solving the sets of partial differential equations that describe the flow. While finite-difference computations can be made for steady, axisymmetric flow [21–27] they become expensive, time-consuming, and often tricky to implement, although important conclusions have recently been drawn from such studies [25–27]. The primary results are the computational demonstrations that, under suitable experimental conditions, with properly chosen boundary conditions one-dimensional codes can be employed with reasonable accuracy [25–27] there being well-defined error metrics on exit-diameter effects [27]. If the problem can be reduced to one of solving only

ordinary differential equations, then the computations become much simpler, and, moreover, in principle they can be performed with greater accuracy. A number of computer codes of this type are now available for solving counterflow combustion problems, such as Chemkin [28], OpenSMOKE [29], Cosilab [30], FlameMaster [31], Cantera [32], and LOGEsoft [33] (formerly DARS [34]). This strongly motivates designing counterflow experiments that obey the conditions required for accurate descriptions in terms of ordinary differential equations. The present discussion addresses the accuracy with which this objective can be obtained.

2. Limitations on the selection of the type of experiment

The first requirement for meeting the preceding objective is to achieve steady, laminar flow. In general, if the Reynolds number is too high, the flow becomes turbulent. For counterflows, the Reynolds number Re may be defined as a representative velocity U of the gas in the approach flow times a characteristic dimension L of the apparatus, divided by a representative kinematic viscosity v of the gas. In a Tsuji burner[1] [36,37] U would be the air flow velocity in the wind tunnel and L the diameter of the porous tube through which the fuel emerges, but in current counterflows U would be an average of the gas exit velocities from the two opposed tubes or ducts, and L the separation distance between the two duct exits. If the duct diameters were smaller than about half the separation distance, then it would be better to use the exit-duct diameter in Re.

The critical value of $Re = UL/v$ above which the counterflow begins to become turbulent actually is not very well established, but because of the stabilizing influences of the configuration it is certainly well above the well-known value of about 2000 for fully developed pipe flow. Corrections for effects of the Reynolds number in laminar flow tend to be of the order of $1/\sqrt{Re}$, and these corrections then can be as small as one percent without there being a tendency for the counterflow to become turbulent. In fact, when there is interest in studying turbulent counterflow combustion experimentally, it is necessary to resort to turbulence-producing grids or perforated plates [38,39], and it is difficult to achieve high-intensity turbulence when that is desired [39].

The axes of the exit ducts in laminar counterflow combustion experiments are placed vertically because if they were not then buoyancy would introduce asymmetry. Unless the temperature of the gas leaving the upper duct is superadiabatic (a condition almost always too hot to achieve), the gas flow between the upper exit and the flame is buoyantly unstable. While a considerable amount of information is available on critical conditions for stability in primarily stagnant layers [40], despite extensive more recent work, such as that which is newly reviewed [41,42], the perturbative influences of the counterflow on the onset of this instability have not been addressed and deserve future study. The stabilizing stretching of the counterflow tends to delay the instability, but stable laminar flow is unattainable in these counterflow experiments at sufficiently high pressures. The relevant stability parameter is the Grashof number, which here is of the order of gL^3/v^2, where g denotes the acceleration of gravity. This parameter, which varies strongly with the length L and the pressure p (being proportional to p^2L^3) is of the order of 1000 in room-temperature air at normal atmospheric pressure if L is 10^{-2} m, which exceeds the critical value for stability [40]. Although the thickness of the layer of adverse density gradient is less than the duct-exit separation distance, it cannot be made appreciably less than 10^{-3} m, whence p as high as 10 atm places most experiments beyond the stability

limit. By decreasing dimensions, employing a design with a nozzle diameter of 6.5×10^{-3} m, useful data have recently be obtained up to 25 atm [17], roughly consistent with the limiting pressure varying as $L^{3/2}$.

In spite of the fact that detailed theoretical analyses of this Grashof-number instability are unavailable (so that this limiting type of $L^{3/2}$ scaling may be inaccurate), the existence of this effect is well documented in recent experimental work [13–16] and likely affected earlier high-pressure NO measurements [7,8], at relatively high Reynolds numbers and relatively low strain rates, where excessively high NO concentrations were recorded on the air side, the upper, unstable side (especially noticeable in the highest-pressure profile [7], well beyond any reasonable NO production region, probably a result of fine-scale upward convective mixing). In a sense, it is fortunate that Earth's gravity level is low enough to allow stable counterflow laminar combustion experiments to be performed routinely at normal atmospheric pressures. Stable experiments at high pressures would require reduced-gravity platforms, such as the Lunar surface, although replacement of nitrogen by helium can improve the stability at high pressures by increasing v [12,15,17].

An additional buoyancy-related complication arises if the exit velocities are too low. The flame then has been observed to bulge upward in the center because of buoyancy (although bulging tendencies in the opposite direction have been observed in some small-scale contoured-nozzle designs). In view of the acceleration of gravity at the Earth's surface, for a duct separation distance on the order of 10^{-2} m, exit velocities greater than 0.3 m/s are needed for the imposed acceleration in the counterflow to be comparable with that of buoyancy (an effective Froude number $U^2/(gL)$ greater than unity). The upward bulging becomes pronounced for screened ducts at exit velocities below this, although it can be reduced by increasing the duct diameters. The curvature associated with the bulge is inconsistent with a one-dimensional calculation; however, the formulation may still apply approximately along the centerline. It is straightforward to include the axial buoyancy term in the ordinary differential equations, and when this is done, for most purposes its influence is found to be negligible; it merely modifies the vertical pressure distribution and the flame location. If, however, L is increased much beyond twice the exit diameter, then buoyant instabilities tend to develop that destroy the one-dimensionality associated with expansion about the centerline. Further discussion of the effect may be found in recent references [12,17], couched in terms of a Richardson number, which is essentially the reciprocal of this Froude number.

Given these buoyancy limitation on exit velocities, counterflow combustion experiments performed on the surface of the Earth are necessarily experiments at high Re. It is impractical to reduce L much below 10^{-2} m, and with U no less than 0.3 m/s, it would be necessary for v to exceed 3×10^{-3} m²/s to have $Re < 1$. This would necessitate producing pressures below 0.03 atm, which would be both difficult and rather uninteresting for most combustion purposes. Low-Re conditions could be achieved at normal atmospheric pressure in space experiments, a fact which motivates the performance of such experiments for the purpose of circumventing the buoyancy limitation, but unfortunately no such experiments yet exist. Current experiments not strongly affected by buoyancy typically correspond to Re between 300 and 3000. In the present situation, then, there is motivation for detailed theoretical consideration of laminar, high-Re limits. Many such investigations have been completed.

It is worth emphasizing that, in numerical computations, there is no particular significance to the fact that in the experiment Re will be large. The entire flow field is calculated, with boundary conditions applied at the exits of the ducts. Numerical difficulties concerning spatial resolution could occur if Re were extremely large,

---

[1] Fuel is injected through the porous walls of a tube whose axis is perpendicular to a uniform air flow in a wind tunnel. This configuration was addressed in the earliest computational work [35].

but a value of 3000 poses no significant computational difficulty. The large Re is taken into account automatically in the calculations, but its large value is helpful in simplifying and thereby clarifying theoretical considerations of designs of experiments and of interpretations of results.

3. Implications of high Reynolds numbers

High-Re flows are characterized by the existence of inviscid regions bounded by narrow viscous regions. In flames, in general, Prandtl and Schmidt numbers are roughly of order unity. Viscous effects may therefore be anticipated to be present where the diffusion and heat-conduction processes that are essential to combustion occur. In counterflow flame experiments, this viscous region is removed from the feed-stream exits where the reactants enter. Inviscid regions therefore are present at the duct exits and extend from there to the flame. Design of counterflow experiments necessitates consideration of these inviscid regions.

In asking what kinds of experiments may be best for comparison with predictions in which ordinary differential equations describe the concentration and temperature fields, it is relevant to begin by determining what kinds of flows can be consistent with such descriptions, with boundary conditions applied over a range of radius r at a constant axial position z. First, it is clear that the temperature, species concentrations, and fluid density must remain constant along the boundary, to avoid violating the underlying assumption right there. The required invariance of the density is a consequence of its appearance in the diffusive terms in the equations. Since pressure decreases as r increases in the flow, this requirement is strictly inconsistent with the ideal-gas equation of state, but since changes in the absolute pressure are of the order of the square of the Mach number, which is extremely small, it is an excellent approximation. Next, it may be observed that for the convective terms in the energy and species conservation equations to be independent of r, the axial velocity u must be a function only of z. From mass conservation, this requires that the radial velocity v be $v = r\,du/dz$, resulting in the vorticity being $(r/2)d^2u/dz^2$.

Two different types of boundary conditions for the velocity field are consistent with this requirement. One, termed plug flow, corresponds to a specified constant inlet velocity u with zero radial velocity, $v = 0$, so that $du/dz = 0$ from mass conservation, which turns out to lead to a quadratic variation of u with z, so that $d^2u/dz^2 \neq 0$, and therefore the flow is rotational. The other type, termed potential flow, has a linear variation of u with z in the inviscid region, so that v increases linearly with r, $d^2u/dz^2 = 0$, and the flow is irrotational, consistent with the existence of a velocity potential. Intermediate boundary conditions can be imposed by effectively considering the boundary to be in the interior of the inviscid region for rotational flow. This is done in some of the available programs by replacing the plug-flow condition of zero radial velocity at the boundary by a specified non-zero linear dependence of the radial velocity on the radial coordinate. When this is done, the vorticity in the inviscid region decreases as the radial gradient of the radial velocity is increased, reaching zero (corresponding to potential flow) at some point (and resulting in vorticity of the opposite sign beyond that point, although that would correspond to a flow that is not attainable physically and so is not done). While the earliest computational programs mainly had only potential-flow boundary conditions [43], codes with plug-flow boundary conditions soon were developed [44,45].[2] Most of the available codes [28–33] now use the plug-flow formulation, often [28,32,33]

with options to specify the inlet velocity gradients to treat intermediate cases, and some [30,31,33] with explicit potential-flow options.

Experimental attempts to produce potential-flow boundary conditions have not been very successful. Feed-system designs with smoothing screens upstream from a nozzle contraction come closest, producing flows that are quite accurately irrotational, but the resulting flow at the nozzle exit does not have du/dz independent of r along a horizontal plane and tends to lie between plug-flow and potential-flow conditions. The flow in the inviscid region is essentially two-dimensional. With such designs, it is best to measure centerline velocity profiles with LDV or PIV techniques and to evaluate du/dz on the centerline (on both sides of the flame) from the measurements, for use in potential-flow calculations. Since, however, the flow field is not exactly that of the ordinary-differential-equation potential-flow numerical codes, differences between experiment and computation may be expected. These differences, which are difficult to quantify, are not likely to be large if results of accurate centerline velocity-field measurements in the vicinity of the exit with the flame present are available [27]. In the absence of such measurements, plug-flow codes can sometimes be employed with acceptable accuracies for some purposes if suitable adjustments are made [17].

Experimental attempts to produce plug-flow boundary conditions typically employ straight ducts without nozzle contractions, inserting screens, honeycombs, or porous plates at the exit of the duct to force uniform, axially directed exit velocities, although a number of (generally poorer) designs, such as flanged ducts, have been tried. Duct exit diameters greater than about half the separation distance are needed to assure plug-flow conditions. These burners are water-cooled to reduce exhaust-gas temperatures for safety reasons, as well as to control reactant temperatures by decreasing their convective heating by hot products and in some cases radiant heat transfer from the flame to the flow-directing surfaces. For these reasons, heat-transfer as well as pressure-drop questions at the duct exits need to be addressed. The measurements are to be compared with computations that employ plug-flow boundary conditions. It is therefore important to evaluate how accurately these conditions can be produced.

The inviscid flow in this counterflow with plug-flow boundary conditions has been analyzed [46]. The theory, invoking the limit of high Re, identifies self-similar conditions under which the axial velocity and all scalar fields depend only on the axial coordinate. The relevant parameter identified in the analysis, the theoretical axial gradient of the axial velocity in the inviscid stream 2 at the stagnation plane when the thickness of the inviscid layer vanishes, is conventionally termed the oxidizer-side strain rate or the effective strain rate [47]. It is

$$a_2 = \frac{2U_2}{L}\left(1 + \frac{U_1\sqrt{\rho_1}}{U_2\sqrt{\rho_2}}\right), \tag{1}$$

where U denotes exit velocities, and ρ the exit-gas densities, of the feed streams. While not given explicitly in the publication [46], it is readily derived therefrom by differentiating the formula given for the axial velocity profile, as is shown in the appendix.

A momentum balance that places the stagnation plane midway between the two exits is $\rho_1 U_1^2 = \rho_2 U_2^2$, a condition usually imposed experimentally. Here the subscripts 1 and 2 would refer to the fuel and oxidizer streams, respectively; in premixed-flame or partially premixed experiments, usually 1 identifies the lower stream and 2 the upper one, which usually contains oxidizer. Because of the presence of the viscous layer, a_2 is not the strain rate on the oxidizer side just outside the flame; indeed, there is arbitrariness in such a definition [47]. Thus, for example, it would not be appropriate to use this a_2 in a potential-flow calculation; in the past, when

---

[2] The Tsuji-burner computations [35] employed potential-flow boundary conditions in the air stream and plug-flow boundary conditions at the fuel inlet.

such calculations were done, strain rates were simply adjusted to best fit the experimental data within the flame.

Fundamentally, Eq. (1) defines a plug-flow parameter. When plug-flow computations are performed, they simply use the experimental values of U, ρ, and L that appear in the equation. Thus, the computations calculate the experimental flow, so long as the configurations agree. Any potential-flow strain rate basically is irrelevant to the most accurate comparisons. The parameter a_2 in the equation merely affords a convenient way to select corresponding experimental and numerical conditions for comparison. In recent discussions, various other terminologies have been used for Eq. (1), such as the overall or global strain rate, which is fine, but sometimes along with such terminology is the false implication that it is insufficient and that experimental determination of a true strain rate is somehow needed for comparisons of results with predictions, while in fact there exists no unique definition of a true strain rate in the counterflow. Many different definitions could be (and have been) introduced because of the axial variation of this quantity. The formula, in fact, is local, rather than global, in the sense that in the analysis it applies only to the stagnation plane.

The analysis [46] neglects displacement effects of the viscous region around the flame. These displacement effects have been analyzed thoroughly [48]. They are quite significant, reducing the effective value of L by thirty percent or more, typically resulting mainly from the oxidizer side, rather than from the fuel side, of a diffusion-flame sheet, since stoichiometric mixture fractions usually are small. The large displacement effects imply that however an oxidizer-side strain rate may be defined, any correct value will be significantly greater than could be estimated from inviscid-flow results with displacement neglected. This is also clear from experiments [47] that employed nozzles with exit boundary conditions intermediate between those of plug-flow and potential flow. These facts, however, have no influence on the comparisons between the experimental and numerical results for experiments that achieve plug-flow exit conditions. The computation automatically includes all of these effects, so that no displacement corrections arise. This enables the experiment to test the values of underlying transport and reaction-rate parameters in the computation.

4. Experimental establishment of computational plug-flow conditions

As previously indicated, screens, honeycombs, or porous plates are used in efforts to obtain plug-flow boundary conditions accurately. Besides necessitating burner cooling and experimental determination of the temperatures of the inlet streams entering the counterflow, these devices introduce exit-flow inhomogeneities that must be small enough to be dissipated before the gas enters the flame. While the inhomogeneities have potentially the finest scales when porous plates are employed, they introduce somewhat higher feed-pressure requirements, and they do not facilitate flow visualization or measurement; little information appears to be available concerning their performance, especially for higher flow velocities, although they may direct exit streams locally over a wide range of directions, thereby resulting in less uniform flow, as has been observed especially in experiments for non-premixed systems. Honeycombs, on the other hand, produce multiple-jet structures which may dissipate too slowly. Screens produce finer scales of exit-velocity fluctuations than honeycombs, achieving rapid dissipation. A typical feed-system design employs straight ducts with three rows of fine wire screens, slightly recessed from the exit. Figure 1 is a representative schematic diagram of a counterflow combustion apparatus of this general type.

In this figure, the upper main duct usually guides the oxidizer stream (2) and the lower main duct the fuel stream (1) in
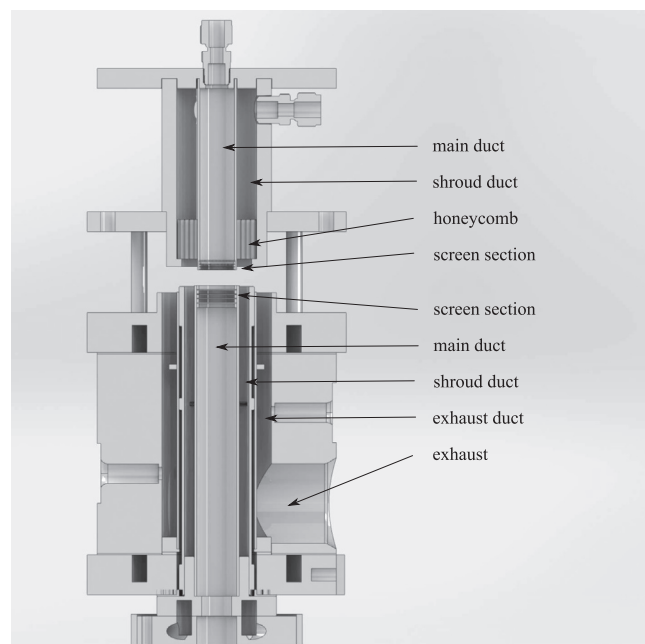

Fig. 1. Schematic drawing of a counterflow apparatus employing screened ducts.

diffusion-flame experiments. The upper and lower shroud ducts, usually carrying inert gas (generally nitrogen), help to minimize any effects of external disturbances on the measurements and to prevent convective heating of the reactants by hot combustion products. The honeycomb illustrated in the upper shroud duct helps to straighten the shroud flow as well as contributing to thermal contact. In the illustrated design, the exhaust and shroud gases are withdrawn downward, through a mild vacuum system capable of handling sufficiently high flow rates. Water cooling, of the exhaust is provided by spray nozzles inserted in the openings shown on either side of the vertical exhaust annular channel. In addition, water cooling of the lower ducts is provided by water circulation through the upper and lower pair of channel openings (seen as dark rectangles in the figure) shown in the lower assembly. The screen temperature (and hence the gas temperature) can readily be kept nearly at the initial feed-stream temperature, never exceeding it by as much as 5 °C, and usually by less than 1 °C, as verified by thermocouple temperature measurements [13]. An exception arises when a hot oxidizer stream is desired for the purpose of determining ignition conditions; in that case, heating elements and insulation are needed for the oxidizer duct, and it is difficult to achieve oxidizer temperatures as high as 1300 K because of materials problems with ducts and screens. Even under those conditions, however, radial variations of the temperature become correspondingly negligible, and in the best designs the heating is provided in the central part of the duct, the ignitions being observed on the centerline, slightly hotter than the periphery. In general, then, in most cases the gases can be assumed to be injected into the counterflow at their initial feed-stream temperature.

In the experiments to be described later, the top duct is a 120 mm-long, straight, constant-diameter tube of inside diameter 22 mm with three equally spaced gauze-type screens placed close to the exit of the duct. Stainless-steel wire screens, 200 mesh per inch, are employed, since that has been found to provide the best performance. This translates into 50 μm wires with 75 μm openings, resulting in an open area of 35%. The screens are kept in place by retaining rings having a 1.5 mm-square cross section, and the tube is notched at the end to provide a flush inner wall, which min-

imizes flow disturbances. In most experiments the screens are recessed 1.5 mm from the duct exit, to avoid the complication of flush mounting. The same screen design is employed for the lower duct in counterflow experiments. The ratio of the inner diameter D of the ducts to the separation distance L between their exits typically lies between 1 and 5, since flow-field assumptions begin to be negated substantially below the lower value,[3] and excessive volume flow rates, increased difficulty of experimental access, and larger radial pressure variations are encountered above the higher value; experience has indicated an optimum value of about 2, which was employed for the measurements reported below. In experiments involving the burning of a solid or liquid fuel in a stagnating oxidizer stream or a premixed combustible gas burning in a stagnation flow, the lower duct is replaced by the solid fuel, a liquid pool, or a flat plate [16,49–52], an optimum ratio of D to the separation distance between the surface and the duct exit then being somewhat less but more than half the value of the ratio for momentum-balanced counterflows, no-slip conditions tending to increase displacement distances slightly.

As a further test of the achievement of plug-flow entrance conditions into a channel flow, attention can be directed to pressure fields. From the analysis [46] of the flow field, it is easy to see that, in the counterflow with plug-flow boundary conditions, the pressure is expressible as a function of z that is determined by conservation of the axial component of momentum, plus a term, determined by conservation of the radial component of momentum, that decreases quadratically with increasing r. This additive term, readily expressible in terms of the velocities and densities at the boundaries, is simply $-2\rho_2 U_2^2 r^2/L^2$ when the aforementioned momentum balance is selected [46]. Proper use of this formula for numerical estimates entails reducing L by the aforementioned displacement thickness of the flame [48]. When this is done, the pressure drop from the stagnation point to the counterflow exit at the edge of the channel for existing experiments [53–55,45,56–71] is calculated to be between 1 Pa and 10 Pa (10^{-4} atm to 10^{-5} atm), increasing with the strain rate. If the feed system is to maintain a constant inlet velocity, independent of r, then this pressure drop must be small compared with the pressure drop across the screens. This pressure requirement will be tested below.

5. Cold-flow experimental and computational methods

Cold-flow experiments can be performed to test some of the requirements discussed above. This is especially true because the fuel flow at the screen exits of a screened-duct types of apparatus typically is cold flow. In the present work, the pressure drop across the screens under cold-flow conditions was measured as a function of the bulk flow velocity, and velocity fields were measured by particle-image velocimetry (PIV). Flow fields were established with dry air at atmospheric conditions, and fluid flows were controlled with computer-regulated mass-flow controllers that are calibrated with a high-precision wet-test meter to volumetric-flow-rate accuracies better than 0.5%. The pressure drops across the screens were measured by use of a differential pressure gauge with pressure taps upstream and downstream from the screens. For the PIV measurements, the air was seeded with oil droplets generated from an atomizer (TSI), producing a mean droplet size of 0.8 μm. The imaging system consisted of a dual-head Nd:YAG laser (New Wave Research) coupled with a CCD camera (Lavision) with a resolution of 1392 × 1024 pixels, equipped with a 60 mm macro lens (Canon).

Pairs of thin laser sheets were pulsed through the axis of symmetry of the flow field at delay times of 100–500 μs, depending on the estimated flow velocities, such that the bulk particle movement is about 25% of the interrogation window size. Velocity vectors were obtained based on 32 × 32 pixels (0.42 mm × 0.42 mm) interrogation windows with 50% grid overlapping in a standard fast Fourier transform (FFT) cross-correlation analysis. Averages of 20 image pairs were taken at a frequency of 10 fps. The resulting accuracy of the flow velocities is on the order of 0.03 m/s. Laser scattering from the screen at the duct exit may as much as double the errors of the exit velocities, compared to the rest of the flow field.

For comparison with the measured velocity field, two-dimensional axisymmetric computations were performed with Star-CCM+, a commercial computational fluid dynamics (CFD) package for a compressible ideal gas [72]. Shroud flows with exit velocities equal to main-flow velocities were included in the models as well, but they were found to exert a negligible influence on the main flow. Structured meshes of quadrilateral cells were generated to approximate the geometric domain. To capture boundary-layer effects, adaptive-mesh refinements were enabled close to walls and flow inlets. Results were confirmed to be grid-insensitive. In addition, unsteady computations were preformed to assure that the steady-state results reported were approached stably. The screens were treated as infinitesimally thin porous baffles, across which the measured relationship between the flow rate and the pressure drop was applied to determine the resistance coefficients. Boundary conditions of uniform entrance flow were applied to the top end of the top duct of Fig. 1, with no-slip conditions at the walls and pressure-outlet conditions at the radial boundaries.

For the screened ducts, two different configurations were studied both experimentally an computationally, namely the counterflow with symmetric momentum balance and the stagnation flow with a flat plate replacing the lower duct of Fig. 1.

6. Experimental and numerical results for screened ducts

The results of the pressure measurements are shown in Fig. 2. These measurements were made at bulk inlet flow velocities (volume flow rates divided by duct exit areas) between 0.25 and 2.00 m/s, which cover the range of typical experiments, corresponding to strain rates calculated from Eq. (1) of around 100–1500 s^{-1}. It is seen that, over this range, the pressure drop lies between 20 Pa and 200 Pa, a range between 2 and 200 times the
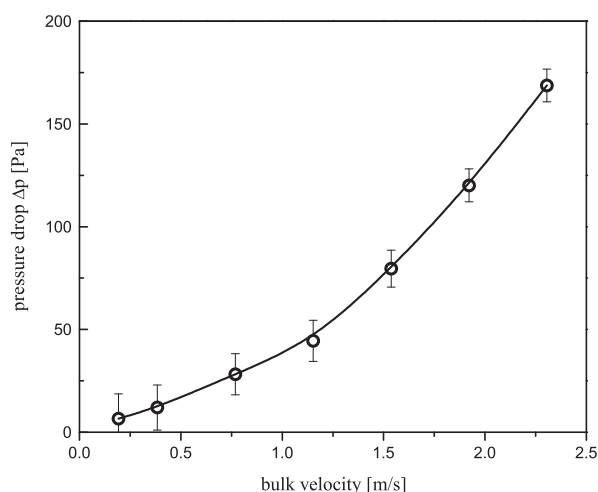

Fig. 2. The measured bulk-velocity dependence of the pressure drop across the screen arrangement.

---

[3] For some purposes, such as comparisons of measured and calculated species profiles, useful results can be obtained beyond this limit [17], although comparisons of flame-extinction conditions, for example, are not recommended without corrections for radial gradients of radial velocities.

range of the radial pressure drop indicated above. Since the radial pressure drop varies with the strain rate in a manner similar to that in Fig. 2, the pressure drop through the screens is consistently a little over 20 times the radial pressure drop, which corresponds to a variation of the inlet velocity of about 10%. Figure 2 thus indicates that the radial variations of the inlet velocities can conservatively be estimated to be no greater than ten percent over the entire exit areas of the ducts. Measurement of velocity fields provide finer tests for achievement of plug-flow conditions.

Representative results of PIV measurements are shown in Fig. 3. In this figure, the reduced data, giving vector diagrams of the directions and magnitudes of the velocities are shown only on the left, so that the raw PIV images can be seen more clearly on the right. Color coding is added to help to clarify velocity magnitudes. The flow is quite symmetric, as would have been seen if the vector diagrams had been extended to the right. In addition, repeated time-resolved images of this kind provide evidence that there are no fluctuations of the stagnation plane or of the streamlines, thereby indicating rapid damping of any screen-induced inhomogeneities. The magnitudes and directions of the velocity vectors are entirely consistent with plug-flow conditions, indicating uniform, axially directed flow through the screens and a fixed stagnation point, with velocities increasing radially away from the stagnation point. Particle-streak photos obtained in a stagnation flow over a burning liquid pool [49] similarly indicated good achievement of plug-flow conditions with a screened duct, in that case in the presence of a flame.

While these general agreements are suggestive, more stringent tests can be made from detailed PIV and CFD results. Figure 4 compares measured and calculated radial profiles of axial velocity at the screen exit for three different flow rates. The normalizing velocity U in this figure is taken to be the centerline velocity at the screen exit calculated by the CFD, which exceeds the bulk inlet velocity by about 2–3%. Aside from the thin near-wall region where overshoots, increasing with increasing flow rate, are seen to occur prior to reaching the boundary layer, the profiles are quite flat. While the experimental overshoot percentage at the highest flow rate approaches twice that calculated, in general the PIV and CFD results are in good agreement. The differences are attributable to inaccuracies in the porous-baffle approximation for the screens near the walls since the CFD resolution was verified to be accurate. The central half of the duct is the most important region for comparing experimental and computational results, and over this
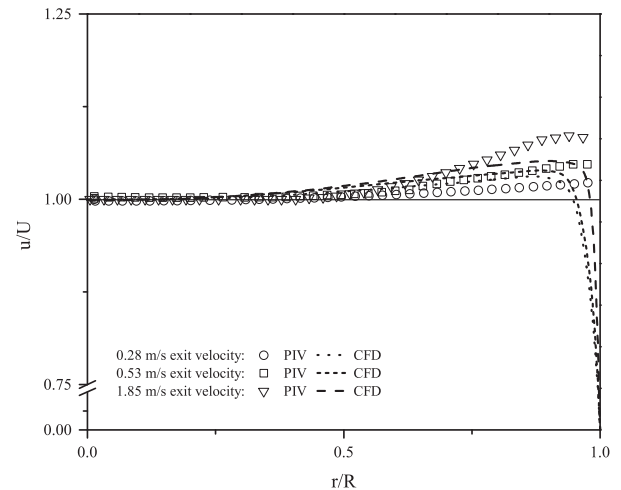

Fig. 4. The inlet radial profiles of axial velocity for a screened duct in an opposed-flow configuration for three different inlet velocities with a separation distance of half the duct diameter.

region the exit velocity variations are less than 1%, both experimentally and computationally.

Figure 5 shows centerline axial velocity profiles for three different flow rates. In this figure, the experimental results are compared with results for plug-flow computations made with one of the standard codes employed in combustion [28], and the analytical result [46], in the inviscid flow with momentum balance, given by

$$\frac{u}{U} = 1 - 4\frac{z^2}{L^2} \qquad 0 \leqslant \frac{z}{L} \leqslant 0.5. \tag{2}$$

The agreements under these cold-flow conditions are excellent, even at the highest flow rate, where the differences would be the greatest. These one-dimensional computations and the analytical solution from Eq. (2) also agree with the CFD results - so well that different curves could not be distinguished for them. The very small deviations that are seen lie within the experimental accuracy. With all curves chosen to reach zero at $z/L = 0.5$, all differences are less than 3%. irrespective of whether bulk velocities or centerline exit CFD velocities are employed.

As a further test, similar measurements and computations were made for a stagnation-flow experiment in which the lower duct in
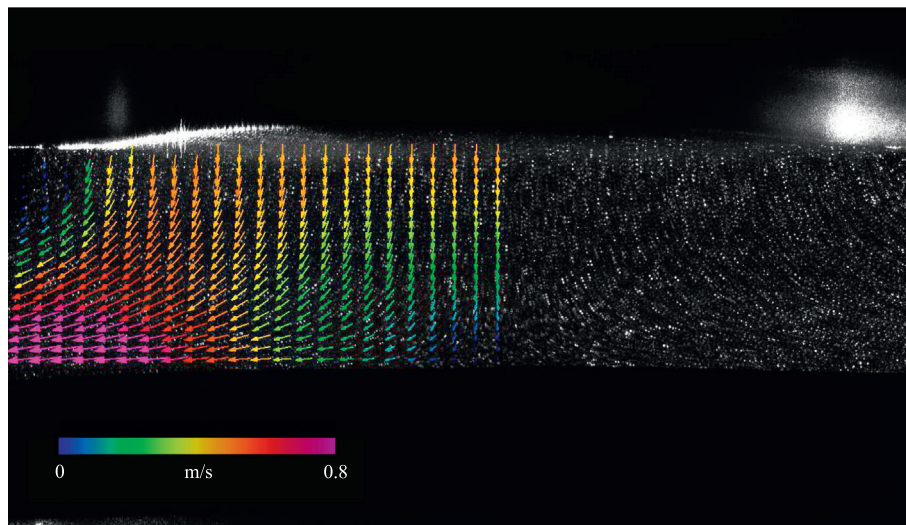

Fig. 3. PIV image with overlayed velocity vector map for an opposed flow from screened ducts with 10 mm separation distance and 0.5 m/s bulk inlet velocities.
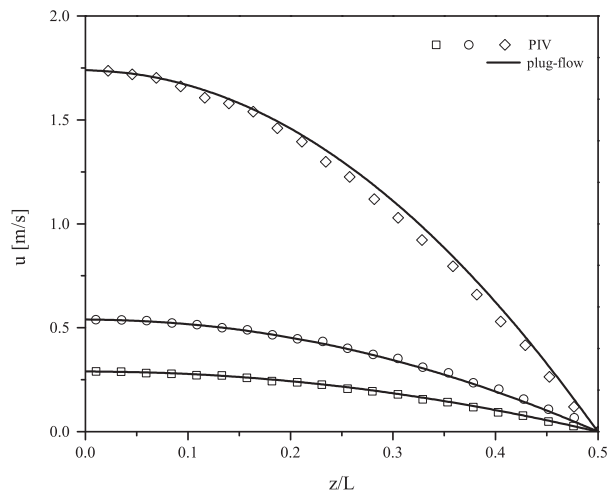
Fig. 5. The centerline axial velocity profiles of a screened duct in an opposed-flow configuration for three different inlet velocities with a separation distance of half the duct diameter.

Fig. 7. The axial velocity profiles for the stagnation-flow configuration from a screened duct for five different inlet velocities with a separation distance of half the duct diameter.

Fig. 1 is replaced by a flat plate. Figure 6 compares exit velocity profiles at four different flow rates for this case. In this configuration, the CFD screen-exit centerline normalization velocity U exceeds the bulk velocity by less than 2%. The PIV and CFD agreements here are similar to those in Fig. 4, although now the CFD predicts somewhat less variation near the wall. As in Fig. 4, agreements with plug-flow assumptions are better than 1% over the central half of the duct, and the maximum experimental overshoot near the edge is less than 8%. From Fig. 7, the analog of Fig. 5 for this flow, now for five flow rates, conclusions identical to those indicated for Fig. 5 can be drawn, with all differences now less than 2%.

Quantitative assessments of uncertainties in axial centerline duct-exit velocities can be made from these results. The bulk inlet velocity is readily calculated from the measured flow rates and the inner diameter of the duct. This calculated value can be compared with the values obtained from both PIV and CFD. The latter two results are both larger than the calculated value, by as much as 3% for the opposed flow and 2% for the stagnation flow, as can be seen in Fig. 8, where the PIV error bars identify the maximum errors possible (greater than the standard deviation). These then
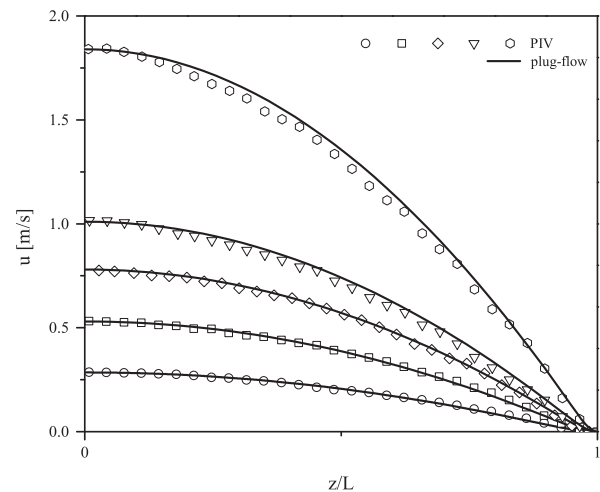
are the uncertainties to be expected in the combustion experiments.

The radial component of velocity provides another basis for assessing accuracies of plug-flow calculations. Figure 9 shows two representative comparisons of this, one for the opposed flow at an axial position 2.5 mm from the duct exit (about half way to the stagnation plane), and the other for the stagnation flow one quarter of the way from the duct exit to the stagnation plate. Both show excellent agreement between PIV and CFD results, as well as indicating that the standard code accurately predicts the radial variations of the radial component of velocity at least over the inner 80% of the duct radius. The radial components of velocity at the screen exit location were too small to be measured by PIV, but they could be calculated by CFD. The results, shown in Fig. 10, indicate that they tend to scale with the axial bulk exit velocity U, fluctuating about zero by amounts of the order of 2% of that velocity over the inner 60% of the duct radius, then increase to as much as 10% of that velocity at the duct wall. The other curves in this figure pertain to the following section. These results, however, support the uncertainty estimate of about 2%, obtained in Fig. 8, and they indicate that variations in velocity gradients at
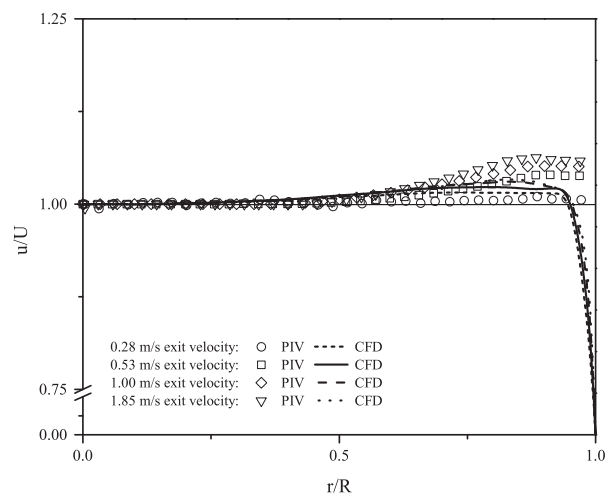

Fig. 6. The radial profiles of axial velocity at the inlet for the stagnation-flow configuration from a screened duct for four different inlet velocities with a separation distance of half the duct diameter.
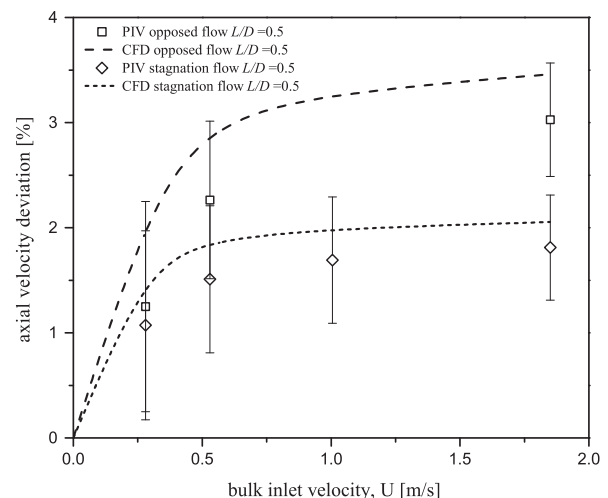

Fig. 8. The bulk-inlet-velocity dependence of the deviation of the centerline exit axial velocity from the bulk velocity, as measured and obtained from computations.
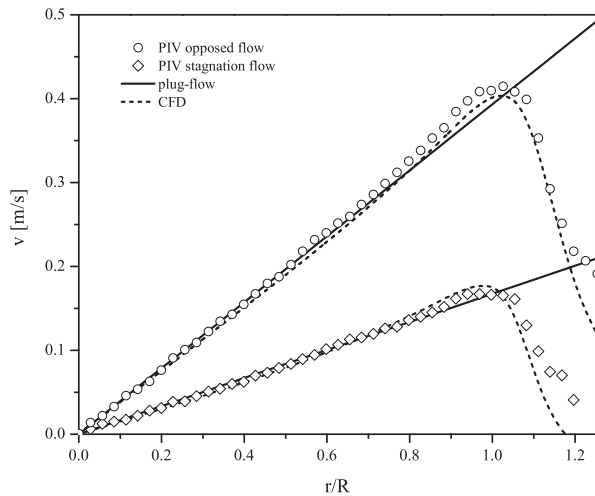
Fig. 9. The radial velocity measured 2.5 mm from the nozzle exit, in comparison with the CFD and plug-flow predictions.

Fig. 11. Cross-sectional view of the contoured nozzle employed in this study.

the screen exits are less than 4 s⁻¹, that is, at most a few percent of the gradients imposed in combustion experiments.

The CFD code also was employed to explore influences of variations in duct-exit designs, such as recessing the screens. Recesses smaller than 10% of the duct diameter were found to have minimal effects on the centerline exit axial velocity at the screen, although they did enhance the boundary-layer overshoot at the wall. This was also consistent with some exploratory PIV measurements.

7. Characteristics of a screen-free nozzle design

Because of the continuing interest in the use of screen-free nozzles instead of screened ducts [17,26,27,52,73–77], a design of this type was constructed and tested in cold flow in a stagnation-flow configuration. Wind-tunnel design information [78] and CFD were employed in the design, which is illustrated in Fig. 11. To facilitate comparisons with the screened-duct measurements, comparable dimensions were chosen, rather than the smaller sizes often employed in combustion experiments. Over the length of 150 mm, the inner diameter of the tube contracts from 120 mm
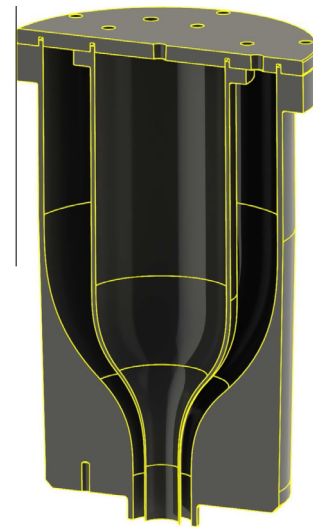
to 29.8 mm, giving an area ratio greater than 16, comparable with the ratios, up to around 24, commonly used in the combustion experiments. A similar contraction ratio was selected for the shroud stream illustrated in the figure, in which the calculated bulk flow velocity was adjusted to match that of the main nozzle. Both CFD and PIV verified achievement of the desired top-hat exit velocity profile in the free-jet configuration.

Measured and computed radial profiles of the axial velocity at the nozzle exit are shown in Fig. 12 for two different separation distances at two different bulk-flow exit velocities. The figure indicates that increasing the exit velocity has a smaller influence on the profiles than decreasing the separation distance, which was anticipated, in view of the fact that although these two changes are expected to exert similar influence on pressure fields around the stagnation point, the pressure changes being of the order U^2/L^2, with the velocity change these effects are offset somewhat by an increase in the pressure drop through the contoured section [74,76]. Thus the velocity change preferentially enhances the velocity overshoot. The PIV and CFD results are in excellent agreement throughout these flows. While the desired top-hat velocity profile is approached near the centerline for sufficiently low exit
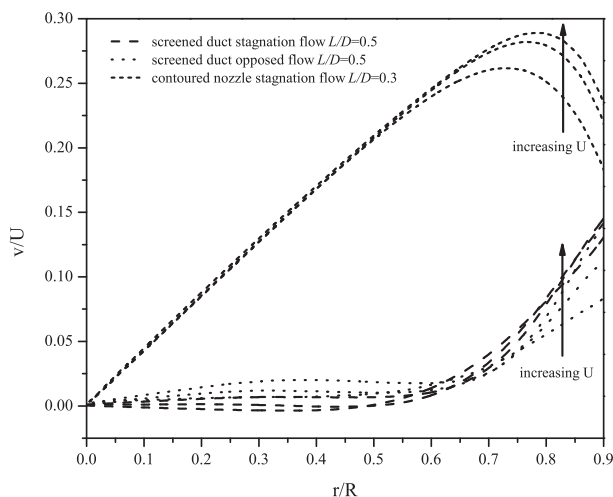

Fig. 10. CFD predictions of the radial velocity at the inlet as a function of the normalized radial distance from the centerline for a screened duct and a contoured nozzle.
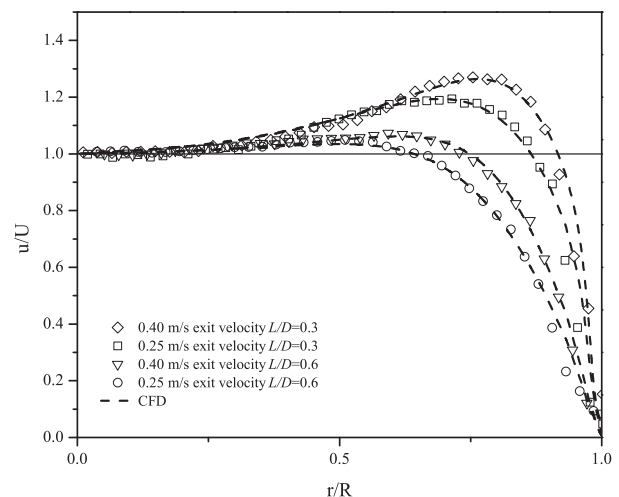

Fig. 12. The radial profiles of axial velocity from the contoured nozzle for two inlet velocities and two separation distances (0.3 and 0.6 times the nozzle-outlet inner diameter).
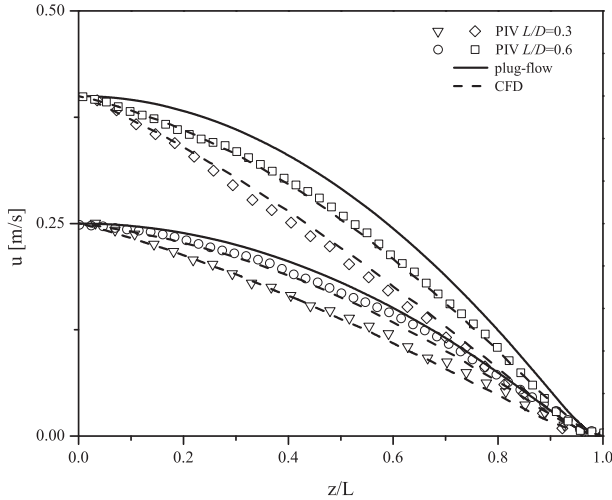
Fig. 13. The axial velocity profiles of stagnation flows from a contoured nozzle for two respective cases of inlet centerline velocity and separation distance normalized by the separation distance for $L/D = 0.3, 0.6$.

velocities, overshoots always become evident, beginning to develop at radii less than half the inner radius of the nozzle, and they exceed those in Fig. 5, being 4–6% at the larger separation distance and 18–25% at the closer distance.

More importantly, some curvature is always evident at the centerline in Fig. 12, reflecting the fact that the radial gradient of the radial velocity component cannot be ignored there, as is seen in the corresponding CFD results shown in Fig. 10. This, also identified in the literature [52,74], emphasizes the desirability of determining radial velocity gradients and employing them in the code options [28] when analyzing combustion experiments for nozzle-type designs. That desirability is underscored in Fig. 13, which shows axial velocity profiles for the cases of Fig. 12, again demonstrating good agreement between PIV and CFD results. The solid curves, obtained employing plug-flow boundary conditions in the code [28], clearly disagree with the measurements, which suggest that potential-flow boundary conditions would be much better at the larger separation distance. Employing the code with proper account taken of the radial gradient of the radial velocity would improve the agreement greatly, irrespective of where in the stagnation region the boundary conditions are applied[52,74,77]. Comparisons of such computational results with experiments can be helpful in attempting to extrapolate results to zero strain rates [25,79,80].

8. Conclusions

From these considerations it may be concluded that both screened ducts and contoured nozzles offer useful tools for investigating combustion processes, to test knowledge of associated transport-property and chemical-kinetic parameters by comparing experimental results with predictions of computer programs based on assumptions of one-dimensional temperature and concentration fields. In such comparisons, it is best to account for the radial gradient of the radial component of the velocity when contoured nozzles are employed, but plug-flow boundary conditions apply with good accuracy for screened ducts. The departures from plug-flow conditions in screened-duct devices generally are too small to be determined accurately enough to justify use of any other boundary condition at the screen exits. Accuracies are such that errors are less than 5% in well-designed screened-duct experiments.

Appendix A

Consider steady, axisymmetric flow of two jets toward a stagnation plane from boundaries that are separated by a distance L. The axial coordinate, ζ, and the radial coordinate, ξ, are nondimensionalized with respect to L. The radial component of the flow velocity is v_ξ, while the axial component of the flow velocity is v_ζ. At the boundary $\zeta = 1$, the magnitude of the injection velocity, the density, and the temperature of the fluid are represented by U_2, ρ_2 and T_2, respectively, and at the boundary $\zeta = 0$, by U_1, ρ_1 and T_1 respectively. The Reynold's numbers $Re_2 = U_2 \rho_2 L/\mu_2$, and $Re_1 = U_1 \rho_1 L/\mu_1$ appear where μ_2 and μ_1 are coefficients of viscosity of the fluid at $\zeta = 1$ and $\zeta = 0$, respectively. There exist solutions for which $v_\xi = \xi U(\zeta)$ [81,50]. All flow quantities, except the pressure, p, are functions of the axial co-ordinate only [50]. For low speed flows, it can be shown from the radial component of the equation of motion that $p = P(\zeta) - \xi^2 Q(\zeta)$. It follows from the axial component of the equation of motion that Q is a constant. Quantities are nondimensionalized with respect to their values at $\zeta = 1$. Thus $T/T_2 = \rho_2/\rho = \mu/\mu_2 = \theta(\zeta)$, where T is the temperature [50].

Of interest here is the limit of large Re_2. If Re_1 is also large and of the order of Re_2, then two inviscid regions will develop on either side of the stagnation plane that is presumed to be at $\zeta = \zeta_s$. A thin viscous layer is established at ζ_s [50,81]. In the inviscid regions, $\theta = \theta_0 =$ constant [50]. In the region $0 < \zeta < \zeta_s, \theta = \theta_1 = \rho_2/\rho_1$, while in the region $\zeta_s < \zeta < 1, \theta = 1$. Thus for $\rho_2 \neq \rho_1$, the value of θ is discontinuous across the stagnation plane. The present analysis is restricted to the hydrodynamic flow field in the inviscid regions.

It follows from the equation of conservation of mass that $U/U_2 - \theta_0 f'/2 = 0$, where $f = -v_\zeta/(\theta_0 U_2)$, and primes denote differentiation with respect to ζ [50]. The radial component of the equation of motion is [50]

$$(f')^2 - 2ff'' - K/\theta_0 = 0. \tag{A.1}$$

Here $K = 8Q/\left(\rho_2 U_2^2\right)$. Plug flow boundary conditions are presumed to apply. Hence at $\zeta = 0$,

$$f' = 0, \quad f = f_1 = -\rho_1 U_1/(\rho_2 U_2). \tag{A.2}$$

At $\zeta = 1$, the boundary conditions are

$$f' = 0, \quad f = 1. \tag{A.3}$$

The solution to Eq. (A.1) that satisfies the boundary conditions Eqs. (A.2) and (A.3) are

$$\begin{aligned} f &= f_1 - K\zeta^2/(4\theta_1 f_1), \quad 0 < \zeta < \zeta_s, \\ f &= 1 - K(1-\zeta)^2/4, \quad \zeta_s < \zeta < 1. \end{aligned} \tag{A.4}$$

At the stagnation plane, $f = 0$. Thus the axial component of the flow velocity is continuous across the stagnation plane. It follows from Eq. (A.4) that $K/4 = (1 - \zeta_s)^{-2} = \theta_1 f_1^2/\zeta_s^2$, and

$$\zeta_s = [1 + U_2\sqrt{\rho_2}/(U_1\sqrt{\rho_1})]^{-1}. \tag{A.5}$$

The radial component of the flow velocity, v_ξ, and the axial gradient of the axial component of the flow velocity, represented by $a = (1/L)|dv_\zeta/d\zeta|$, are proportional to $\theta_0 U_2 f'$. Eq. (A.4) reveals that the value of these quantities change with changes in ζ, and are discontinuous across the stagnation plane. The value of a evaluated at $\zeta = \zeta_s$ in the region $\zeta_s < \zeta < 1$ is represented by a_2. An expression for a_2 obtained by differentiating the second relation in Eq. (A.4) is

$$a_2 = \frac{2U_2}{L}\left(1 + \frac{U_1\sqrt{\rho_1}}{U_2\sqrt{\rho_2}}\right), \tag{A.6}$$

where use is made of Eq. (A.5). It can be verified that $a_1 = a_2\sqrt{(\rho_2/\rho_1)}$, where a_1 is the value of a evaluated at $\zeta = \zeta_s$ in the region $0 < \zeta < \zeta_s$.

References

[1] J.A.E. Potter, J.N. Butler, ARS J. 29 (1959) 54–56.
[2] J.A.E. Potter, S. Heimel, J.N. Butler, Proc. Combust. Inst. 8 (1962) 1027–1034.
[3] J. Sato, Combust. Sci. Technol. 75 (1991) 103–113.
[4] D.X. Du, H. Wang, C.K. Law, Combust. Flame 113 (1998) 264–270.
[5] C.J. Sung, B. Li, H. Wang, C.K. Law, Proc. Combust. Inst. 27 (1998) 1523–1529.
[6] H. Bohm, F. Lacas, Proc. Combust. Inst. 28 (2000) 2627–2634.
[7] R.V. Ravikrishna, D.D. Thomsen, N.M. Laurendeau, Combust. Sci. Technol. 157 (2000) 243–261.
[8] R.V. Ravikrishna, S.V. Naik, C.S. Cooper, N.M. Laurendeau, Combust. Sci. Technol. 176 (2004) 1–21.
[9] S.V. Naik, N.M. Laurendeau, Combust. Sci. Technol. 176 (2004) 1809–1853.
[10] K. Maruta, K. Abe, S. Hasegawa, S. Maruyama, J. Sato, Proc. Combust. Inst. 31 (2007) 1223–1230.
[11] H. Zhang, R. Fan, S. Wang, X. Tran, K. Xu, S. Wan, F.N. Egolfopoulos, Proc. Combust. Inst. 33 (2011) 1171–1178.
[12] L. Figura, A. Gomez, Combust. Flame 159 (2012) 142–150.
[13] U. Niemann, Experimental and Computational Studies of the Combustion of Classical and Alternative Fuels, Ph.D. thesis, 2013.
[14] U. Niemann, K. Seshadri, F. Williams, Proc. Combust. Inst. 34 (2013) 881–886.
[15] U. Niemann, K. Seshadri, F.A. Williams, Combust. Flame 161 (2014) 138–146.
[16] R. Gehmlich, A. Kuo, K. Seshadri, Proc. Combust. Inst. (2014), http://dx.doi.org/10.1016/j.proci.2014.05.111 (in press).
[17] L. Figura, A. Gomez, Combust. Flame 161 (2014) 1587–1603.
[18] L. Figura, F. Carbone, A. Gomez, Proc. Combust. Inst. (2014), http://dx.doi.org/10.1016/j.proci.2014.05.028 (in press).
[19] M.L. Shay, P.D. Ronney, Combust. Flame 112 (1998) 171–180.
[20] J.B. Liu, P.D. Ronney, Combust. Sci. Technol. 144 (1999) 21–45.
[21] A. Ern, C.C. Douglas, M.D. Smooke, Int. J. Supercomput. Appl. 9 (1995) 167–186.
[22] C. Frouzakis, J. Lee, A. Tomboulides, K. Boulouchos, Symp. (Int.) Combust. 27 (1998) 571–577. Twenty-Seventh Sysposium (International) on Combustion Volume One.
[23] M.D. Smooke, C.S. McEnally, L.D. Pfefferle, R.J. Hall, M.B. Colket, Combust. Flame 117 (1999) 117–139.
[24] M. Smooke, M.B. Long, B.C. Connelly, M. Colket, R.J. Hall, Combust. Flame 143 (2005) 613–628.
[25] V. Mittal, H. Pitsch, F. Egolfopoulos, Combust. Theor. Model. 16 (2012) 419–433.
[26] N. Bouvet, D. Davidenko, C. Chauveau, L. Pillier, Y. Yoon, Combust. Flame 161 (2014) 438–452.
[27] A. Johnson, R.F. VanDine, G. Esposito, H. Chelliah, Combust. Sci. Technol. (submitted for publication) (2014).
[28] CHEMKIN-PRO v.15112, Reaction Design, 2012.
[29] A. Cuoci, A. Frassoldati, T. Faravelli, E. Ranzi, Combust. Sci. Technol. 180 (2008) 767–784.
[30] Cosilab collection, version 2.0.7, www.rotexo.com, 2007.
[31] H. Pitsch, Entwicklung eines Programmpaketes zur Berechnung eindimensionaler Flammen am Beispiel einer Gegenstromdiffusionsflamme, Master's thesis, RWTH Aachen, 1993.
[32] Cantera: An object-oriented software toolkit for chemical kinetics, thermodynamics, and transport processes, <www.cantera.org>, 2013.
[33] LOGEsoft, www.loge.se, 2014.
[34] DARS-Basic, CD-adapco, 2014.
[35] G. Dixon-Lewis, T. David, P.H. Gaskell, S. Fukutani, H. Jinno, J.A. Miller, R.J. Kee, M.D. Smooke, N. Peters, E. Effelsberg, J. Warnatz, F. Behrendt, Proc. Combust. Inst. 20 (1984) 1893–1904.

[36] H. Tsuji, I. Yamaoka, Proc. Combust. Inst. 11 (1967) 979–984.
[37] H. Tsuji, Prog. Energy Combust. Sci. 8 (1982) 93–119.
[38] S.C. Li, P.A. Libby, F.A. Williams, Proc. Combust. Inst. 25 (1995) 1207–1214.
[39] B. Coriton, J.H. Frank, A.G. Hsu, M.D. Smooke, A. Gomez, Proc. Combust. Inst. 33 (2011) 1647–1654.
[40] B. Gebhart, Annu. Rev. Fluid Mech. 5 (1973) 213–246.
[41] R. Govindarajan, K.C. Sahu, Annu. Rev. Fluid Mech. 46 (2014) 331–353.
[42] P. Luchini, A. Bottaro, Annu. Rev. Fluid Mech. 46 (2014) 493–517.
[43] V. Giovangigli, M.D. Smooke, Combust. Sci. Technol. 53 (1987) 23–49.
[44] R.J. Kee, J.A. Miller, G.H. Evans, G. Dixon-Lewis, Symp. (Int.) Combust. 22 (1989) 1479–1494.
[45] M.D. Smooke, J. Crumb, K. Seshadri, V. Giovangigli, Proc. Combust. Inst. 23 (1990) 463–470.
[46] K. Seshadri, F.A. Williams, Int. J. Heat Mass Transf. 21 (1978) 251–253.
[47] H.K. Chelliah, C.K. Law, T. Ueda, M.D. Smooke, F.A. Williams, Proc. Combust. Inst. 23 (1990) 503–511.
[48] J.S. Kim, P.A. Libby, F.A. Williams, Combust. Sci. Technol. 87 (1992) 1–25.
[49] J.H. Kent, F.A. Williams, Proc. Combust. Inst. 15 (1975) 315–325.
[50] K. Seshadri, F.A. Williams, J. Polym. Sci.: Polym. Chem. Ed. 16 (1978) 1755–1778.
[51] S.H. Sohrab, F.A. Williams, J. Polym. Sci.: Polym. Chem. Ed. 19 (1981) 2955–2976.
[52] J.M. Bergthorson, S.D. Salusbury, P.E. Dimotakis, J. Fluid Mech. 681 (2011) 340–369.
[53] I.K. Puri, K. Seshadri, Combust. Flame 65 (1986) 137–150.
[54] I.K. Puri, K. Seshadri, Combust. Sci. Technol. 53 (1987) 55–65.
[55] I.K. Puri, K. Seshadri, M.D. Smooke, D.E. Keyes, Combust. Sci. Technol. 56 (1987) 1–22.
[56] D. Trees, T.M. Brown, K. Seshadri, M.D. Smooke, G. Balakrishnan, R. Pitz, V. Giovangigli, S.P. Nandula, Combust. Sci. Technol. 104 (1995) 427–439.
[57] R. Seiser, L. Truett, D. Trees, K. Seshadri, Proc. Combust. Inst. 27 (1998) 649–657.
[58] L. Truett, H. Thermann, D. Trees, K. Seshadri, J. Yuan, L. Wells, P. Marshall, Proc. Combust. Inst. 27 (1998) 2741–2748.
[59] R. Seiser, H. Pitsch, K. Seshadri, W.J. Pitz, H.J. Curran, Proc. Combust. Inst. 28 (2000) 2029–2037.
[60] S. Humer, R. Seiser, K. Seshadri, Proc. Combust. Inst. 29 (2002) 1597–1604.
[61] R. Seiser, K. Seshadri, Proc. Combust. Inst. 30 (2005) 407–414.
[62] S. Humer, A. Frassoldati, S. Granata, T. Faravelli, E. Ranzi, R. Seiser, K. Seshadri, Proc. Combust. Inst. 31 (2007) 393–400.
[63] S. Honnet, K. Seshadri, U. Niemann, N. Peters, Proc. Combust. Inst. 32 (2009) 485–492.
[64] T. Bieleveld, A. Frassoldati, A. Cuoci, T. Faravelli, E. Ranzi, U. Niemann, K. Seshadri, Proc. Combust. Inst. 32 (2009) 493–500.
[65] K. Seshadri, T. Lu, O. Herbinet, S. Humer, U. Niemann, W.J. Pitz, R. Seiser, C.K. Law, Proc. Combust. Inst. 32 (2009) 1067–1074.
[66] U. Niemann, R. Seiser, K. Seshadri, Combust. Theor. Model. 14 (2010) 875–891.
[67] A. Frassoldati, A. Cuoci, T. Faravelli, U. Niemann, E. Ranzi, R. Seiser, R. Cattolica, K. Seshadri, Combust. Flame 157 (2010) 2–16.
[68] R. Grana, A. Frassoldati, T. Faravelli, U. Niemann, E. Ranzi, R. Seiser, R. Cattolica, K. Seshadri, Combust. Flame 157 (2010) 2137–2154.
[69] H. S, R. Seiser, K. Seshadri, J. Propul. Power 27 (2011) 847–855.
[70] K. Seshadri, A. Frassoldati, A. Cuoci, T. Faravelli, U. Niemann, P. Weydert, E. Ranzi, Combust. Theor. Model. 15 (2011) 569–583.
[71] R. Seiser, U. Niemann, K. Seshadri, Proc. Combust. Inst. 33 (2011) 1045–1052.
[72] STAR-CCM+ v8.0, CD-adapco, 2014.
[73] J. Rolon, D. Veynante, J. Martin, F. Durst, Exp. Fluids 11 (1991) 313–324.
[74] J.M. Bergthorson, K. Sone, T.W. Mattner, P.E. Dimotakis, D.G. Goodwin, D.I. Meiron, Phys. Rev. E 72 (2005) 066307.
[75] G. Amantini, J.H. Frank, M.D. Smooke, A. Gomez, Combust. Theor. Model. 11 (2007) 47–72.
[76] B. Sarnacki, G. Esposito, R. Krauss, H. Chelliah, Combust. Flame 159 (2012) 1026–1043.
[77] G.M.G. Watson, J.D. Munzar, J.M. Bergthorson, Energy Fuels 27 (2013) 7031–7043.
[78] T. Morel, J. Fluids Eng. 97 (1975) 225–233.
[79] F.N. Egolfopoulos, N. Hansen, Y. Ju, K. Kohse-Höinghaus, C.K. Law, F. Qi, Prog. Energy Combust. Sci. 43 (2014) 36–67.
[80] J. Jayachandran, A. Lefebvre, R. Zhao, F. Halter, E. Varea, B. Renou, F.N. Egolfopoulos, Proc. Combust. Inst. (2014), http://dx.doi.org/10.1016/j.proci.2014.05.031 (in press).
[81] I. Proudman, J. Fluid Mech. 9 (1960) 593–602.

9th US National Combustion Meeting
Organized by the Central States Section of the Combustion Institute
May 17-20, 2015
Cincinnati, Ohio

Autoignition of *n*-Heptane at Moderate Pressures

Gerald Mairinger[1,2]   *Ryan Gehmlich*[1]   *Ernst Pucher*[2],

Kalyanasundaram Seshadri[1]

[1]*Department of Mechanical and Aerospace Engineering, University of California at San Diego, La Jolla, California 92093-0411, USA*
[2]*Institute for Powertrains and Automotive Technology, Vienna University of Technology, A-1040 Vienna, Gusshausstrasse 27-29/315, Austria*

Abstract

An apparatus is constructed for measuring critical conditions of autoignition of *n*-heptane, in non-premixed flows, at moderate pressure. The counterflow configuration is employed. In this configuration a laminar flow of air is directed over the vaporizing surface of liquid *n*-heptane. The burner employed in this study in made up of a cup into which liquid *n*-heptane is introduced, at a rate that is equal to the rate of vaporization, so that the position of the liquid-gas interface is maintained at a constant level. Heated air is injected from a duct that is placed directly above the surface of the liquid pool. A mixing layer is established in the vicinity of the liquid gas interface. Autoignition takes place in this layer. It has been shown that the characteristic residence time is given by the reciprocal of the strain rate $a_2 = 2V_2/L$, where V_2 is the speed at which air is injected from the duct, and L is the distance between the liquid-gas interface and the exit of the duct. The counterflow burner is placed inside a stainless steel chamber designed for carrying out experiments at pressures up to 2.5 MPa. The chamber has optical access via four view-ports with fused silica windows. The pressure in the chamber is maintained constant during experiments using a TESCOM PID-control pressure regulation system. Air is heated in two stages. First it flows through three process heaters with a power of 750 watts each and a maximum exit temperature of 800 K. Next, air is heated using spiral silicon carbide heating element with power rating of 4800 watts. The surface temperature of the heating element can attain a maximum value of 1900 K. To prevent heat loss the duct is surrounded by a 2260 watts cylindrical ceramic heating furnace that can reach a surface temperature of 1200 K. A fused quartz tube separates the oxidizer stream from the nitrogen curtain. Another quartz tube separates the nitrogen curtain from the surrounding. The whole assembly consists of machined aluminum and stainless steel parts. Where necessary the parts are cooled with deionized water. Experimental measurements will include the temperature of air at autoignition is recorded as a function of pressure.

1   Introduction

Numerous experimental, computational and analytical studies have addressed autoignition of high molecular weight hydrocarbon fuels and jet fuels in shock tubes and rapid compression machines [1–5]. There are a number of studies on autoignition of hydrocarbon fuels and surrogates at atmospheric pressure in nonuniform flows [6–11].There are, however, very few studies on autoignition in nonuniform flows at elevated pressures. Here we report on an apparatus developed for measuring critical conditions of autoignition of *n*-heptane at moderate pressure.

A "High Pressure Combustion Experimental Facility" (HPCEF) was constructed at UCSD for carrying out experiments at pressures up to 25 bar. In the HPCEF different types of counterflow burners can be placed inside a high pressure chamber. Counterflow burners for conducting experiments on gaseous fuels and liquid fuels at elevated pressures were built and tested. Measurements that have been made using the HPCEF are critical conditions of flame extinction and temperature profiles. The capability of this system is currently being extended to allow measurements of critical conditions of autoignition. Further details are available in [12–14].

2   High Pressure Combustion Experimental Facility

The HPCEF can be used to study non-premixed, premixed and partially premixed combustion. The measurements that could be made include critical conditions of flame extinction and autoignition. Probes can be placed inside the pressure chamber to allow samples to be removed from the flame for analysis using gas chromatographs. Thermocouples can be placed inside the pressure chamber to allow measurements of temperature profiles. The facility has optical access to permit future nonintrusive, optical measurements of profiles of temperature and concentration of various species. Although the facility will be mainly employed for studies of combustion processes in non-uniform flow fields employing counterflow burners, it will be possible to house many different types of burners inside the pressure chamber. They include, for example, co-flow burners for studies on diffusion flames, and bunsen burners and flat flame burners for studies on premixed flames. The HPCEF is therefore a versatile facility that can be employed for experimental studies on non-premixed, premixed and partially premixed combustion using different burners and configurations.

Several systems are integral to the facility. These systems are described below.

2.1   Pressure Chamber

The main part of the HPCEF is a cylindrical pressure chamber made from stainless steel. Figure 1 is a photograph of the pressure chamber. Figure 2 is a photograph of a counterflow burner for burning fuels that are liquids at room temperature and pressure. The pressure chamber measures 40 inches from top to bottom and has a diameter of 15 inches with a wall thickness of 5/8 inch. Several hours of computational time was spent on finite elements stress analysis to properly design the dimensions of the chamber and to detect weak spots in the design. The chamber was designed to withstand a pressure of 150 bar which represents a safety factor of 5. It features four view-ports for optical access with an opening size of 4 inches. The bottom contains a number of through-puts for gas lines and electrical wiring. Threads for safety equipment and lifting hooks are incorporated in the top. The bottom is mounted to an aluminum stand, while the chamber cylinder and top can be lifted off, for easy access to the chamber inside. All flanges are sealed with o-rings and retained by bolted connections. Tempered one inch quartz windows are employed in the view-ports. Tension and slight impurities can have a significant impact on such a brittle material. A special test bomb was designed to pressurize the windows in a safe environment to verify the ability to withstand desired operating conditions. The quartz windows successfully withstood a pressure of 40 bar. In

addition the entire chamber underwent a hydrostatic pressure test of 40 bar without any damages or leakage.

2.2 Exhaust System

The products of combustion enter into an exhaust system where they are cooled before they are introduced into the exhaust treatment system in the laboratory. The counterflow burners employed in the HPCEF are equipped with water spray in the suction exhaust system, which sits in the lower part of the burner. Micro droplets of industrial water are injected onto the hot exhaust gases as they make their way from the reaction zone to the exhaust duct. The water spray serves multiple purposes. It works as a cooling agent that not only chills the exhaust gases, but also keeps the temperature of the burner body low which is important not only for the repeatability of the experiments but also for the longevity of the burner parts. Furthermore the water spray acts as a flame suppressant that prevents flame propagation into the exhaust system. In experiments where the fuels in use are prevaporized, the water spray allows the fuel to condense and a water-fuel mixture can safely be drained thus eliminating a reactive fuel-oxidizer mixture. The water spray system features six spray nozzles. The upper three nozzles provide a horizontal fan shaped spray pattern while the lower three provide a solid cone shaped pattern. Droplets do not exceed the size of 50 microns. The nozzles are connected in series with aluminum tubes for an even water pressure distribution. A spray forms as low as 200 ml/min and depending on the water supply pressure up to 1.2 l/min. Under normal experimental conditions a water flow of 2 l/min has been deemed sufficient for the purpose of exhaust after treatment.

2.3 Pressure Control Unit

The pressure inside the chamber is held constant at a desired value by a PID controlled back-pressure valve. The unit consists of a 100 psi electronic pressure controller, a 500 psi air-loaded regulator dome, a pressure transducer and a RS-485 communication module. The electronic pressure controller contains a PID control unit which automatically adjusts the output pressure based on a set point downloaded from a PC via a RS-485 connection. The pressurized air provided by the electronic pressure controller moves a diaphragm located in the regulator dome which multiplies the applied pressure by a factor 5 to the attached regulator valve. The process variable is provided by a pressure transducer mounted on the pressure chamber. For proper function of the unit a high-accuracy 24 V power supply and 110 psi of clean and dry air or nitrogen as a working medium for electronic pressure controller are required.

2.4 Computer Control Station

A quad-core processor PC equipped with a National Instruments PXI system is used as a central control and data collection unit. Several "Virtual Instruments" running on a Lab view platform were programmed to allow integration of multiple processes into customized controls. The PXI system features a multifunction digital/analog input/output data acquisition board. Pressure and

temperature measurements, water level sensing, solenoid valve controls, solid state relay controls, controls of flows and chamber pressure are monitored from the computer control unit.

2.5   Water Compression Unit

The compressed water required for the exhaust treatment is provided by a positive displacement pump. The unit is a combination of a pump head, a motor and a variable frequency drive. The low-pulse stainless steel pump head is designed to deliver 200 ml/min to 4 l/min depending on the rpm, but independent of press

2.6   Burner

Figures 2 shows a photograph of the counterflow burner used for testing liquid fuels. The figure shows the fuel cup and the ignition system. Figure 3 shows a cutaway view of the burner. The design incorporates a water-cooled liquid fuel cup and a delivery pipe through which fuel enters the cup. A thermocouple, for measuring fuel inlet temperature, is encased in a pressure-sealed stainless steel housing placed inside the delivery pipe. Surrounding the fuel cup is a nitrogen "curtain" delivery channel. Figure 3 shows water cooling channels for the burner, water spray nozzles for cooling the exhaust gases, an excess fuel drain to handle any potential spills of liquid fuel over the cup edge, and a semi-automatic ignition system. The parts are designed to be easy to disassemble for cleaning and maintenance, since burning high molecular weight fuels has a tendency to generate soot, and this soot buildup has to be periodically cleaned out.

2.7   Counterflow duct for Autoignition Experiments

Figures 4 and 5 show design details of the counterflow burners for heating air and nitrogen for use in autoignition experiments. The upper top frame contains the inlets for the air as well as the nitrogen stream. The lower top frame contains the water cooling channels and directs the nitrogen down to the duct. It is sealed against the upper frame with orings (Aluminium). The lower frame assembly consists of two stainless steel parts welded together. It is water cooled internally. Silicon carbide heating elements will be used. The surface temperatures of these heating elements can attain a temperature of 2100 K. A conically shaped machined quartz tube is used to separate the oxidizer stream from the nitrogen curtain. Quartz is necessary in view of the high temperatures in the system. Also a low thermal expansion coefficient is more favorable. A second quartz tube is employed to separate the nitrogen curtain from the surroundings. This tube is also exposed to high temperatures, so it is necessary to make it out of quartz. Iron-Chrome-Aluminum heating furnace is used for heating the nitrogen curtains. It can reach up to 1200 K.

(Program Manager Dr. Ralph A. Anthenien Jr).

References

[1] S. Dooley, S. H. Won, M. Chaos, J. Heyne, Y. Ju, F. L. Dryer, K. Kumar, C.-J. Sung, H. Wang, M. A. Oehlschlaeger, R. J. Santoro, and T. A. Litzinger. *Combustion and Flame*, 157 (2010) 2333–2339.

[2] S. Dooley, S. H. Won, J. Heyne, T. I. Farouk, Y. Ju, F. L. Dryer, K. Kumar, X. Hui, C.-J. Sung, H. Wang, M. A. Oehlschlaeger, V. Iyer, S. Iyer, T. A. Litzinger, R. J. Santoro, T. Malewicki, and K. Brezinsky. *Combustion and Flame*, 159 (2012) 1444–1466.

[3] T. Malewicki, S. Gudiyella, and K. Brezinsky. *Combustion and Flame*, 160 (2013) 17–30.

[4] D. Kim, J. Martz, and A. Violi. *Combustion and Flame*, 161 (2014) 1489–1498.

[5] N. Peters, G. Paczko, R. Seiser, and K. Seshadri. *Combustion and Flame*, 128 (2002) 38–59.

[6] S. Humer, A. Frassoldati, S. Granata, T. Faravelli, E. Ranzi, R. Seiser, and K. Seshadri. *Proceedings of the Combustion Institute*, 31 (2007) 393–400.

[7] S. Honnet, K. Seshadri, U. Niemann, and N. Peters. *Proceedings of the Combustion Institute*, 32 (2008) 485–492.

[8] S. Humer, R. Seiser, and K. Seshadri. *Journal of Propulsion and Power*, (2011) to appear.

[9] R. Seiser, K. Seshadri, E. Piskernik, and A. Liñán. *Combustion and Flame*, 122 (2000) 339–349.

[10] K. Seshadri, N. Peters, and G. Paczko. *Combustion and Flame*, 146 (2006) 33–59.

[11] R. Grana, K. Seshadri, A. Cuoci, U. Niemann, T. Faravelli, and E. Ranzi. *Combustion and Flame*, 159 (2012) 130–141.

[12] R. Gehmlich, A. Kuo, and K. Seshadri. *Proceedings of the Combustion Institute*, 35 (2014) in press.

[13] U. Niemann, K. Seshadri, and F. A. Williams. *Proceedings of the Combustion Institute*, 34 (2013) 881–886.

[14] U. Niemann, K. Seshadri, and F. A. Williams. *Combustion and Flame*, 161 (2014) 138–146.

5

Figure 1: Photo of the stainless steel pressure chamber mounted to an aluminum stand. Flanges connecting the cylindrical part to bottom and top are reinforced with gussets. All gas lines enter the chamber through the bottom part. Top and cylindrical part of the chamber can therefore be lifted off without dismantling any connections. The chamber is enclosed in a high-impact polycarbonate cubicle that provides an increased degree of safety in case of malfunction or accident.
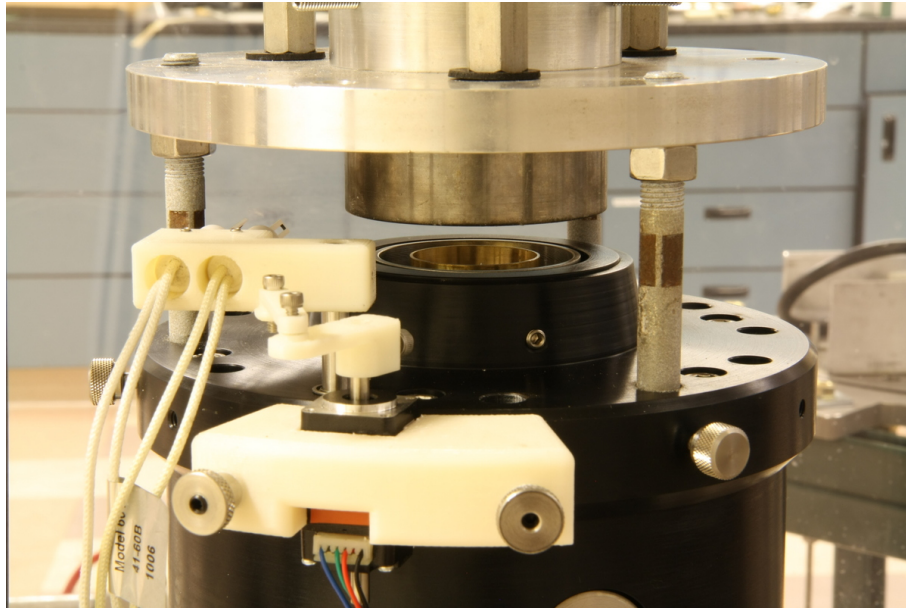
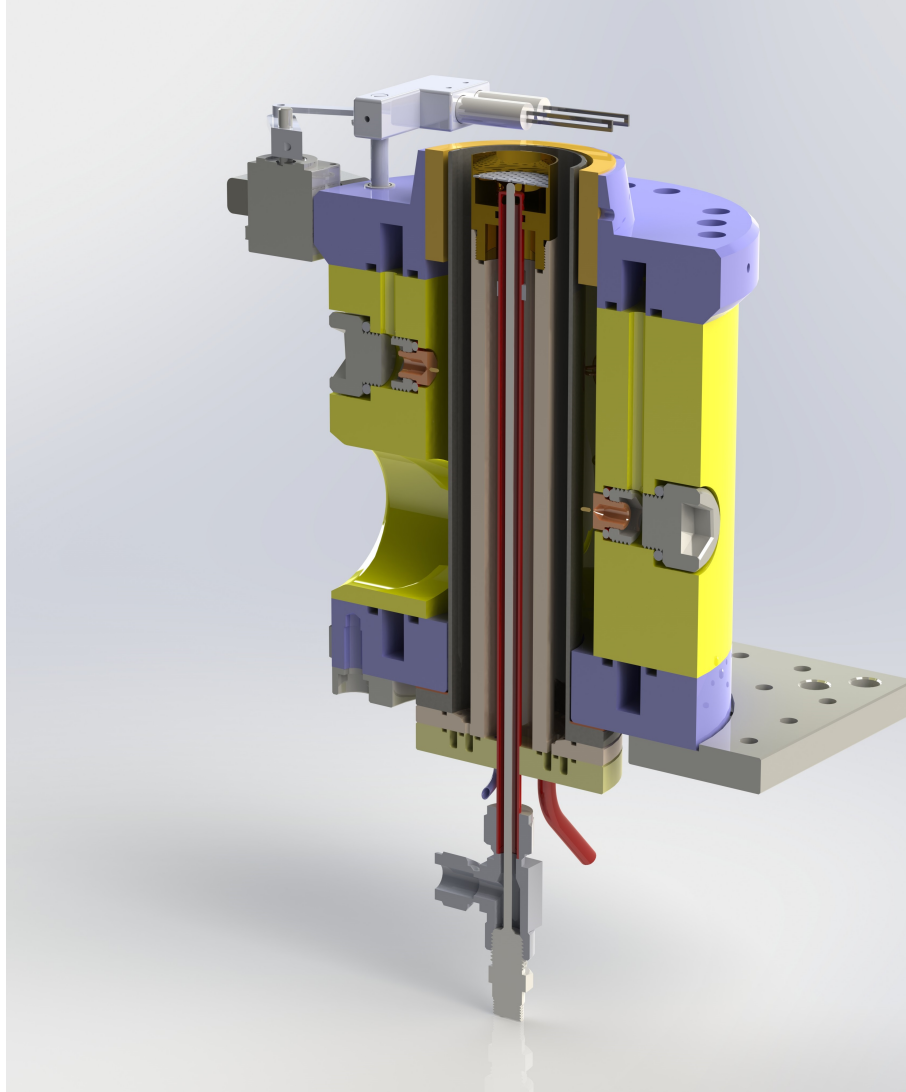**Figure 2: Photo of a counterflow burner for burning liquid fuels. The figure show the fuel cup**
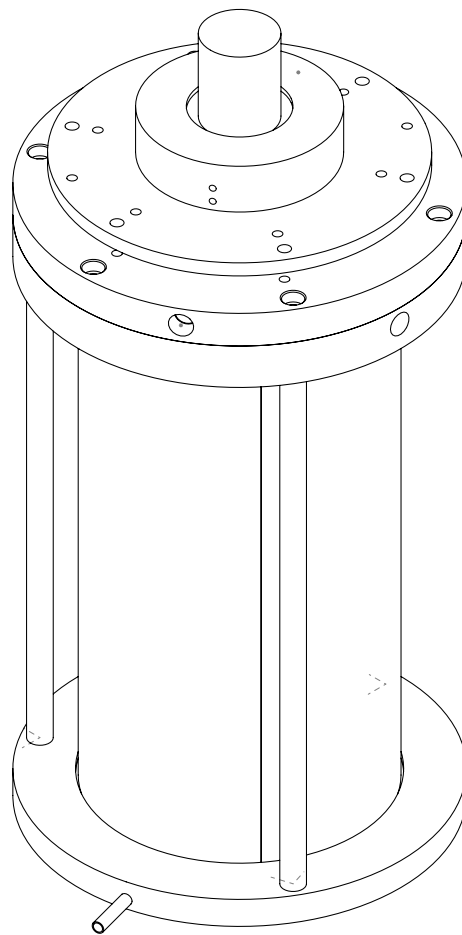
Figure 3: Cut away view of the liquid pool burner assembly.

3D-View

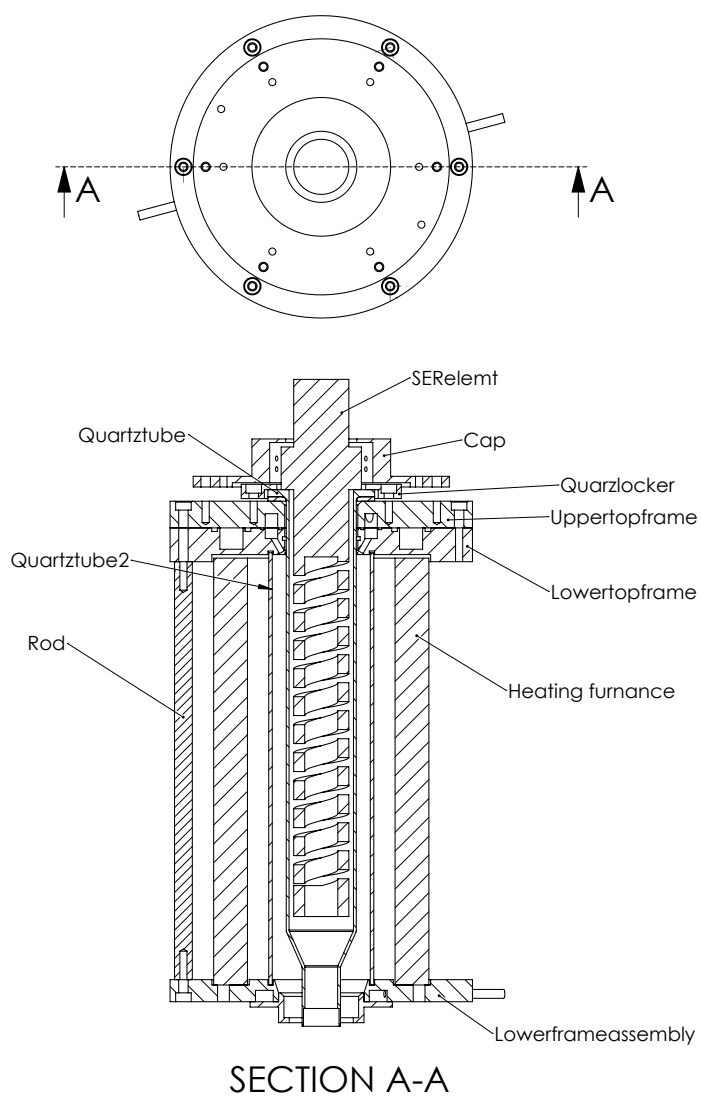**Figure 4: Counterflow duct for autoignition experiments.**

SECTION A-A

Figure 5: Counterflow duct for autoignition experiments. The figure shows the heating elements.

Manuscript

Autoignition of Condensed Hydrocarbon Fuels in Nonpremixed Flows at Elevated Pressures

Gerald Mairinger[a], Alessio Frassoldati[b], Ryan Gehmlich[a], Ulrich Niemann[a], Alessandro

Stagni[a], Eliseo Ranzi[b], Kalyanasundaram Seshadri[a]*

[a]*Department of Mechanical and Aerospace Engineering, University of California at San Diego, La Jolla, California 92093, USA*;
[b]*Dipartimento di Chimica Materiali, e Ingegneria Chimica "G. Natta", Politecnico di Milano, Piazza L. da Vinci 32, 20133 Milano, Italy*
(*Received 00 Month 200x; final version received 00 Month 200x*)

Experimental and computational investigation is carried out to elucidate the fundamental mechanism of autoignition of n-heptane, n-decane, and n-dodecane in nonpremixed flows at elevated pressures up to 6 bar. The counterflow configuration is employed. In this configuration a axisymmetric flow of a gaseous oxidizer stream is directed over the surface of an evaporating pool of a liquid fuel. The oxidizer stream is a mixture of oxygen and nitrogen. The experiments are conducted at a fixed value of mass fraction of oxygen and at a fixed low value of the strain rate. The temperature of the oxidizer stream at autoignition, T_{ig}, is measured as a function of pressure, p. Computations were carried out using skeletal mechanisms constructed from a detailed mechanism and critical conditions of autoignition were predicted. The experimental data and predictions show that for all fuels tested T_{ig} decreases with increasing p. At a fixed value of p, T_{ig} for n-dodecane is the lowest followed by n-decane and n-heptane. This indicates that n-dodecane is most easy to ignite followed by n-decane and n-heptane. This is in agreement with previous experimental and computational studies at 1 atm where a similar order of reactivities for these fuels were observed at low strain rates. Flame structures at conditions before and at conditions immediately after autoignition were calculated. A noteworthy finding is that low temperature chemistry was found to play a dominant role in promoting autoignition. The influence of low temperature chemistry was found to increase with increasing pressure.

Keywords: autoignition, hydrocarbon fuels, low temperature chemistry, nonpremixed flows, kinetic modelling.

1. Introduction

Fundamental knowledge of mechanisms of autoignition of condensed hydrocarbon fuels at elevated pressures is essential for accurate prediction of chemical processes taking place in propulsion systems. Numerous experimental, computational and analytical studies have addressed combustion of high molecular weight hydrocarbon fuels, methane, ethane, ethene, and hydrogen at elevated pressures [1–12]. These studies include measurements and prediction of combustion processes in shock tubes, flow reactors and rapid compression machines [1–6], extinction of counterflow nonpremixed flames [7–10], autoignition in nonpremixed flows [11], and laminar premixed flames [12]. In contrast to numerous studies of autoignition of high molecular weight hydrocarbon fuels in homogeneous systems [1–6], there are very limited studies on autoignition of these fuels in nonuniform flows and

---

at elevated pressures. There are, however, a number of studies on autoignition of these fuels at atmospheric pressure in nonuniform flows [13–18].

In a previous study [16], critical conditions of extinction and autoignition were measured for many condensed hydrocarbon fuels in nonpremixed flows at atmospheric pressure. The fuels considered were n-heptane, n-decane, n-dodecane, n-hexadecane, and *iso*-octane. It was found that at low values of the strain rate, n-hexadecane is most easy to ignite followed by n-dodecane, n-decane, and n-heptane. Activation-energy asymptotic theory was employed to interpret the results [16]. In a subsequent study a semi-detailed chemical-kinetic mechanism was used to predict critical conditions of autoignition for these fuels [17]. The predictions were in agreement with the experimental data. A noteworthy finding was that the reactivities of these fuels is a result of competition between the rates of low temperature chemistry, rates of high temperature chemistry, and rates of molecular transport. At low strain rates autoignition was promoted by low temperature chemistry and the influence of molecular transport was not pronounced [17]. As the strain rate is increased, the influence of low temperature chemistry on autoignition was observed to diminish and influence of high temperature chemistry and rates molecular transport were found to increase. The present study extends this previous work to elevated pressures to investigate the relative influence of low temperature chemistry and high temperature chemistry on autoignition. An experimental and kinetic modeling study is carried out on mechanisms of autoignition of n-heptane, n-decane, and n-dodecane at elevated pressures. Critical conditions of autoignition are measured and compared with predictions obtained using skeletal chemical-kinetic mechanisms. This work also complements a previous study of critical conditions of extinction of these condensed fuels at elevated pressures [10].

2.   Experiment

Figure 1 is a schematic illustration of the "condensed-fuel" counterflow configu-
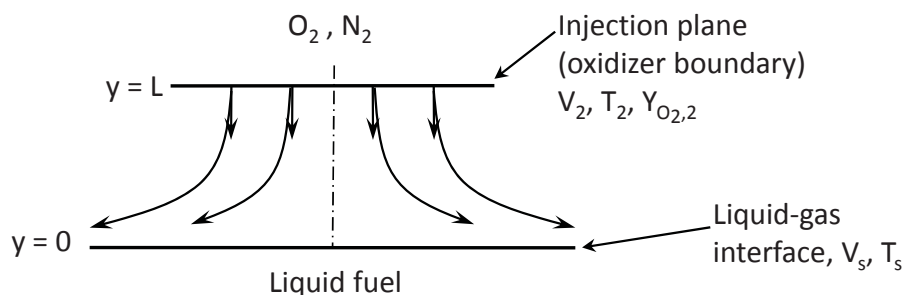

Figure 1.   Schematic illustration of the counterflow configuration. V_2 and V_s are the velocities at the oxidizer-boundary and on the gas side of the liquid-gas interface, respectively. T_2 and T_s are the temperatures at the oxidizer-boundary and the liquid-gas interface, respectively.

ration employed here in the experimental and computational study. In this configuration an axisymmetric flow of a gaseous oxidizer stream is directed over the surface of an evaporating pool of a liquid fuel. The oxidizer stream is a mixture of oxygen (O_2) and nitrogen (N_2). It is injected from the oxidizer-duct, the exit of which is the oxidizer-boundary. The origin is placed on the axis of symmetry at the surface of the liquid pool, and y is the axial co-ordinate and r the radial co-ordinate. The distance between the liquid-gas interface and the oxidizer-boundary is L. At the oxidizer-boundary, the magnitude of the injection velocity is V_2, the

temperature T_2, the density ρ_2, and the mass fraction of oxygen $Y_{O_2,2}$. Here subscript 2 represents conditions at the oxidizer-boundary. The radial component of the flow velocity at the oxidizer-boundary is presumed to be equal to zero. The temperature at the liquid-gas interface is T_s, and the mass averaged velocity on the gas side of the liquid-gas interface is V_s. Here subscript s represents conditions on the gas side of the liquid-gas interface. It has been shown previously [16] that the radial component of the flow velocity at the liquid-gas interface is small and can be presumed to be equal to zero. It has been shown that in the asymptotic limit of large Reynolds number the stagnation plane formed between the oxidizer stream and the fuel vapors is close to the liquid-gas interface and a thin boundary layer is established there. The inviscid flow outside the boundary layer is rotational. The local strain rate, a_2, at the stagnation plane, is given by [16, 19].

$$a_2 = 2V_2/L. \tag{1}$$

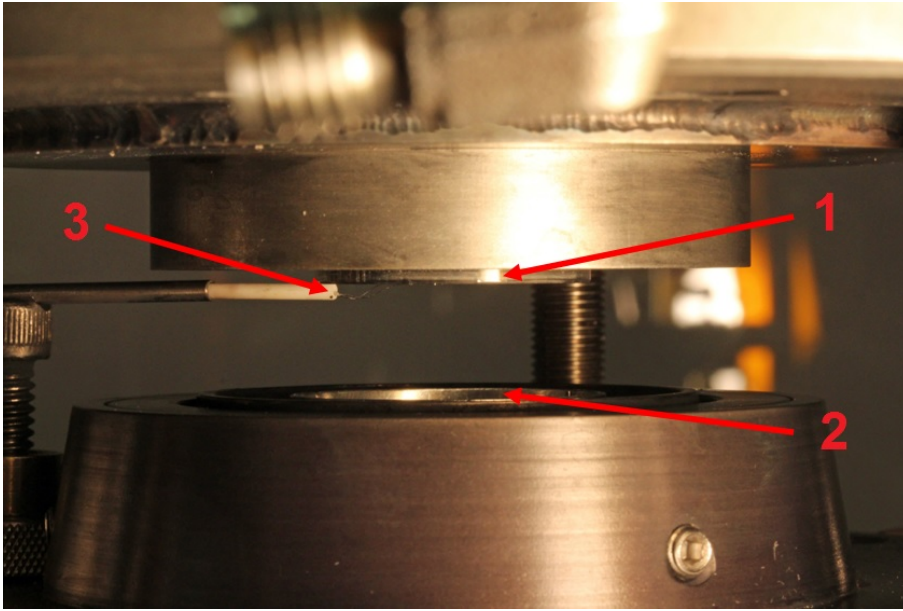Figure 2 shows a photograph of condensed-fuel burner. It shows the fuel-cup,

Figure 2.   Photograph of the counterflow burner. The photo shows the exit of the oxidizer-duct (1), the fuel-cup (2), and the thermocouple employed to measure the temperature of the oxidizer stream (3).

the oxidizer-duct, and the Pt-Pt 13% Rh thermocouple with a wire diameter of $0.127\,\mathrm{mm}$ and a junction diameter of $0.21\,\mathrm{mm}$ that is used to measure the temperature of the oxidizer stream, T_2. The fuel-cup has an outer diameter of $31.75\,\mathrm{mm}$ and inner diameter of $30.2\,\mathrm{mm}$. The distance between the exit of the oxidizer-duct and the surface of the liquid pool is $12\,\mathrm{mm}$. Fuel is supplied to the fuel cup by ISCO 500D syringe pump with a volumetric flow accuracy of $\pm 0.01\,\mathrm{mL/min}$. The temperature of the fuel entering the cup is T_c. A stainless steel screen is placed in the fuel-cup to minimize flow disturbances. The lower part of the fuel cup is cooled by water so that fuel always enters the cup at a temperature close to 300 K. The pool temperature is measured by a thermocouple located at the point where the fuel enters the fuel cup. Further details of the fuel-cup including the procedure employed to maintain the level of the liquid fuel in the cup is described in detail elsewhere [10].
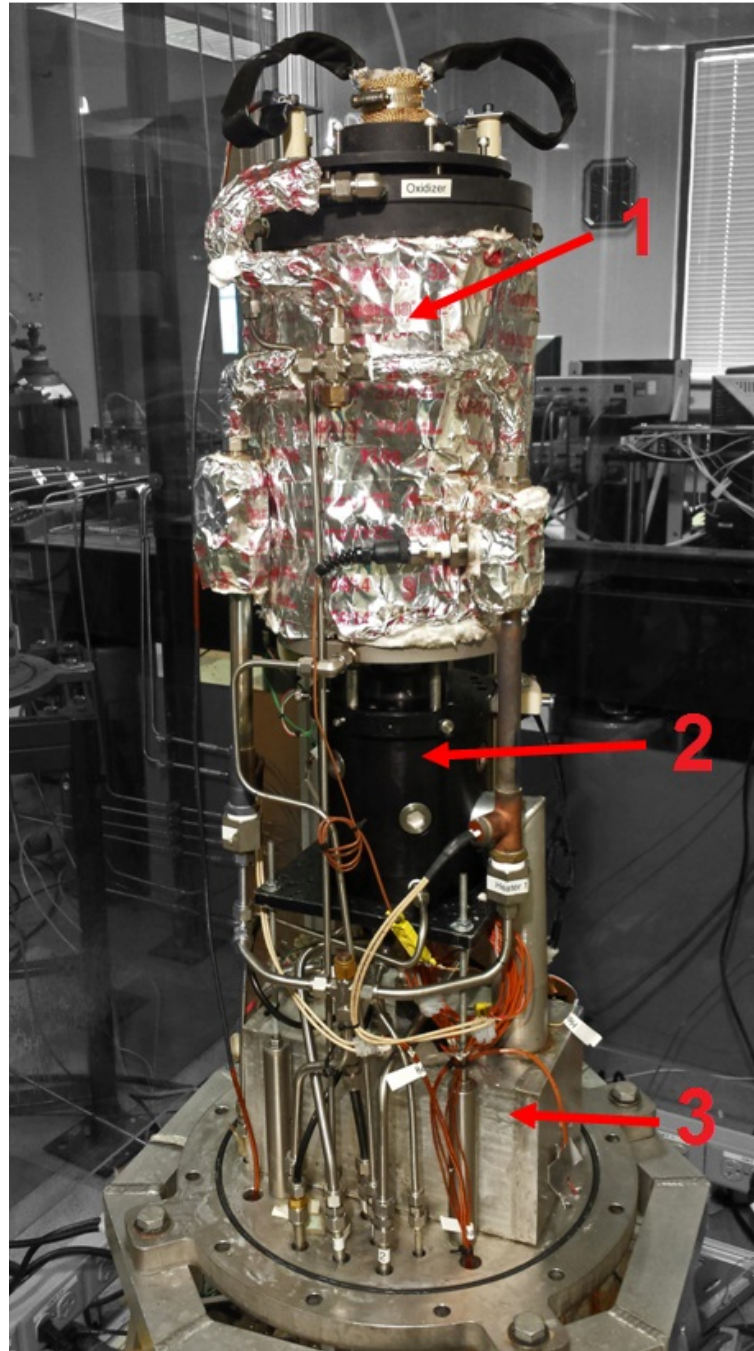
Figure 3.   Photograph of the burner. It shows the oxidizer duct (1), the liquid-pool assembly (2), and the water collector unit for cooling exhaust gases (3).

Figure 3 Figure 3 is a photograph of the counterflow burner and Fig. 4 is a photograph of the oxidizer duct. The counterflow burner is made up of two concentric quartz tubes. The inner tube has an inner diameter of 25.4 mm and an outer diameter of 27.4 mm. The oxidizer stream flows through the inner tube and nitrogen through the outer tube. Three 200 mesh fine wire Inconel 600 screens are placed at the exit of the quartz tube to achieve plug-flow conditions at the exit. The screens are held with inconel rings and are recessed by 1 mm. As a consequence the effective exit diameter of the oxidizer-duct is 22.5 mm and the distance between the liquid-gas interface and the oxidizer boundary is $L = 13$ mm. These numbers are used to evaluate the exit velocity, V_2, and the
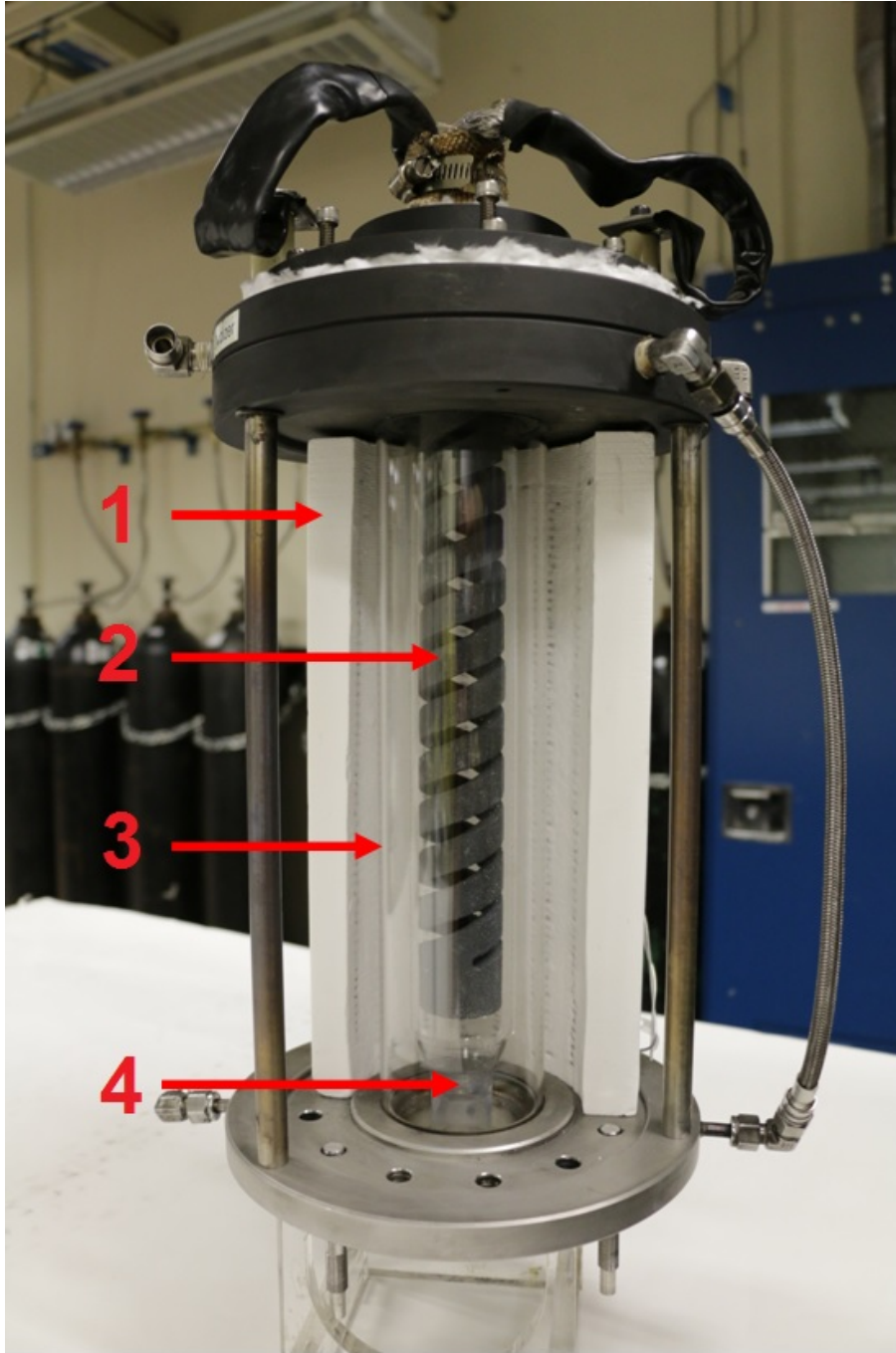
Figure 4.   Photograph of the oxidizer duct. It shows the ceramic heater (1), the silicon carbide heating element (2), the concentric quartz tube for nitrogen shield (3), and quartz tube for oxidizer (4).

strain rate using Eq. (1). A silicon carbide heating element, 381 mm long with a diameter of 33.1 mm and a output of 3600 watts, is placed inside the inner quartz tube. The distance between the end of the heating element and the exit oxidizer duct is 80.0 mm. The surface of the heating element can reach a temperature of 1900 K. To minimize heat losses to the environment the duct is surrounded by a 2260 watt cylindrical ceramic heating furnace that can reach a surface temperature of 1200 K, as shown in Fig. 3. Three 750 watt process heaters are used to preheat the oxidizer stream up to 700 K before it enters the quartz tube. All gaseous streams are controlled by computer regulated analog mass flow controllers.

Experiments are conducted with the counterflow burner placed inside the High Pressure Combustion Experimental Facility (HPCEF) described elsewhere [8–10]. The main part of the HPCEF is a cylindrical pressure chamber made from stainless steel. It measures 101.6 cm from top to bottom and has a diameter of 36 cm. Experiments up to a pressure of 25 bar can be carried out in the HPCEF. The reactive flow field is characterized by the value of pressure, p, the mass fraction of oxygen, $Y_{O_2,2}$, and the temperature, T_2 of the oxidizer stream, and the strain rate, a_2. The experiments were conducted at a fixed values of $Y_{O_2,2} = 0.15$ and $a_2 = 138^{-1}$s. The temperature of the oxidizer stream at autoignition, T_{ig}, was measured as a function of p. The measured temperatures were corrected to account for heat losses by radiation from the theromocouple wires [20]. The values of $Y_{O_2,2}$ and a_2 were selected to minimize rates of soot formation.

The procedure for measuring critical conditions of autoignition is as follows. First the desired chamber pressure is established by introducing nitrogen into the chamber. Water cooling systems are activated. The flowfield is established by setting the desired value of Y_{O_2} the strain rate and T_2. Liquid fuel is introduced into the fuel-cup. The syringe pump is used to control the level of the liquid fuel in the cup. The temperature of the oxidizer stream is gradually increased in small increments, allowing sufficient time for the system to reach steady-state, until autoignition takes place. The autoignition event is recorded using a high speed video camera operating at 500 frames per second. Data is recorded only if autoignition takes place around the axis of symmetry. These measurements are performed for different values of p. Figure 5 shows a typical autoignition event recorded by the high speed camera. The figure shows the progression of the ignition event at successive values of the time, t. The large nearly circular illumination is from the lamp used to illuminate the surface of the liquid pool. The first image shows the onset of autoignition where the flame is seen as a small circular disc around the axis of symmetry. In the subsequent images the diameter of the flame increases. The repeatability of the measurements of autoignition temperatures is ± 10 K. The accuracy is expected to be 30 K and is attributed to uncertainties in evaluating the correction that must be applied to the measured temperature due to heat losses from radiation from the thermocouple.

3.   Formulation

Kinetic modeling is carried out using skeletal chemical-kinetic mechanisms constructed from the POLIMI-1412 detailed chemical-kinetic mechanism [21]. This detailed mechanism describes the pyrolysis, partial oxidation and combustion of hydrocarbons up to C_{16}, and oxygenated fuels [22]. It employs a lumped approach for describing the primary propagation reactions from high molecular weight species to lower molecular weight species. The successive reactions of these low molecular weight species are then described using detailed chemical-kinetic schemes. The role of the lumped approach in the context of mechanism reduction has been recently discussed in detail by Ranzi et al [23]. This comprehensive kinetic model has been recently updated to include new reaction classes, to facilitate better prediction of the reactivity of alkanes at very low temperatures and to explain the formation of oxygenated species, such as organic acids and dicarbonyl species [24, 25]. In the present work, the mechanism reduction was performed using the DoctorSMOKE++ software [26], which implements a numer-
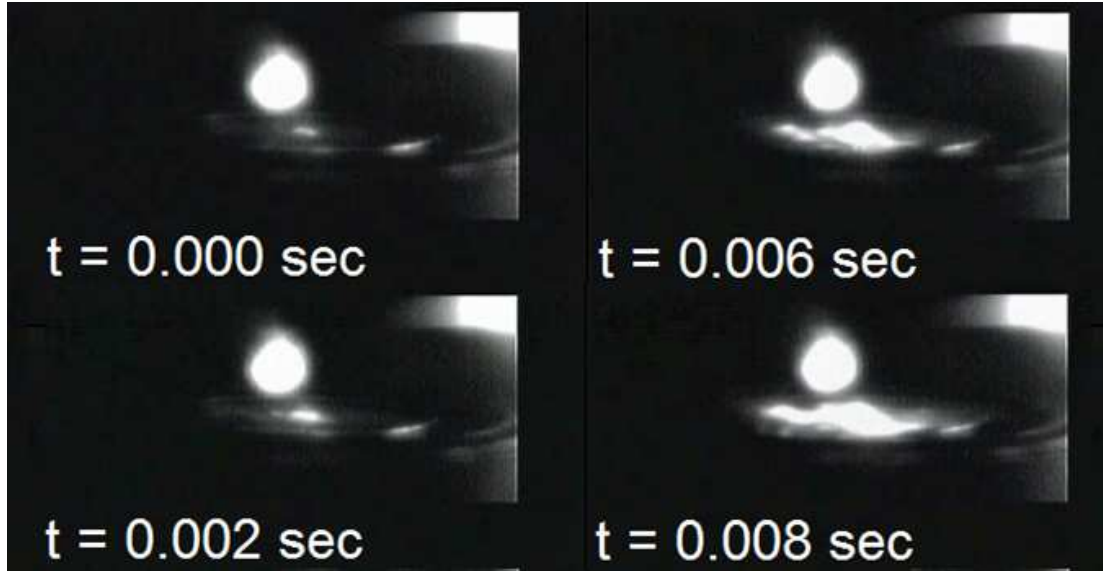
Figure 5. High speed photograph of a typical autoignition event at $p = 4.5\,\mathrm{bar}$ $Y_{O_2} = 0.15$, strain rate $a_2 = 138\,\mathrm{s}^{-1}$, and $T_\mathrm{ig} = 886\,\mathrm{K}$. The fuel is n-decane

ical algorithm based on directed relation graph (DRG) with error propagation and sensitivity analysis that includes sensitivity analysis on reactions [27]. The skeletal mechanisms were tested by comparing predictions of ignition delay times in adiabatic, constant pressure batch reactors with those of a detailed scheme over a temperature range of $500\,\mathrm{K}$ to $1700\,\mathrm{K}$ and pressures up to $40\,\mathrm{bar}$. The differences in the predictions were constrained to be to less than $10\,\%$. Since the application considered here is prediction of critical conditions of autoignition in nonpremixed flows, the skeletal mechanisms were tested over a wide range of equivalence ratio, ϕ, from very lean $\phi = 0.2$ to very rich $\phi = 8$ conditions. After the reduction, the three skeletal mechanisms were made up of about 3000 reactions among 117 species for n-heptane, 122 for n-decane and 136 for n-dodecane. Although the accuracy of predictions of ignition-delay times of n-alkanes by the POLIMI mechanism has been tested previously [28], the performance of the three skeletal mechanisms employed here is tested to ensure that the reduction procedure retained the predictive accuracy of the POLIMI mechanism. Figures 6, 7, and 8 compare predictions of ignition-delay times obtained using the skeletal mechanisms with corresponding measured values in shock-tubes reported in the literature[29–35] for the n-heptane, n-decane, and n-dodecane. The symbols represent experimental data and the lines are predictions obtained using the skeletal mechanism for these fuels. The predictions agree well with experimental data for a wide range of values of pressures and temperatures thus confirming the previous benchmarks, as well as the effectiveness of the reduction methodology.

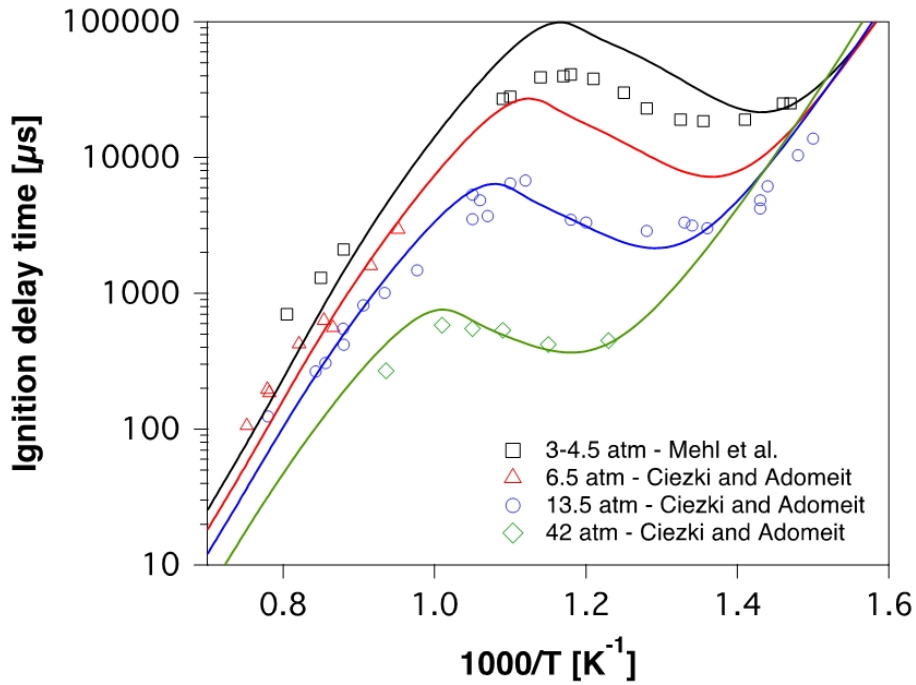The computations were performed with the OpenSMOKE++ code [36]. The

Figure 6.   Comparison of predictions of ignition-delay times obtained using the skeletal mechanism for *n*-heptane with corresponding measured values in shock-tubes reported in the literature [29, 30].
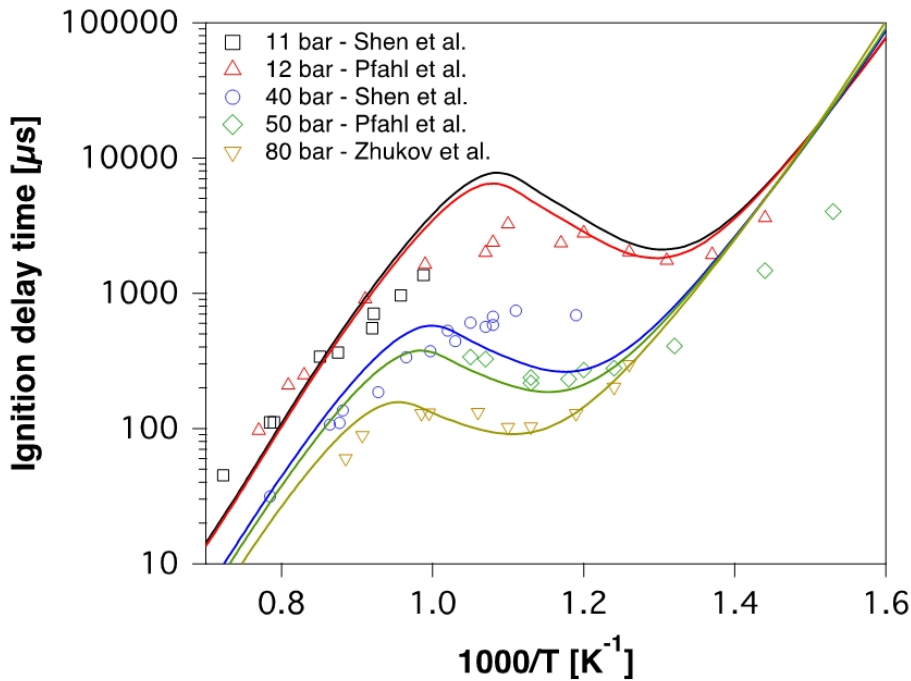

Figure 7.   Comparison of predictions of ignition-delay times obtained using the skeletal mechanism for *n*-decane with corresponding measured values in shock-tubes reported in the literature [31–33].

structure of the reactive flow-field is obtained by solving the conservation equations of mass, momentum and energy and species balance. Boundary conditions are applied at the exit of the oxidizer duct and on the gas side of the liquid-gas interface [16, 17, 37]. At the oxidizer-boundary, the injection velocity V_2, the temperature, T_2, and the composition of the oxidizer are specified. The radial component of the flow velocity is presumed to be equal to zero at the oxidizer-boundary. At the
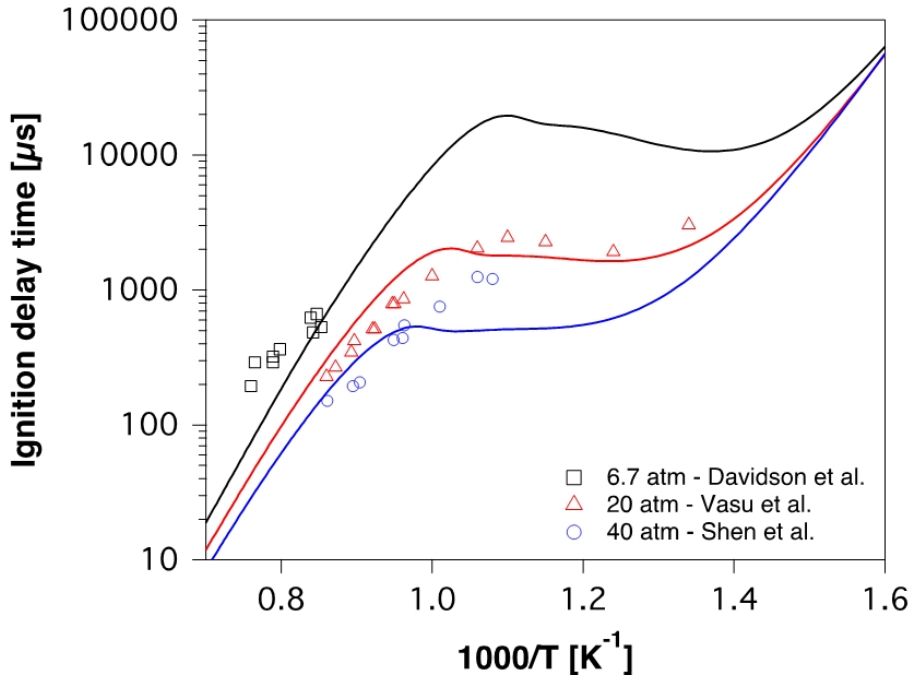
Figure 8.   Comparison of predictions of ignition-delay times obtained using the skeletal mechanism for
n-dodecane with corresponding measured values in shock-tubes reported in the literature [31, 34, 35].

liquid-gas interface, mixed boundary conditions are applied for the species balance
equations, and the energy conservation equation. The total mass flux of all species,
i, is comprised of the diffusive flux, $j_{i,s}$, and the convective terms. This total mass
flux for all species, except that for the fuel, is prescribed to vanish at the liquid-
gas interface. The heat flux at the liquid-gas interface is balanced by the product
of $\dot{m}$ and the heat of vaporization h_L, and the sensible heat required to raise the
temperature of the liquid from T_c to T_s. The temperature at the liquid-gas interface,
T_s, is obtained using Raoult's Law. Empirical coefficients for calculating the vapor
pressure, and the heat of vaporization, for these fuels are given in Ref. [38]. No-slip
boundary condition is applied [16, 17]. The boundary condition at the liquid-gas
interface is written as [17, 37, 39]

$$
\begin{aligned}
&\dot{m} Y_{i,s} + j_{i,s} = 0, \quad i{\neq}F, \\
&\dot{m} \left(1 - Y_{F,s}\right) - j_{F,s} = 0, \\
&\left[\lambda \left(dT/dy\right)\right]_s - \dot{m} \left[h_L + C_c \left(T_s - T_c\right)\right] = 0, \\
&P_v^{\text{sat}}(T_s) - X_{F,s} p = 0
\end{aligned}
\tag{2}
$$

Here λ is the thermal conductivity of the gas at the liquid-gas interface, C_c the
heat capacity of the liquid, P_v^{sat} the saturation vapor pressure, and $X_{F,s}$ the mole
fraction of fuel at the liquid-gas interface. Heat transfer from the liquid to the
burner is neglected. The boundary condition at the exit of the oxidizer duct is
modeled using a rate of rise for the oxidizer stream temperature of $0.1\,\text{K/s}$, starting
from unreactive ambient conditions ($300\,\text{K}$), similar to the procedure used in the
measurement. This value is sufficiently slow, because with faster temperature
rise rates ($1\,\text{K/s}$) the model predicts the same autoignition temperatures. The
structure of the reactive flow field is obtained by solving the unsteady conservation
equations of mass, momentum and energy and species balance and are described
in detail elsewhere [40, 41].

Simulations were performed using a computational grid with more than 225 grid points to ensure grid insensitive results. The computations were performed for values of pressure between $1\,\mathrm{atm}$ and $6\,\mathrm{atm}$, with $Y_{O_2} = 0.15$ and $a_2 = 138\,\mathrm{s}^{-1}$. The fuels considered were *n*-heptane, *n*-decane, and *n*-dodecane. Flame structure and critical conditions of autoignition were predicted. A converged non-reactive (cold) solution is first obtained for $T_2 = 300\,\mathrm{K}$. The temperature of the oxidizer stream is increased until autoignition takes place and a hot flame is established. For the given value of the strain rate, autoignition is defined to take place at the value of temperature of the oxidizer stream, $T_2 = T_{\mathrm{ig}}$ where an abrupt transition takes place from a weakly reactive region to a flame.

4.   Results and Discussion

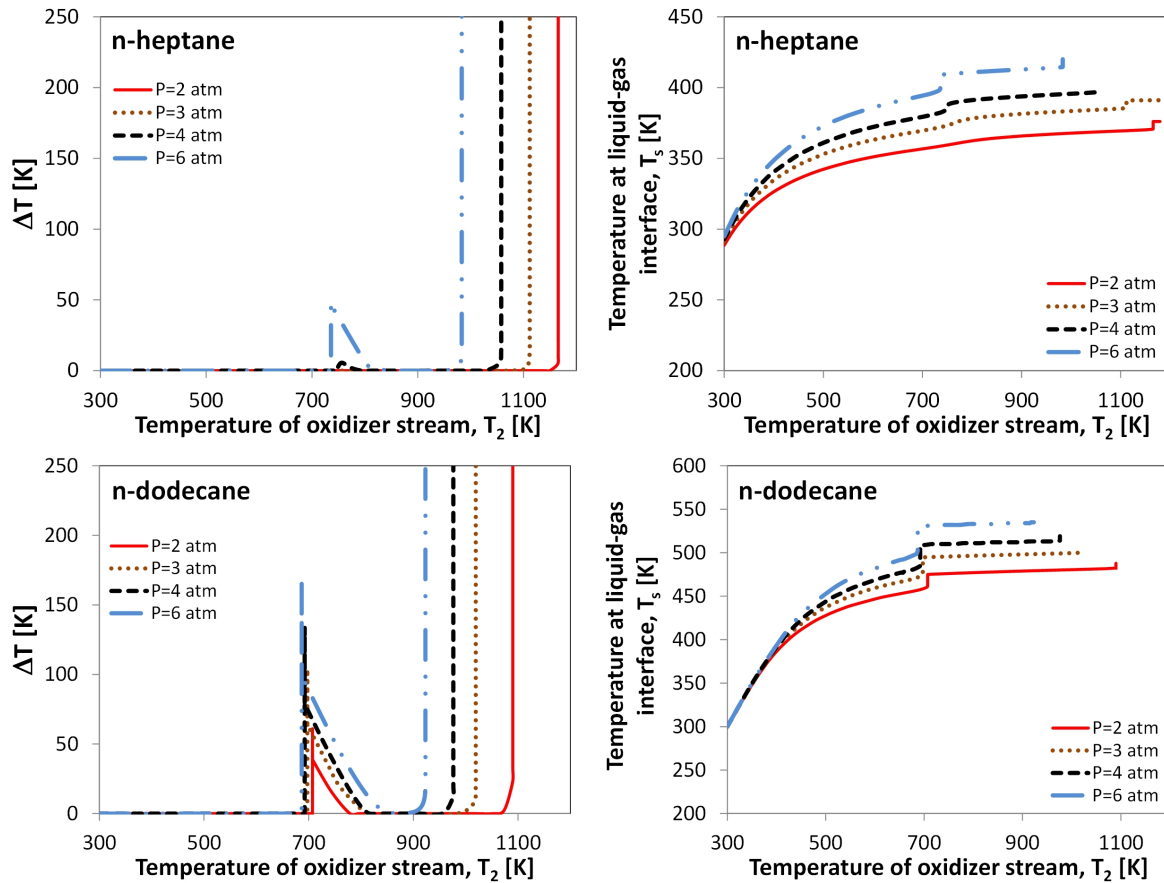Figure 9 shows, for *n*-heptane and *n*-dodecane, the temperature increment ΔT

Figure 9.   Temperature increment ΔT [K] and temperature at the liquid gas interface, T_s, as a function of the temperature of the oxidizer stream, T_2, for various values of the pressure, p. The computations were done at fixed $T_2 = 300\,\mathrm{K}$, and $Y_{O_2} = 0.15$.

[K] and temperature at the liquid gas interface as a function of T_2, for various values of p. The temperature increment is defined as the difference between the peak value of the temperature in the mixing layer and T_2. For both fuels, as the temperature of the oxidizer stream is increased, a weakly reactive region appears that is marked by an increase in temperature in the mixing layer followed by a decrease in temperature. Further increase in T_2 leads to a rapid rise in temperature indicating that autoignition has taken place. This is referred here as

hot ignition. The temperature rise in the weakly reacting region is around $100\,\mathrm{K}$ and it is indicative of low temperature chemistry taking place in the reaction zone. The low temperature reactivity peaks around $700\,\mathrm{K}$ which is close to the crossover temperature defined by Peters et al. [5]. Figure 9 shows the existence of the negative temperature coefficient (NTC) region after the weakly reactive region and before the rapid rise in temperature. This clearly indicates the onset of two-stage ignition. Figure 9 shows that for both fuels, the reactivity of the region where low temperature chemistry is taking place increases with increasing pressure. This in turn advances the onset of autoignition by decreasing the value of the autoignition temperature T_{ig} where hot ignition takes place. Figure 9 shows that the temperature at the liquid-gas interface increases with increasing pressure as a consequence of increase in partial pressure. More importantly, the surface temperature of a liquid pool of n-dodecane is higher than that of n-heptane, because at a given temperature the vapor pressure of n-dodecane is lower than that of n-heptane. As a consequence, for a given T_2, the surface temperature of a pool of n-dodecane must be higher than that of n-heptane to achieve comparable mass evaporation rates. Figure 9 shows that at a given value of T_2 and p the difference between the surface temperature of pool of n-dodecane and that of n-heptane is more than $100\,\mathrm{K}$ for all values of p. This higher evaporation temperature makes a significant contribution to lowering the values of T_{ig} for n-dodecane in comparison to n-heptane for the same value of p and T_2. The temperature of the liquid-gas interface also increases with increasing T_2 as a consequence of heat release, first from low temperature chemistry and later from high temperature chemistry.

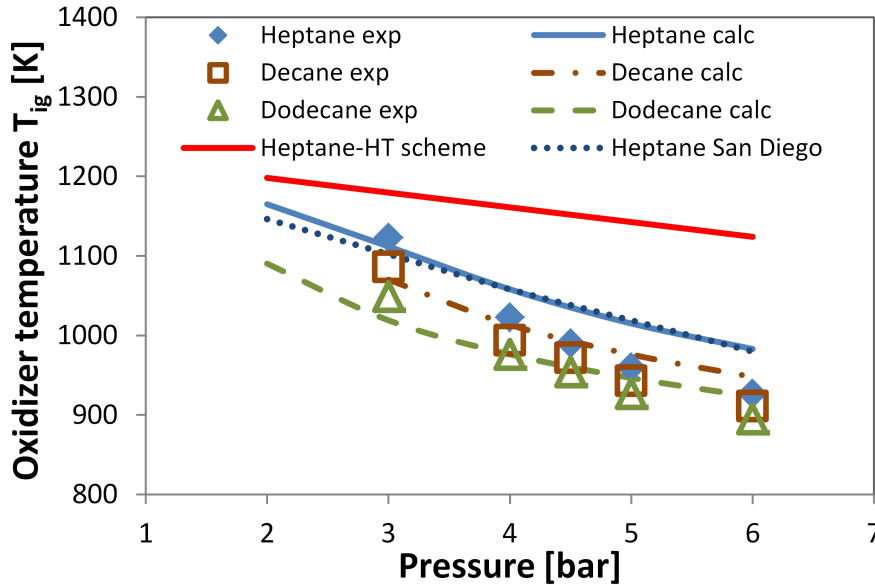Figure 10 compares the measured and predicted values of critical conditions

Figure 10. The temperature of the oxidizer stream at autoignition, T_{ig} as a function of pressure at fixed $a_2 = 138\,\mathrm{s}^{-1}$, and $Y_{O_2} = 0.15$. The symbols represent experimental data and the lines are predictions. The figure includes prediction of T_{ig} for n-heptane using the San Diego Mechanism [42].

of hot flame autoignition of all fuels tested. The predictions include those made for n-heptane employing the San Diego Mechanism [42]. The experimental data and predictions show a significant decrease in the value of T_{ig}, in the range of $150\,\mathrm{K}$ to $200\,\mathrm{K}$, with increase in pressure from $3\,\mathrm{bar}$ to $6\,\mathrm{bar}$. In general at a given value of p, T_{ig} for n-dodecane is the lowest followed by n-decane and n-heptane.

Thus n-dodecane is easiest to ignite followed by n-decane and n-heptane. This is consistent with the results shown in Fig. 9, wherein the influence of low temperature chemistry increases with increasing pressure, and that of Grana et. al [17] who observed a similar order of reactivities for these fuels at low strain rates. The study in [17] was at a pressure of 1.0 atm and oxygen mass fraction of 0.233. Figure 10 shows that predictions in general well agree with the experimental measurements. In view of previous finding that at low strain rates the influence of molecular transport is less important than that of low temperature chemistry, the relatively small differences between the measured and predicted value of T_{ig} could be attributed to uncertainties in the experimental measurements and in the description of low temperature chemistry. The low temperature chemistry in the Polimi mechanism has been recently revised and analyzed in detail for alkanes [23–25, 43], and provides reliable prediction of ignition delay times, as already shown in Figures 6, 7, and 8. Figure 10 shows that the predictions of T_{ig} obtained when the low temperature chemistry of n-heptane is excluded is different from those obtained when low-temperature chemistry is included. This difference is a quantitative measure of the influence of the low temperature chemistry on critical conditions of autoignition of n-heptane. It shows that the influence of low temperature chemistry, on autoignition of n-heptane increases with increasing pressure. Similar behaviour can be expected for the other fuels tested here.

Figure 11 shows the temperature profile, and profiles of n-heptane, oxygen, hydrogen peroxide (H_2O_2), and heptyl-ketohydroperoxide ($OC_7H_{13}OOH$), referred to here as KET, and heat release rates, Q_{reac}, as a function of the height about the liquid-gas interface for times corresponding to various values of T_2, that includes conditions before onset of autoignition and immediately after. These profiles were calculated for $p = 6\,\mathrm{atm}$, $a_2 = 138\,\mathrm{s}^{-1}$, and $Y_{O_2} = 0.15$. KET is marked as NC$_7$-OQOOH in Fig. 11. The location of the stagnation plane is also marked. Autoignition at these conditions takes place around 980 K. For values of T_2 less than T_{ig}, significant reactivity associated with low temperature oxidation chemistry is present. The fuel diffuses through the stagnation plane and reaction proceeds through the typical low temperature chemistry path, forming H_2O_2, peroxides and ketohydroperoxides as well as heptenes and heterocycle components. The temperature profile shows a monotonic increase, there is a small amount of heat release, and KET is formed and consumed. The formation of ketohydroperoxides peaks at T_2 of about 740 K, while increasing the temperature further favors the formation of H_2O_2, as the system approaches the intermediate temperature regime [44] where the OH radical reactions, such as OH + OH + M = H_2O_2 + M, play an important role. Figure 6 shows that at $p = 6\,\mathrm{bar}$ the NTC region is located for values of T_2 between 730 K and 850 K. A noteworthy observation is that in this region the low temperature reactivity decreases with increasing T_2. For this reason, the peak values of mole fraction of the peroxides and KET in Fig. 11 decreases with increasing T_2. As discussed, H_2O_2 exhibits a different behavior and peaks in the intermediate temperature region, just before the hot ignition. Finally, at very low temperatures (600 K) the peroxides are not formed because of insufficient reactivity, while at high temperatures the peroxides are decomposed and a hot flame is established.

Another noteworthy observation is that in the region where KET is formed and produced, the mole fractions of C_7H_{16} and O_2 is high, indicating leakages of both fuel and oxygen. The flame structure, therefore, resembles that of a nonpremixed flame in the partial-burning regime analysed by Liñán [45]. The flame structure for
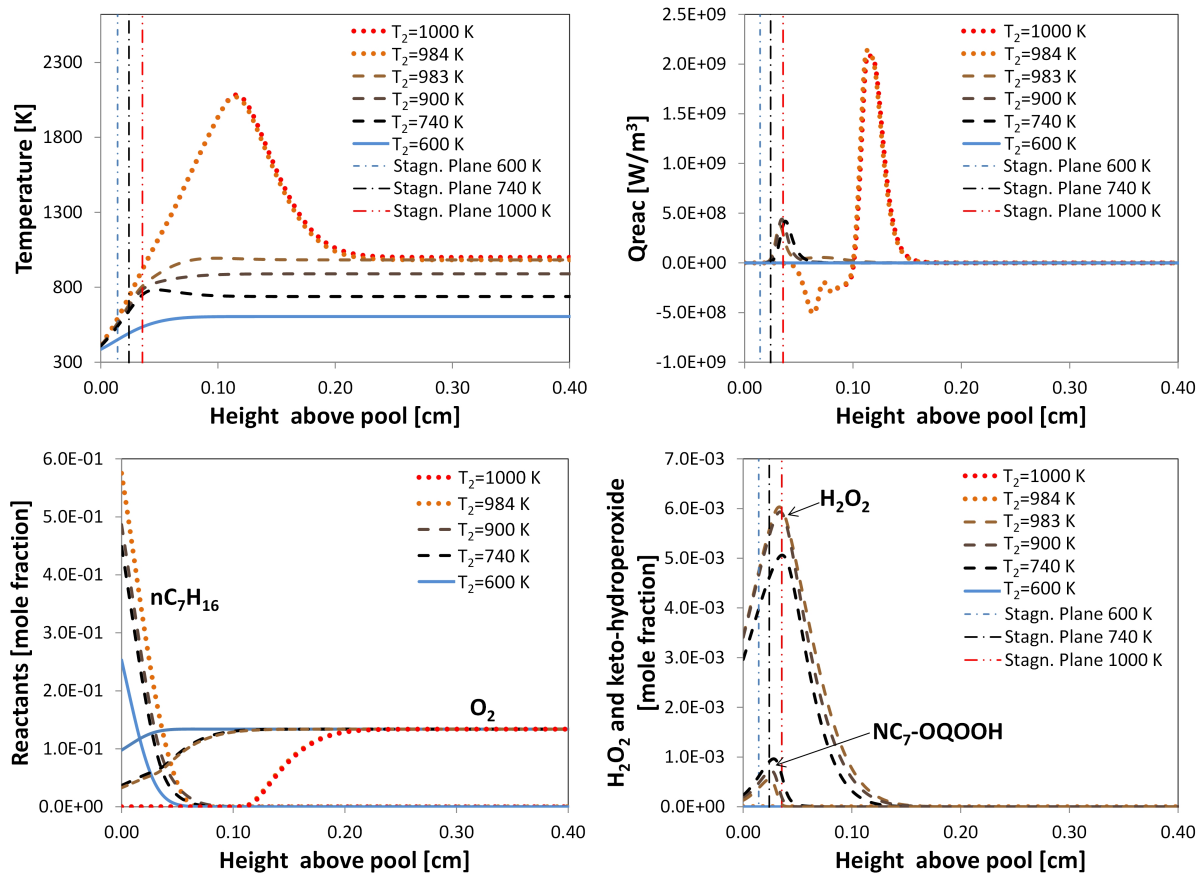
Figure 11. Temperature profile, and profiles of n-heptane, oxygen, hydrogen peroxide, heptyl-ketohydroperoxide (KET) and heat release rates, Q_{reac} as a function of the height about the liquid-gas interface for various values of temperature of the oxidizer stream, T_2. The fuel is n-heptane, $p = 6\,\mathrm{atm}$, $a_2 = 138\,\mathrm{s}^{-1}$, and $Y_{O_2} = 0.15$. KET is marked as NC7-OQOOH in the figure.

temperatures of the oxidizer stream above T_{ig} is very different from those below T_{ig}. The heat release profile now shows a region where endothermic pyrolysis is taking place followed by an exothermic region. Fuel is completely consumed and very little KET is formed. Due to the enhanced burning rate of the liquid fuel with increasing T_2, the stagnation plane moves towards the oxidizer stream.

Figure 12 shows the sensitivity coefficients for the n-heptane flame at $p = 4\,\mathrm{atm}$, $T_2 = 1050\,\mathrm{K}$, $a_2 = 138\,\mathrm{s}^{-1}$, and $Y_{O_2} = 0.15$, just before the hot ignition takes place. It shows that the system is sensitive to reactions that characterize low and intermediate temperature chemistry. The largest positive sensitivity is the expected production rate of OH, the dominant radical that carries the low temperature chain. In addition, the competition between oxygen addition to the hydroperoxy-alkyl radical and its reverse dissociation, as well as, to a lesser extent, its decomposition reactions, forming HO_2 and the parent olefin or OH, and the C_7-heterocycle, mainly controls the reactivity of the flame. Decomposition reactions of peroxides (H_2O_2 and NC7-OQOOH) form OH radicals and thus favor the hot ignition. Therefore, the system is also very sensitive to the reaction forming the heptyl-ketohydroperoxide. Results similar to those shown in Fig. 12 are also obtained when sensitivity analysis is performed using the San Diego Mechanism [42].
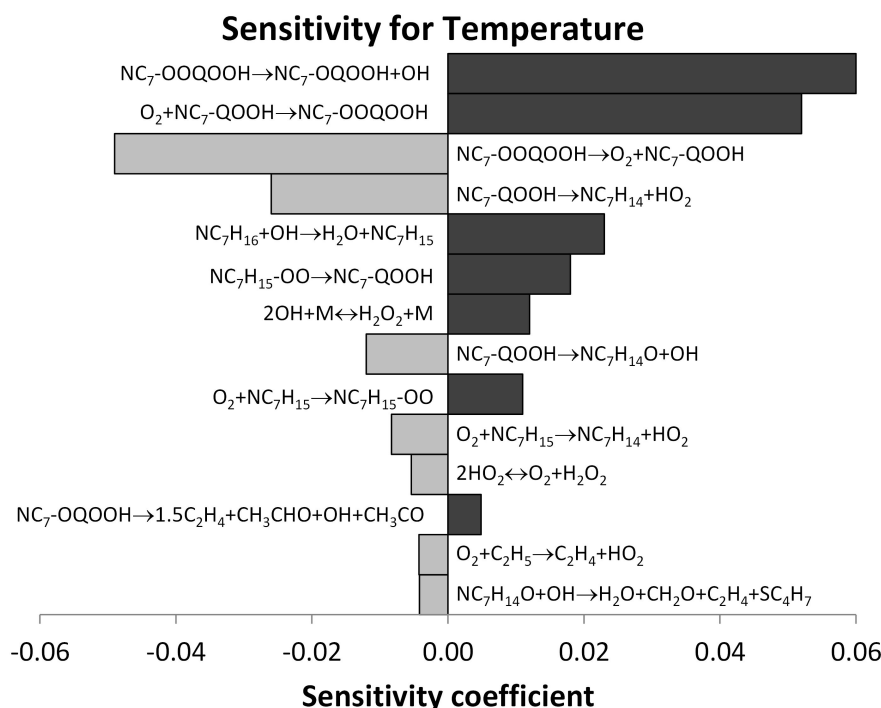
Sensitivity for Temperature

Figure 12.   Maximum sensitivity coefficient for temperature in the n-heptane flame. The fuel is n-heptane, $p = 4\,\text{atm}$, $T_2 = 1050\,\text{K}$, $a_2 = 138\,\text{s}^{-1}$, and $Y_{O_2} = 0.15$. Positive sensitivity coefficients identify reactions which enhance the reactivity of the system, favoring autoignition.

5.   Concluding Remarks

The experimental and computational studies described here show the dominant role of low temperature chemistry in promoting autoignition of the condensed hydrocarbon fuels tested here. The investigation described here was restricted to low values of the strain rates and low values of Y_{O_2}. Moreover, the physical properties and mainly vapor pressure of the different fuels affect the autoignition temperatures. It would be of interest to test the influence of low temperature chemistry on autoignition at higher values of strain rates and higher values of Y_{O_2}. The maximum value of p considered here was 6 bar. It would be of interest to measure critical conditions of autoignition at higher values of pressure.

References

[1]   S. Dooley, S.H. Won, J. Heyne, T.I. Farouk, Y. Ju, F.L. Dryer, K. Kumar, X. Hui, C.J. Sung, H. Wang, M.A. Oehlschlaeger, V. Iyer, S. Iyer, T.A. Litzinger, R.J. Santoro, T. Malewicki, and K. Brezinsky, *The experimental evaluation of a methodology for surrogate fuel formulation to emulate gas phase combustion kinetic phenomena*, Combustion and Flame 159 (2012), pp. 1444–1466.

[2] T. Malewicki, S. Gudiyella, and K. Brezinsky, *Experimental and modeling study on the oxidation of jet a and the n-dodecane/iso-octane/n-propylbenzene/1,3,5-trimethylbenzene surrogate fuel*, Combustion and Flame 160 (2013), pp. 17–30.

[3] Y. Zhu, S. Li, D.F. Davidson, and R.K. Hanson, *Ignition delay times of conventional and alternative fuels behind reflected shock waves*, Proceedings of the Combustion Institute 35 (2014), p. in press.

[4] K. Kumar and C.J. Sung, *An experimental study of the autoignition characteristics of conventional jet fuel/oxidizer mixtures: Jet-A and JP-8*, Combustion and Flame 157 (2010), pp. 676–685.

[5] N. Peters, G. Paczko, R. Seiser, and K. Seshadri, *Temperature cross-over and non-thermal runway at two-stage ignition of n-heptane*, Combustion and Flame 128 (2002), pp. 38–59.

[6] K. Narayanaswamy, P. Pepiot, and H. Pitsch, *A chemical mechanism for low to high temperature oxidation of n-dodecane as a component of transportation fuel surrogates*, Combustion and Flame 161 (2014), pp. 866–884.

[7] L. Figura and A. Gomez, *Structure of incipiently sooting ethylenenitrogen counterflow diffusion flames at high pressures*, Combustion and Flame 161 (2014), pp. 1587–1603.

[8] U. Niemann, K. Seshadri, and F.A. Williams, *Effect of pressure on structure and extinction of near-limit hydrogen counterflow diffusion flames*, Proceedings of the Combustion Institute 34 (2013), pp. 881–886.

[9] U. Niemann, K. Seshadri, and F.A. Williams, *Methane, ethane, and ethylene laminar counterflow diffusion flames at elevated pressures: Experimental and computational investigations up to 2.0 MPa*, Combustion and Flame 161 (2014), pp. 138–146.

[10] R. Gehmlich, A. Kuo, and K. Seshadri, *Experimental investigations of the influence of pressure on critical extinction conditions of laminar nonpremixed flames burning condensed hydrocarbon fuels, jet fuels, and surrogates*, Proceedings of the Combustion Institute 35 (2014), pp. 937–943.

[11] A. Smallbone, W. Liu, C. Law, X. You, and H. Wang, *Experimental and modeling study of laminar flame speed and non-premixed counterflow ignition of n-heptane*, Proceedings of the Combustion Institute 32 (2009), pp. 1245–1252.

[12] G. Jomaas, X. Zheng, D. Zhu, and C. Law, *Experimental determination of counterflow ignition temperatures and laminar flame speeds of C_2–C_3 hydrocarbons at atmospheric and elevated pressures*, Proceedings of the Combustion Institute 30 (2005), pp. 193–200.

[13] S. Honnet, K. Seshadri, U. Niemann, and N. Peters, *A surrogate for kerosene*, Proceedings of the Combustion Institute 32 (2008), pp. 485–492.

[14] S. Humer, R. Seiser, and K. Seshadri, *Experimental investigation of combustion of jet fuels and their surrogates in laminar nonpremixed flows*, Journal of Propulsion and Power 27 (2011), pp. 847–855.

[15] R. Seiser, H. Pitsch, K. Seshadri, W. Pitz, and H. Gurran, *Extinction and autoignition of n-heptane in counterflow configuration*, Proceedings of the Combustion Institute 28 (2000), pp. 2029–2037.

[16] K. Seshadri, S. Humer, and R. Seiser, *Activation-energy asymptotic theory of autoignition of condensed hydrocarbon fuels in non-premixed flows with comparison to experiment*, Combustion Theory and Modelling 12 (2008), pp. 831–855.

[17] R. Grana, K. Seshadri, A. Cuoci, U. Niemann, T. Faravelli, and E. Ranzi, *Kinetic modelling of extinction and autoignition of condensed hydrocarbon fuels in non-premixed flows with comparison to experiment*, Combustion and Flame 159 (2012), pp. 130–141.

[18] W. Liu, J.A. Koch, and C.K. Law, *Nonpremixed ignition of $C_7$$C_{16}$ normal alkanes in stagnating liquid pool*, Combustion and Flame 158 (2011), pp. 2145–2148.

[19] K. Seshadri and F.A. Williams, *Laminar flow between parallel plates with injection of a reactant at high Reynolds number*, International Journal of Heat and Mass Transfer 21 (1978), pp. 251–253.

[20] R. Seiser, *Nonpremixed combustion of liquid hydrocarbon fuels*, Ph.D thesis, Technical University of Graz, 2000.

[21] E. Ranzi, A. Frassoldati, R. Grana, A. Cuoci, T. Faravelli, A. Kelley, and C. Law, *Hierarchical and comparative kinetic modeling of laminar flame speeds of hydrocarbon and oxygenated fuels*, Progress in Energy and Combustion Science 38 (2012), pp. 468–501.

[22] http://creckmodeling.chem.polimi.it (2011).

[23] E. Ranzi, A. Frassoldati, A. Stagni, M. Pelucchi, A. Cuoci, and T. Faravelli, *Reduced kinetic schemes of complex reaction systems: Fossil and biomass-derived transportation fuels*, International Journal of Chemical Kinetics 46 (2014), pp. 512–542.

[24] E. Ranzi, C. Cavallotti, A. Cuoci, A. Frassoldati, M. Pelucchi, and T. Faravelli, *New reaction*

classes in the kinetic modeling of low temperature oxidation of n-alkanes, Combustion and Flame 162 (2015), pp. 1679–1691.

[25] M. Pelucchi, M. Bissoli, C. Cavallotti, A. Cuoci, T. Faravelli, A. Frassoldati, E. Ranzi, and A. Stagni, *Improved kinetic model of the low-temperature oxidation of n-heptane*, Energy & Fuels 28 (2014), p. 7178.

[26] A. Stagni, A. Frassoldati, A. Cuoci, T. Faravelli, and E. Ranzi, *Skeletal mechanism reduction through species-targeted sensitivity analysis*, Combustion and Flame 163 (2016), pp. 382–393.

[27] K.E. Niemeyer, C.J. Sung, and M.P. Raju, *Skeletal mechanism generation for surrogate fuels using directed relation graph with error propagation and sensitivity analysis*, Combustion and Flame 157 (2010), pp. 1760–1770.

[28] E. Ranzi, S. Granata, A. Frassoldati, and T. Faravelli, *Wide range kinetic modeling study of pyrolysis and combustion of heavy n-alkanes*, Industrial & Engineering Chemistry Research 44 (2005), pp. 5170–5183.

[29] M. Mehl, W.J. Pitz, C.K. Westbrook, and H.J. Curran, *Kinetic modeling of gasoline surrogate components and mixtures under engine conditions*, Proceedings of the Combustion Institute 33 (2011), pp. 193–200.

[30] H.K. Ciezki and G. Adomeit, *Shock-tube investigation of self-ignition of n-heptane-air mixtures under engine relevant conditions*, Combustion and Flame 93 (1993), pp. 421–433.

[31] H.S. Shen, J. Steinberg, J. Vanderover, and M.A. Oehlschlaeger, *A shock tube study of the ignition of n-heptane, n-decane, n-dodecane, and n-tetradecane at elevated pressures*, Energy & Fuels , p. 24822489.

[32] U. Pfahl, K. Fieweger, and G. Adomeit, *Self-Ignition of Diesel-Relevant Hydrocarbon-Air Mixtures Under Engine Conditions*, in *Twenty-Sixth Symposium (International) on Combustion*, The Combustion Institute, Pittsburgh, Pennsylvania, 1996, pp. 781–789.

[33] V.P. Zhukov, V.A. Sechenov, and A.Y. Starikovskii, *Autoignition of n-decane at high pressure*, Combustion and Flame 153 (2008), pp. 130–136.

[34] S. Vasu, D. Davidson, Z. Hong, V. Vasudevan, and R. Hanson, *n-dodecane oxidation at high-pressures: Measurements of ignition delay times and OH concentration time-histories*, Proceedings of the Combustion Institute 32 (2009), pp. 173–180.

[35] R.H. D.F. Davidson D.R. Haylett, *Development of an aerosol shock tube for kinetic studies of low-vapor-pressure fuels*, Combustion and Flame , pp. 108–117.

[36] A. Cuoci, A. Frassoldati, T. Faravelli, and E. Ranzi, *OpenSMOKE++: an object-oriented framework for the numerical modeling of reactive systems with detailed kinetic mechanisms*, Computer Physics Communications 192 (2015), pp. 237–264.

[37] U. Niemann, R. Seiser, and K. Seshadri, *Ignition and extinction of low molecular weight esters in nonpremixed flows*, Combustion Theory and Modelling 14 (2010), pp. 831–855.

[38] D.W. Green and R.H. Perry, *Perry's Chemical Engineers' Handbook*, 8th ed., McGraw Hill, 2008.

[39] C.M. Müller, K. Seshadri, and J.Y. Chen, *Reduced kinetic mechanisms for counterflow methanol diffusion flames*, in *Reduced Kinetic Mechanisms for Applications in Combustion Systems*, N. Peters and B. Rogg, eds., Lecture Notes in Physics, Vol. m 15, chap. 16, Springer-Verlag, Berlin Heidelberg, 1993, pp. 284–307.

[40] A. Cuoci, A. Frassoldati, T. Faravelli, and E. Ranzi, *Frequency response of counterflow diffusion flames to strain rate harmonic oscillations*, Combustion Science and Technology 180 (2008), pp. 767–784.

[41] K. Seshadri, A. Frassoldati, A. Cuoci, T. Faravelli, U. Niemann, P. Weydert, and E. Ranzi, *Experimental and kinetic modeling study of combustion of jp-8, its surrogates and components in laminar premixed flows*, Combustion Theory and Modelling (2011), p. to appear.

[42] J.C. Prince, F.A. Williams, and G.E. Ovando, *A short mechanism for the low-temperature ignition of n-heptane at high pressures*, Fuel 149 (2015), pp. 138–142.

[43] A. Frassoldati, G. D'Errico, T. Lucchini, A. Stagni, A. Cuoci, T. Faravelli, A. Onorati, and E. Ranzi, *Reduced kinetic mechanisms of diesel fuel surrogate for engine cfd simulations*, Combustion and Flame 162 (2015), pp. 3391–4007.

[44] H.J. Curran, P. Gaffuri, W.J. Pitz, and C.K. Westbrook, *A comprehensive modeling study of n-heptane oxidation*, Combustion and Flame 114 (1998), pp. 149–177.

[45] A. Liñán, *The asymptotic structure of counterflow diffusion flames for large activation energies*, Acta Astronautica 1 (1974), pp. 1007–1039.